

MABE, TAYLOR LEVI, Ph.D. Nanostructured Metallic Film Plasmonics: Fabrication and Biosensing Applications. (2018)
Directed by Dr. Jianjun Wei. 188 pp.

The research presented in this dissertation is interdisciplinary in nature. It covers the areas of micro- and nanofabrication, chemistry, materials science, and biological sensing. The running theme of the dissertation is the fabrication of micro- and nanostructures for use in plasmonic devices to aid in the optical detection of biomolecules. Phase I of the research focused on a bimetallic nanostructured (nanoslit) film to aid in improving the sensitivity in comparison to pure gold films. Phase II of the research investigated nanoledge structures (stair-step features) for their ability to trap biomolecules and aid in surface plasmon resonance sensing. Phase III of the research examined how to produce a fluidic dam, a microstructure with an overcut sidewall profile, which could aid in separating biological entities from the proteins of interest. Phase IV of the research assessed the use of the fluidic dam and nanoledge structures for detection of Troponin T, a biomarker used in the diagnosis of heart attacks. Phase V of the research focused on the design and microfabrication of a plasmonic device, which could study how surface plasmon resonance influences a photocurrent generated by immobilizing photosystem I in a nanoslit structure.

NANOSTRUCTURED METALLIC FILM PLASMONICS:
FABRICATION AND BIOSENSING APPLICATIONS

by

Taylor Levi Mabe

A Dissertation Submitted to
the Faculty of The Graduate School at
The University of North Carolina at Greensboro
in Partial Fulfillment
of the Requirements for the Degree
Doctor of Philosophy

Greensboro
2018

Approved by

Dr. Jianjun Wei
Committee Chair

APPROVAL PAGE

This dissertation, written by Taylor Levi Mabe, has been approved by the following committee of the Faculty of The Graduate School at The University of North Carolina at Greensboro.

Committee Chair Jianjun Wei

Committee Members James G. Ryan

Dennis LaJeunesse

Joseph M. Starobin

Shyam Aravamudhan

October 17, 2018
Date of Acceptance by Committee

October 17, 2018
Date of Final Oral Examination

ACKNOWLEDGMENTS

Thanks to my father for my scientific curiosity, my mother for my ability to work through the night, my grandfather for my ability to laugh at myself, Dr. James Ryan for our many long discussions about life and thin film technology, Dr. Jianjun Wei for his guidance, Dr. Zheng Zeng for all of his simulation work, Glenn Seymour for a wonderful partnership during our NSF I-Corps experience, Dr. Nadja Cech for turning on my spark for chemistry, Alla Letfullina for being my biggest supporter, the UNCG Chemistry Dept. for always being my home, and the Joint School of Nanoscience & Nanoengineering for giving me access to all of the “toys” a boy could dream of and for leading me to Alla.

TABLE OF CONTENTS

	Page
LIST OF TABLES	vi
LIST OF FIGURES	vii
LIST OF EQUATIONS.....	xii
CHAPTER	
I. INTRODUCTION	1
Analytical Instrumentation and Biosensing Technology	1
Surface Plasmon Resonance (SPR)	3
Excitation of Surface Plasmon Polaritons	7
Extraordinary Optical Transmission (EOT)	9
Nanostructured Substrate Designs.....	11
Instrumentation Setup.....	13
Brief Introduction of Each Chapter	14
References	17
II. BIMETALLIC FILMS FOR ENHANCED SENSITIVITY	20
Overview	20
Introduction	21
Results and Discussion	24
Conclusion	32
References	34
III. PROTEIN SENSING IN NANOEDGE STRUCTURES	37
Overview	37
Introduction	38
Methods and Materials	40
Results and Discussions	45
Conclusions	58
References	60

IV. MICROFABRICATION OF A FLOW-OVER FLUIDIC DAM	64
Overview	64
Introduction	64
Materials and Methods	73
Conclusion	90
Discussion of Techniques	91
References	100
V. TROPONIN T BIOSENSING	103
Overview	103
Introduction	103
Experimental	107
Results	117
Conclusion	123
References	125
VI. FABRICATION OF A PLASMONIC PHOTOCURRENT DEVICE	128
Overview	128
Introduction	128
Materials and Methods	131
Results and Discussion	135
Conclusions	144
References	145
VII. CONCLUSION AND FUTURE CONSIDERATIONS	150
APPENDIX A. SUPPORTING INFORMATION FOR CHAPTER II	155
APPENDIX B. SUPPORTING INFORMATION FOR CHAPTER III	168
APPENDIX C. SUPPORTING INFORMATION FOR CHAPTER VI	175

LIST OF TABLES

	Page
Table 1.1. Comparison of Large Bench Top Instruments to Point-of-care Biosensors	3
Table 1.2. Comparison between SPR and LSPR	6
Table 3.1. Results Obtained from FCS Measurements	53

LIST OF FIGURES

	Page
Figure 1.1. Schematic of LSPR and SPR with Y Shaped Ligands on the Gold Surface and Red Circular Analytes Flowing Over	4
Figure 1.2. The Dispersion Relation for Frequency (ω) vs. the Wavevector (κ).....	8
Figure 1.3. The Four Methods to Excite SPPs with Photons.....	9
Figure 1.4. Ebbensen's Group (A) Square Array of Nanoholes from the Seminal Paper in 1998 and (B) Bulls-eye Array from the Later Work in 2001.....	10
Figure 1.5. (A) Instrumental Setup with Incident Broadband Light from Underneath the Substrate Exciting Surface Plasmons in the Nanohole and Nanoslit Arrays and the Collected Light is Measuring with Spectrophotometer	11
Figure 1.6. Gold Nanoslit, Bimetallic Nanoslit, and Gold Nanoledge	12
Figure 1.7. Instrumentation and Setup for Sensing in Transmission SPR.....	13
Figure 2.1. A Schematic Drawing of (a) Gold Nanoslit Structure and (b) Bimetallic Nanoslit Structure	25
Figure 2.2. (a) Experimental and (b) FDTD Simulation Results Showing the Correlation of Resonant Peak Position with Nanoslit Period for 450 nm, 500 nm, and 550 nm Period Arrays.....	27
Figure 2.3. Semi-Analytical Analysis of SP Generation and FDTD Simulation of Nanoslit Array.....	29
Figure 2.4. Transmission Spectra of (a) Au and (b) Ag/Au Devices in Glycerol/Water Solutions	31
Figure 2.5. Schematic of the Nanoslit Device (a) Before Binding of the SAM and (b) After the SAM Formation.....	32
Figure 3.1. (a) Schematic Illustration of the Interface between the Nanoledge Array at the Quartz Chip and PDMS Microfluidic Channel, (b) Side View of the Micro-channel and, (c) a SEM Image of the Nanoledge Array	44

Figure 3.2.	The SP Generation Efficiency Change, $\Delta(e_1+e_2+e_3)$, for the Nanoledge Geometry of 280-50 nm with on-top SiO ₂ layer (a) and without on-top SiO ₂ Layer (b) for the Bulk Media RI Ranging from 1.0 to 1.2	47
Figure 3.3.	Left: Schematic Diagram of TIRF Imaging	50
Figure 3.4.	(a) Diagram of FCS Setup for Measuring Protein Diffusion in the Nanoslits	52
Figure 3.5.	(a) An Illustration of the Immobilization of the Detection Antibody (mAb) at the SAM for f-PSA Binding	55
Figure 4.1.	(A) Flow-over vs. (B) Flow-through Sensing with Red Balls Representing Analytes.....	66
Figure 4.2.	(A) Standard Gold Surface and Flow Channel.....	68
Figure 4.3.	(A) Schematic of Chip with a Magnification on the Fluidic Dam	69
Figure 4.4.	Fabrication Process Overview for a Fluidic Dam: (A) Mask Designed in CAD Software, (B) Glass Substrate Cleaned and Dehydrated (C) Spin Apply Photoresist, (D) Lithography, (E) Etching, (F) Metal Deposition, and (G) Oxide Deposition	70
Figure 4.5.	Cross Section Sidewall Profiles in Patterned Photoresist Include (A) Straight Sidewalls, (B) Undercut Trapezoid, (C) T Topped Profile, and (D) Overcut Trapezoid.....	71
Figure 4.6.	Glass Substrate with Two Fluidic Dams with Undercut Sidewalls.....	71
Figure 4.7.	An Undercut Sidewall Made of Transparent Photoresist Will Be Transparent to Light When a Light Source is Placed Underneath the Substrate.....	73
Figure 4.8.	(A) Reflection Image of a Fluidic Dam with a 75 μm x 25 μm Reference Box Milled into the Dam.....	74
Figure 4.9.	(A) Reflection Microscope Image of a Fluidic Dam without Nanostructures Milled into the Dam	75
Figure 4.10.	SEM Cross-section Image Showing a T Topped Photoresist.....	78

Figure 4.11.	A Transmission Spectrum Showing Various Filters for Their Ability to Act as Long Pass Wavelength Filters.....	79
Figure 4.12.	SEM Images Showing Cross-sections of Photoresist Structures	80
Figure 4.13.	Fabrication Process for the Flow-over Fluidic Dam with Overcut Sidewall Profile Using a Multi-layered Resist (MLR) Method	83
Figure 4.14.	(A) Optical Microscope Image Showing an Overcut Fluidic Dam	85
Figure 4.15.	Photograph of a Glass Substrate (A) after Lithography with Clear SU-8 Forming Two Flow-over Dams on the Substrate and (B) after Metal Deposition.....	86
Figure 4.16.	Schematic of FIB Milled Structure (A) with SiO ₂ Capping Layer and (B) without SiO ₂ Capping Layer	87
Figure 4.17.	(A) A Schematic Showing the Rectangular Design That Was Entered into the Focused Ion Beam Patterning Software.....	88
Figure 4.18.	(A) A Photograph of a Chip after the Microfabrication of the Fluidic Dam, Metal Deposition, and SiO ₂ Deposition	89
Figure 4.19.	A SEM Image Showing a Flow-over Fluidic Dam with a Reference Window Milled on the Left Side and an Array of Nanostructures Milled on the Right Side of the Dam.....	90
Figure 4.20.	A FIB Image Showing a Flow-over Fluidic Dam with an Array of Nanoledge Structures Milled into the Dam	90
Figure 4.21.	SEM Image Showing a Flow-over Dam with a Rough Surface Due to Under Etching and a Non-planar Top to the Dam	92
Figure 4.22.	Process for Making a Metal Etch Mask	94
Figure 4.23.	SEM Image Showing a Rough Surface	95
Figure 4.24.	Profilometry Scan Showing an Etch Depth of 180 nm after a 1.5-hour Dry Etch.....	96
Figure 4.25.	(A) A Photograph Image of a Polymeric Substrate; the Center Region Shows a Ripple Effect from the Developer Solution Dissolving the Polymer Substrate, (B) An Optical Microscope	

	Image of a Polymeric Substrate with Patterned Photoresist Shown in Red	97
Figure 4.26.	Schematics Showing Topside and Backside Exposure of a Photoresist through a Photomask and the Resultant Shape of Patterned Photoresist	98
Figure 4.27.	SEM Cross-section Image of a Photoresist Exposed from the (A) Topside with an Exposure Gap Yielded a Sidewall Angle of 122.9° (Undercut Profile), (B) Topside in Soft Contact Mode Yielded a Sidewall Angle of 98.7° (Undercut Profile), (C) Backside in Soft Contact Mode Yielded a Sidewall Angle of 89.1° (Straight Sidewall Profile).....	99
Figure 5.1.	(A) Scanning Electron Microscope (SEM) Image of an Actual Flow-over, Fluidic Dam with Nanostructures Milled into the Top of the Dam; the Dam Measures 45 μm in Width and is 7 μm in Height, (B) A Plasmonic Chip with Enclosed Polyethylene Flow Chamber; the Penny is for a Scale/Size Comparison, (C) A Drawing of the Cross-section View of a Dam with Gold Thin Film atop the Dam; Into the Gold Film are a Reference Window and an Array Nanostructures.....	107
Figure 5.2.	Fabrication Process for the Flow-over Fluidic Dam with Overcut Sidewall Profile Using a Multi-layered Resist (MLR) Method	109
Figure 5.3.	An Overview of the Fabrication Process is as Follows: (A) Thin Film Deposition, (B) Nanostructuring by Focused Ion Beam Milling, (C) Surface Chemistry by Self Assembly, (D) Flow Chamber Fabrication and Bonding to Chip, and (E) Transmission SPR Measurement	110
Figure 5.4.	Schematic of FIB Milled Structure (A) with SiO ₂ Capping Layer and (B) without SiO ₂ Capping Layer	111
Figure 5.5.	A Photograph of a Chip after the Microfabrication of the Fluidic Dam, Metal Deposition, and SiO ₂ Deposition.....	111
Figure 5.6.	A Schematic Showing the Stepwise Sequence of the SAM Formation, DNA Aptamer Attachment, and Protein Binding to the DNA Aptamer.....	113

Figure 5.7.	(A) A Schematic of a Chip with Fluidic Dam in the Center of the Flow Channel	114
Figure 5.8.	Scanning Electron Microscope (SEM) Images of a Flow-over Dam with Milled (A) Nanoledge Array and (B) Reference Box	117
Figure 5.9.	A Cross-section View of a Drawing of a Fluidic, Flow-over Dam with an (A) Undercut Profile and a (B) Overcut Profile	118
Figure 5.10.	(A) A Reflection Optical Microscope Image of a Flow-over Fluidic Dam	120
Figure 5.11.	Optical Transmission Spectrum through a Nanoledge Array Showing Peak Shifts to Longer Wavelengths with Increasing Concentration of Troponin T Protein	121
Figure 5.12.	The Dependence of the Peak Wavelength Shift ($\Delta\lambda_{\text{SPR}}$) on the Concentration of Troponin T Protein is a Logarithmic Relationship	122
Figure 5.13.	Optical Transmission Spectrum through a Nanoledge Array Showing Little to No Peak Shift with Interleukin-6 (IL-6) Protein in the Running Solution	123
Figure 6.1.	A Schematic View of a Method for the PSI Immobilization with a SAM and a Setup for the Light Associated Electrochemistry Analysis of PSI	136
Figure 6.2.	(a) Illustration of the Electron Transfer from PSI to Au Slide Electrode with the Reaction-center Electron Transfer Chain.....	137
Figure 6.3.	(a) Illustration of the Key Parameters for the SPG Calculation with Respect to the Structure of the Nanoslit and Light Source	140
Figure 6.4.	(a) Light Intensity Measurements for Different Nanoslit Structures in Reflection Mode, (b) Peak Intensity Versus Different Nanoslit Structures.....	142
Figure 6.5.	Plot of Average Photocurrent in Experimental Measurements or Calculated SPG Efficiency Versus Nanoslit Width.....	144

LIST OF EQUATIONS

	Page
Equation 1.1. Overall Response of SPR or LSPR Measured as a Wavelength Shift ($\Delta\lambda$)	6
Equation 1.2. The Resonant Surface Plasmon Wavelength is Governed by the Above Equation.....	14

CHAPTER I

INTRODUCTION

Decreasing the size of a chemical or biological sensor (biosensors) can show analogous improvements to those that have revolutionized the semiconductor industry. In a decade of time we have moved from large, tabletop computers to a world where the majority of Americans own a smart phone that fits in the palm of the hand. Similarly, chemical sensing has relied on large benchtop instruments for years, but moving to sensors that can fit in the hand offer several benefits when compared to their large, benchtop counterparts. Point-of-care analysis, in which the “lab” is brought to the patient’s bedside as opposed to collecting a sample and transporting the sample to a centralized laboratory, is the primary benefit to the patient.

The overarching theme of my research is in the fabrication and study of portable, handheld biosensors. My area of interest and focus within this large area is in micro- and nanofabrication and surface plasmon resonance (introduced below) bio-detection. Below I account an introduction to the background material and at the end of this chapter I give a brief introduction to the work in each chapter.

Analytical Instrumentation and Biosensing Technology

The world’s analytical instrumentation market is currently around \$12 billion and less than 0.1% are small biosensors.¹ Consequently, there is a vast market growth

potential and need, as point of care (POC) analysis would solve many of the shortcomings with large benchtop instruments. Speed, cost, portability, throughput, versatility, selectivity, and sensitivity are all factors that analytical instruments are evaluated on. Simply shrinking the size of the instrument can enhance the first 3 metrics. Common techniques to detect analytes in low concentration are electrical, optical or mass based.^{2,3} Electrochemical methods are easy to shrink down to a point of care sensor and are cheap to fabricate, but need a power supply and rely on redox chemistry, which gets complicated for large protein molecules. Most optical techniques, like fluorescence, require the addition of a label or dye to the molecule of interest. This can be a lengthy process that requires some technical ability. Mass spectrometry (MS) is a common mass sensing technique and is considered the gold standard for chemical analysis. MS does have drawbacks. The technique excels with small molecule assays but becomes increasingly difficult for protein analysis, which are the analyte of interest in disease diagnostics. The instruments are quite expensive, large, and elaborate to operate and maintain. Table 1.1 compares a large benchtop instruments to smaller, point of care devices on the basis of cost, speed, portability, solvents used, waste generated, repair cost and limit of detection (LOD). The POC device triumphs on every metric in the table except the LOD.⁴ The primary shortcoming of the POC biosensor is due to low sensitivity, which results in a high limit of detection. None of the previous mentioned techniques have found their way into a point of care (POC) sensor. A POC device capable of label-free, real time analysis that is sensitive, portable, cheap, and in complex

media is of high interest. The optical technique of surface plasmon resonance (SPR) shows the most promise in achieving that goal.⁵

Table 1.1

Comparison of Large Bench Top Instruments to Point-of-care Biosensors.^{4,6}

Metric	Large Instrument	POC Biosensor
Initial Cost	\$.25 Million	\$2 Thousand
Analysis Time	Weeks	Minutes
Portability	No (100 lbs.)	Yes (< 5 lbs.)
Solvents	1000 X	1 X
Waste	1000 X	1 X
Repair	Costly	Disposable Devices
Limit of Detection	fM (10^{-15} M)	pM (10^{-12} M)

Surface Plasmon Resonance (SPR)

Surface plasmons, by definition, are quanta of collective surface charge oscillations.⁷ Surface plasmons (SP) can be thought of as a density wave of electrons at the interface of a metal and dielectric. These surface charge oscillations are induced by electromagnetic (EM) radiation with an appropriate coupler.⁷ When the incident EM field has a frequency matching that of the plasmons, those electrons resonate, increase in intensity and emit detectable radiation. SPs are very sensitive to the local refractive index and are effective at measuring binding events. Therefore, they make up the technique known as surface plasmon resonance (SPR). SPR is a label-free technique that can

monitor, in real-time, very low concentrations of many analytes at once (multiplexing).⁸ It is a resourceful technique as it gives concentration and kinetic information about the binding events.⁷ Traditional surface plasmon resonance is known as the Kretschmann configuration (Figure 1.1B) and uses total internal reflection (TIR) to couple the incident light into surface plasmon polaritons (SPPs).⁷ SPPs are propagating waves of electron density, whereas non-propagating plasmons are termed localized surface plasmon resonance (LSPR).

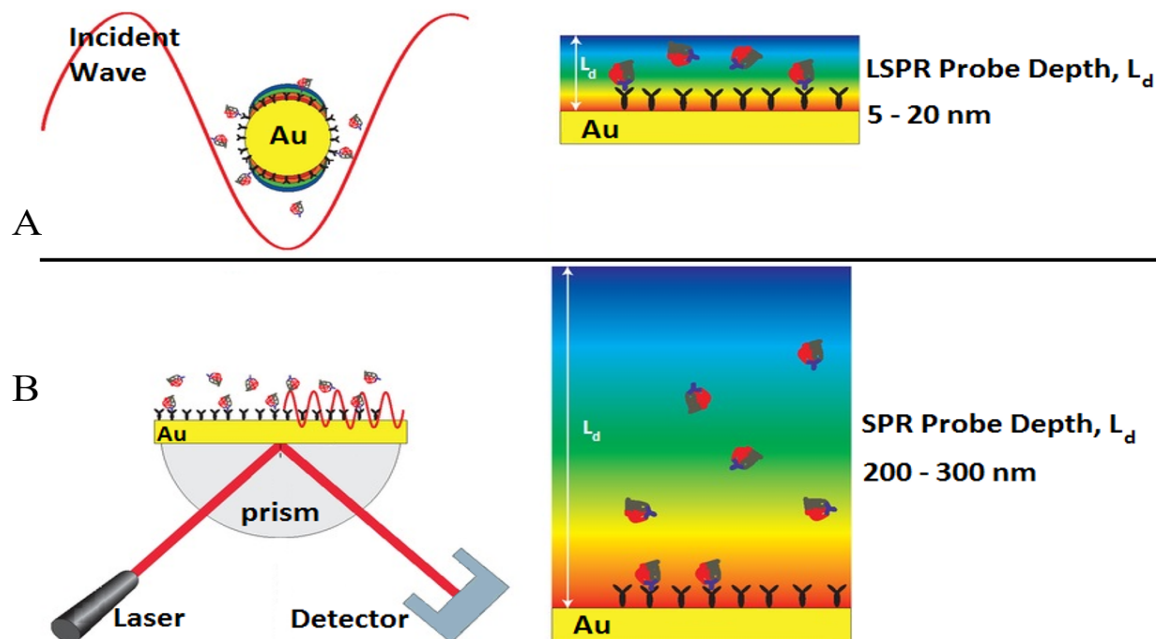


Figure 1.1. Schematic of LSPR and SPR with Y Shaped Ligands on the Gold Surface and Red Circular Analytes Flowing Over. EM Field Intensity Gradient Shows the Intensity of the Evanescent Wave with Color Change; Red as High and Blue as Low EM Field. (A) LSPR Effect Where the Nanostructure Dimension is Far Smaller Than the Wavelength of Light. Probe Depth (L_d) is on the Order of 10's of nm. (B) Total Internal Reflection SPR (Kretschmann Configuration). The Electrons Oscillate Perpendicular to the Metal Film after Total Internal Reflection of the Incident Laser Light. The SPPs Propagate Parallel to the Surface and over a Distance of Microns. The Evanescent Field (Probe Depth) is Much Longer Than in LSPR. L_d for SPR is on the Order of 100's of nm.⁹

LSPR occurs when metallic structures, smaller than the incident wavelength, interact with light to give a plasmon that oscillates locally (Figure 1.1A).⁸ LSPR ensues when the incident photon frequency (ω_{light}) matches that of the frequency for the conduction band electrons in the metal structure (ω_{metal}). Many structures have been studied: nanoparticles, nanotriangles, core-shell particles, etc.^{4,10} LSPR is a non-propagating mode and has several benefits over TIR SPR.⁸ As Table 1.2 shows, both techniques are label-free with multiplex capabilities and real-time detection, but LSPR shines due to the short probe distance (provides LSPR with increases sensitivity), lack of required temperature control, portability, major reduction in cost, and low spatial resolution.⁸ The low cost and lack of temperature control make LSRP better suited for POC applications over SPR. The instrumental design in LSPR becomes simplified over the total internal reflection (TIR) design, which requires a laser, polarizer, moveable mirrors, and temperature control). One alarm is the third metric in Table 1.2, the refractive index (RI) sensitivity. The overall sensitivity of LSPR is actually comparable to SPR due to the short probe depth of LSPR.⁹ Governed by Equation 1.1, the overall response of SPR or LSPR can be monitored with a shift in wavelength. When comparing SPR to LSPR via Equation 1.1, there are only two variables to note, m (RI sensitivity) and L_d (the probe depth). LSPR affords the ability to shrink the instrumentation by losing the bulky optics, prism, and mirrors found in SPR. The portability is of prime interest to afford point of care (POC) analysis. This significantly affects the cost, turnaround time, shipping requirements, and locations at which testing can be done. POC testing allows for

immediate, on-site results as opposed to drawing blood, shipping to a centralized laboratory, and waiting weeks for the test results. The immediate results, lower cost, and elimination of refrigerated shipments of biological samples are benefits of POC testing. The low cost, label-free and real-time analysis, ease of use, and portability united with the sensitivity and versatility of LSPR make it a strong candidate for POC biosensing and are strong attributes over the current technology.

$$\Delta\lambda_{\max} = m\Delta n(1 - \exp(-2d/l_d))$$

Equation 1.1. Overall Response of SPR or LSPR Measured as a Wavelength Shift ($\Delta\lambda$). The Other Variables Include: m as the Refractive Index Sensitivity, Δn as the Change in Refractive Index after Analyte Absorption, d Represents the Effective Adsorbate Layer Thickness, and l_d is the EM Field Decay Length or the Probe Depth of the EM Wave.⁸

Table 1.2

Comparison between SPR and LSPR¹¹

Feature/characteristic	SPR	LSPR
Label-free detection	Yes	Yes
Distance dependence	~1000 nm	~30 nm (size tunable)
Refractive index sensitivity	2×10^6 nm/RIU	2×10^2 nm/RIU
Modes	angle shift wavelength shift imaging	extinction scattering imaging
Requires temperature control	yes	no
Field portability	no	yes
Cost	\$150,000 – \$300,000	\$5,000

Table 1.2

Cont.

Feature/characteristic	SPR	LSPR
Spatial resolution	$\sim 10 \times 10 \mu\text{m}$	nanoparticle
Real-time detection	time scale = $10^{-1} - 10^3 \text{ s}$	time scale = $10^{-1} - 10^3 \text{ s}$
Multiplexed capabilities	yes	yes
Small molecule sensitivity	good	better

Excitation of Surface Plasmon Polaritons

There are several ways to excite SPPs. The earliest method was to use a beam of electrons. While this method worked, it is not feasible for POC analysis. Excitation of SPPs using light is much more economical and portable. Most methods of SPP excitation with light relies on a narrow bandwidth fixed wavelength, i.e., a laser. The devices would be cheaper and simpler if broadband white light was used, as the bulky optics could be removed. Light cannot directly excite a SP due to the momentum mismatch between the massless photon and the natural frequency of the electronic oscillation. As Figure 1.2 shows, the dispersion relation gives some insight into how to excite a SPP. The light line (light blue in Figure 1.2) shows the energy/momentum relationship for incident light in air. By increasing the wavevector, and thus the momentum (Figure 1.2, purple line), we can excite SPPs.

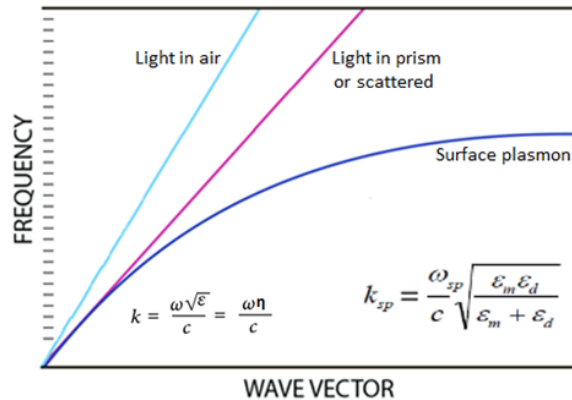


Figure 1.2. The Dispersion Relation for Frequency (ω) vs. the Wavevector (κ). The Wavevector is Directly Proportional to the Momentum of the Incident Light and Indirectly Proportional to the λ . Light Blue Light is Governed by the Bottom Left Equation and is the Dispersion Relation for Light Propagating through Air. The Purple Line is the Dispersion Relation for Light Propagating through a Prism or Scattered Via a Grating or Nanostructures. The Dark Blue Line is the Dispersion Relation for Surface Plasmon Polaritons (SPPs) On a Thin Metallic Film. SPPs Follow the Equation on the Bottom Right of the Plot. Figure Redrawn from Reference.⁷

Figure 1.3 shows the four methods to excite a SPP with light. A high refractive index prism acts by shortening the wavelength, increasing the wavevector, which increases the momentum, giving a momentum matching condition. The two prism coupling methods (Figure 1.3A, 1.3B) are efficient couplers but require extensive optical instrumentation. Other ways to shift the light line is by scattering affects. Figure 1.3C shows a grating coupler which matches the momentum due to scattering, but have an incident angle dependence for the exciting light and low signal to noise ratio. Figure 1.3D represents subwavelength nanostructures as the coupler and is our proposed method due to the small footprint and incident angle independence.

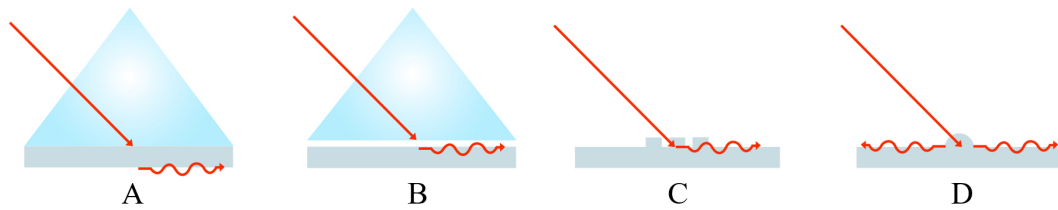


Figure 1.3. The Four Methods to Excite SPPs with Photons. (A) Kretschmann Prism Configuration, (B) Otto Prism Configuration, (C) Grating, (D) Subwavelength Nanostructures.

Emphasis through the entire dissertation will be placed on nanostructured films, as opposed to free nanoparticles. This is because patterned films are easily incorporated into microfluidic systems. This is critical for the design of a point-of-care biosensor. Additionally, nanostructured films afford access to both localized resonance (LSPR) and a propagating surface plasmon polariton (SPP). Nanostructuring a metal film has displayed enhanced sensitivity and afforded inexpensive, portable sensing devices.¹²

Extraordinary Optical Transmission (EOT)

Extraordinary optical transmission (EOT) is the enhanced transmission of light through apertures.¹³ Classically these subwavelength apertures are not expected to transmit in the visible wavelength regime. The periodic arrangement of these apertures allows for several orders of magnitude increase in the far-field transmission. The effect is due to surface plasmons and constructive interference of the oscillating charge density waves. In 1998 Ebbensen's group found that much more light gets through a periodic array of subwavelength apertures than classically predicted by Bethe's theory.^{14,15} Ebbensen's group used a square array of 150 nm holes milled into a 200 nm thick silver

film (Figure 1.4A). Their results, now corroborated by other groups, showed strong enhancement of the transmitted light due to coupling to surface plasmons in the metal film. This seminal publication spawned a lot of research in the EOT area.^{16,17,18,19} A few years later the same group investigated a bulls-eye nanostructure (Figure 1.4B) and showed a 10 fold improvement in the transmission compared to the nanoholes alone, further demonstrating that tailoring the structure alters the transmission properties.²⁰ The EOT effect was used by Brolo et al. for the use in biosensing for the first time in 2004.²¹ They changed the spacing between the nanoholes from 510 nm to 618 nm with 200 nm diameter holes. It is now well known that the EOT effect has a strong dependence on the nanostructure shape, size and periodicity. These parameters are defined in the fabrication process and can lead to control over the transmission and the resonant peak location.

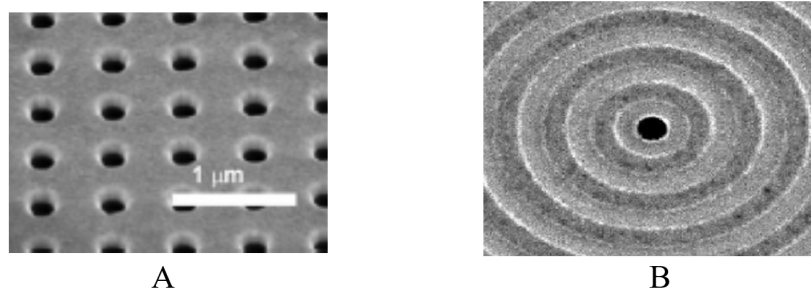


Figure 1.4. Ebbensen's Group (A) Square Array of Nanoholes from the Seminal Paper in 1998 and (B) Bulls-eye Array from the Later Work in 2001.^{15, 20, 22}

EOT is directly applicable to transmission SPR (tSPR) using a broad band light source and measuring a shift in the resonant peak's wavelength after a RI change, due to binding events (Figure 1.5B). Transmission mode SPR affords a much simpler

instrumental design (Figure 1.5A) and allows for a POC system via ease of miniaturization. The other benefit of using tSPR is that we can attain two modes of SPs. The propagating surface plasmon polariton (SPP) mode and the local surface plasmon resonance (LSPR) mode.

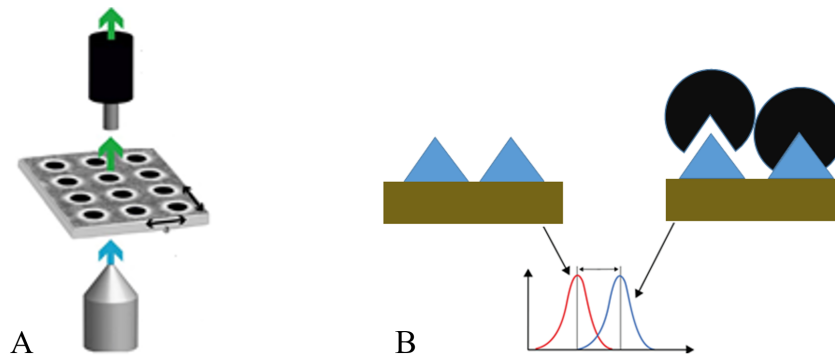


Figure 1.5. (A) Instrumental Setup with Incident Broadband Light from Underneath the Substrate Exciting Surface Plasmons in the Nanohole and Nanoslit Arrays and the Collected Light is Measuring with a Spectrophotometer. (B) The Principle of Wavelength Shift SPR. The Gold Surface is Covered with Ligands (Blue Triangles). After a Binding Event (Black Circles) the Refractive Index of the Surface Changes and Yields a Shift in Resonant Wavelength.²²

Nanostructured Substrate Designs

One of the primary goals of the research was to investigate and vary the type of nanostructure shape, the nanostructure spacing (periodicity), alloy composition, and the nanostructure pore size. The numerical modeling method of finite difference time domain (FDTD) served as a means for rapid design and simulation. FDTD is a versatile modeling technique that solves Maxwell's equations to attain the plasmonic modes for SPR. FDTD is a time-domain technique where a single simulation can provide results from a wide

range of frequencies and wavelengths. This is beneficial as the resonant frequency and primary SP peak are unknown when faced with many variables such as slit width, period, material composition, bimetallic ratio, etc. FDTD provides fundamental understanding of the EM waves and SP modes along with movies and images of how the EM modes evolve over time. Lastly, FDTD provides a quick way for the experimentalist to gain some insight into what devices to fabricate and further investigate. Nanostructures of interest are the nanoslit and the nanoledge (Figure 1.6). In chapter two we will be introduced to the work on bimetallic devices. The bimetallic devices will be compared to the control device (Ag chip) on the basis of sensitivity. In chapter three we will be introduced to a novel design, a nanoledge. This is a stair-step feature. This design has a large pore opening of 280 nm and an inner slit of 50 nm in width. The primary benefit of this design is in the fact that the large pore opening (280 nm in width) is large enough to easily allow the entry of charge analytes, such as proteins in an aqueous solution. These charged analytes form an electrical double layer in solution. The overlap of this charged layer within the nano-sized aperture opening becomes an issue when trying to accommodate charged analytes. The 50 nm slit is needed because researchers have found that slits with a width less than 100 nm provide strong SPR signals.²³

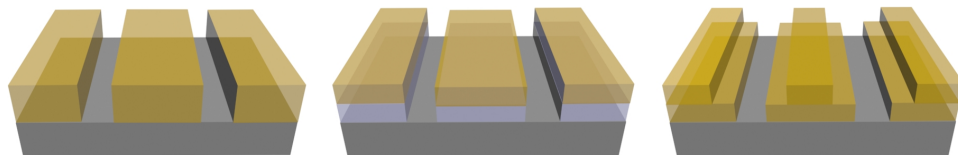


Figure 1.6. Gold Nanoslit, Bimetallic Nanoslit, and Gold Nanoledge.

Instrumentation Setup

Figure 1.7A shows the instrumentation used for the optical measurements in transmission mode SPR. The simplicity of the instrumentation allows for ease of miniaturization and portability. The instrument consists of a miniature light source, fabricated biosensor chip, and a spectrometer, all of which is connected with fiber optic cables. Figure 1.7B displays the method of spectral sensing. White light consisting of all wavelengths is incident on the nanostructured thin film. The surface plasmons are activated and give the extraordinary optical transmission (EOT) and a resonant peak (Figure 1.7B). This process is governed by the mathematics in Equation 1.2.²⁴

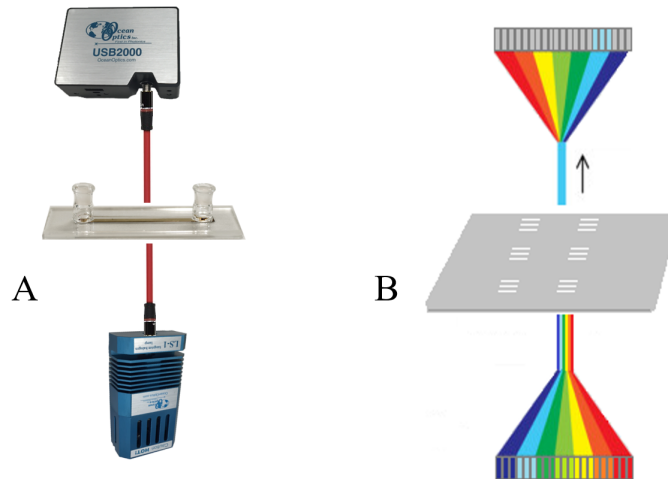


Figure 1.7. Instrumentation and Setup for Sensing in Transmission SPR. (A) The Instrumentation Consists of a Portable Light Source (Ocean Optics LS-1) with Tungsten Bulb, Fabricated Chip with Flow Cell, Fiber Optic Cables and Spectrophotometer (Ocean Optics USB2000). (B) Drawing of the Setup Shows White Light (All Wavelengths) Incident on Metal Film. Due to the Plasmons and Constructive Interference, the EOT Effect is Achieved. Governed by Equation 1.2, a Resonant Peak is Detected (Light Blue Line).

$$\lambda_{SP} = P \sqrt{\frac{\epsilon_m \cdot \epsilon_d}{\epsilon_m + \epsilon_d}} = P \sqrt{\frac{\epsilon_m \cdot \eta^2}{\epsilon_m + \eta^2}}$$

Equation 1.2. The Resonant Surface Plasmon Wavelength is Governed by the Above Equation. λ is the Resonant Wavelength, P is the Periodicity of the Nanostructures, ϵ_m is the Dielectric Constant of the Metal, ϵ_d is the Dielectric Constant of Sensing Area (the Aqueous Media above the Metal), and n is the Refractive Index.²⁴

Brief Introduction of Each Chapter

The following chapters are all in the area of surface plasmon resonance bio-detection, microfabrication, and/or nanofabrication. A brief introduction to each chapter is outlined below.

A bimetallic (Ag/Au) thin film substrate with nanoslits was examined in chapter two for an increase in sensitivity over a gold nanoslit device. To address this point, devices were made with a 100 nm film thickness and milled with nanoslits either 50 nm or 100 nm in size. Devices were also made with various periodicities (spacing between each slit). Experimental optical transmission data and FDTD simulation data was compared on the basis of nanoslit period to corresponding peak wavelength value. The stability of the bimetallic system was investigated for any inter-diffusion between the gold and silver layers. The effect of temperature and age was also investigated. To compare the sensitivity the bimetallic chips and the gold chips were compared on the basis of their peak wavelength shift with solutions of increasing glycerol content, and thus increasing refractive index. Finally, a self-assembled monolayer was used to gain insight on the SPR performance of the bimetallic chip in comparison to the gold chip.

A novel nanoledge design was used in chapter three to examine its ability to allow entry and trapping of protein molecules. TIRF (Total internal reflection fluorescence) microscopy was used to investigate if fluorophore labeled proteins can actually make entry into the nanostructures. A SiO₂ capping layer was introduced in order to promote the binding of SAMs and thus the bio-detection of proteins within the slit and not on the planar upper portion of the thin film. Finally, a monoclonal antibody for free-prostate specific antigen (f-PSA) was attached to the surface and the nanoledge structure was probed for its detection capabilities.

Chapter IV is a technical chapter that addresses the microfabrication of a flow-over fluidic dam. A flow-over fluidic dam was suggested for its ability to decrease diffusion times of analytes to the sensing area. Flow-through fluidic structures have been suggested in the past. Their primary downfall is their ability to clog when working with solutions with “sticky” biological such as large red blood cells. Several microfabrication approaches are discussed and non-traditional fabrication techniques such as multi-layered resist structure formation are discussed.

Biosensing for troponin T, a myocardial infarction biomarker, is investigated in Chapter V. The flow-over fluidic dams with nanoledge structures milled in the top are assessed with confocal microscopy for their ability to allow microspheres (similar in size to red blood cells) to pass over the fluidic dams. A DNA aptamer specific for troponin T was attached to the sensor surface via SAM chemistry. SPR resonant peak shifts were

studied for troponin T binding to the DNA aptamer. This was compared to control solutions of IL-6 protein without troponin T.

Chapter VI is titled “Fabrication of a Plasmonic Photocurrent Device.” This chapter focused on how surface plasmon resonance can influence the photocurrent generating abilities of photosystem I (PSI), a photoactive protein. A device with novel design was needed in order to immobilize PSI into a nanocavity on a gold chip. My contribution was in regards to the design, lithography, etching, and nanofabrication of said device.

References

1. Kirsch, J.; Siltanen, C.; Zhou, Q.; Revzin, A.; Simonian, A., Biosensor technology: recent advances in threat agent detection and medicine. *Chemical Society Reviews* **2013**, *42* (22), 8733-8768.
2. Chao, J.; Chao, J.; Zhu, D.; Zhang, Y. N.; Wang, L. H., DNA nanotechnology-enabled biosensors. *Biosensors & bioelectronics* **2016**, *76*, 68-79.
3. R.K. Arora, R. P. S., Biosensors: Way of Diagnosis. *International Journal of Pharmaceutical Sciences and Research* **2013**, *4* (7), 2517-2527.
4. Mukherji, S.; Shukla, G., Nanoplasmonic biosensors: Current perspectives. *Nanobiosensors in Disease Diagnosis* **2015**, *75*.
5. Sachin K. Srivastava, B. D. G., Fiber Optic Plasmonic Sensors: Past, Present and Future. *The Open Optics Journal* **2013**, *7*, 58-83.
6. Liu, Y.; Liu, Q.; Chen, S.; Cheng, F.; Wang, H.; Peng, W., Surface Plasmon Resonance Biosensor Based on Smart Phone Platforms. *Sci Rep* **2015**, *5*, 12864.
7. Couture, M.; Zhao, S. S.; Masson, J. F., Modern surface plasmon resonance for bioanalytics and biophysics. *Phys Chem Chem Phys* **2013**, *15* (27), 11190-216.
8. Couture, M.; Live, L. S.; Dhawan, A.; Masson, J. F., EOT or Kretschmann configuration? Comparative study of the plasmonic modes in gold nanohole arrays. *Analyst* **2012**, *137* (18), 4162-70.
9. Brolo, A. G.; Brolo, A. G., Plasmonics for future biosensors. *Nature Photonics* **2012**, *6* (11), 709-713.
10. Rycenga, M.; Cobley, C. M.; Zeng, J.; Li, W.; Moran, C. H.; Zhang, Q.; Qin, D.; Xia, Y., Controlling the synthesis and assembly of silver nanostructures for plasmonic applications. *Chem Rev* **2011**, *111* (6), 3669-712.
11. Stuart, D. A.; Stuart, D. A.; Haes, A. J.; Yonzon, C. R.; Hicks, E. M., Biological applications of localised surface plasmonic phenomena. *IEE proceedings. Nanobiotechnology* **2005**, *152* (1), 13.

12. Lee, K.-L., Wang, W.-S. & Wei, P.-K. (2008) Sensitive label-free biosensors by using gap plasmons in gold nanoslits. *Biosensors and Bioelectronics* **2008**, *24* (2), 210-215.
13. Rodrigo, S. G., Extraordinary Optical Transmission. In *Optical Properties of Nanostructured Metallic Systems: Studied with the Finite-Difference Time-Domain Method*, Springer Berlin Heidelberg: Berlin, Heidelberg, **2012**; pp 37-74.
14. Bethe, H. A., Theory of Diffraction by Small Holes. *Physical Review* **1944**, *66* (7-8), 163-182.
15. Ebbesen, T. W.; Lezec, H. J.; Ghaemi, H. F.; Thio, T.; Wolff, P. A., Extraordinary optical transmission through sub-wavelength hole arrays. *Nature* **1998**, *391* (6668), 667-669.
16. van der Molen, K. L.; Klein Koerkamp, K. J.; Enoch, S.; Segerink, F. B.; van Hulst, N. F.; Kuipers, L., Role of shape and localized resonances in extraordinary transmission through periodic arrays of subwavelength holes: Experiment and theory. *Physical Review B* **2005**, *72* (4).
17. Razeghi, M.; Lesuffleur, A.; Im, H.; Lindquist, N. C.; Lim, K. S.; Oh, S.-H.; Mohseni, H., Plasmonic nanohole arrays for real-time multiplex biosensing. **2008**, 7035, 703504-703504-10.
18. Martin-Moreno, L.; Garcia-Vidal, F. J.; Lezec, H. J.; Pellerin, K. M.; Thio, T.; Pendry, J. B.; Ebbesen, T. W., Theory of extraordinary optical transmission through subwavelength hole arrays. *Phys Rev Lett* **2001**, *86* (6), 1114-7.
19. Huang, C.-p.; Wang, Q.-j.; Zhu, Y.-y., Dual effect of surface plasmons in light transmission through perforated metal films. *Physical Review B* **2007**, *75* (24).
20. Thio, T.; Pellerin, K. M.; Linke, R. A.; Lezec, H. J.; Ebbesen, T. W., Enhanced light transmission through a single subwavelength aperture. *Opt. Lett.* **2001**, *26* (24), 1972-1974.
21. Brolo, A. G.; Gordon, R.; Leathem, B.; Kavanagh, K. L., Surface Plasmon Sensor Based on the Enhanced Light Transmission through Arrays of Nanoholes in Gold Films. *Langmuir* **2004**, *20* (12), 4813-4815.
22. Brolo, A., A new method for therapeutic antibody screening. SPIE newsroom **2010**.
23. Lee, K.-L.; Wang, W.-S.; Wei, P.-K. Biosens. *Bioelectron.* **2008**, *24*, 210–215.

24. J. Wei; Kofke, M. S., S.; Waldeck, DH., A Study of Localized Surface Plasmon Resonance Nanoslits Array and Applications for Chip-based Protein Detection. *JSM Nanotechnology and Nanomedicine* **2014**, 2 (2).

CHAPTER II

BIMETALLIC FILMS FOR ENHANCED SENSITIVITY

This chapter has been published as: Taylor Mabe, Zheng Zeng, Bhawna Bagra, James Ryan, Jianjun Wei. "Surface plasmon resonance of a bimetallic nanostructured film for enhanced optical sensitivity." *Chemistry Select.* 2018, 3(11), 3018-3023.

Overview

A bimetallic (Ag/Au) nanoslit film is reported on surface plasmon (SP) generation and refractive index (RI) sensitivity. These were compared to gold devices in transmission surface plasmon resonance (tSPR). The bimetallic films have a primary resonant peak that shifts with periodicity and correlates well with Finite-Difference Time-Domain (FDTD) simulation studies. The SPR of bimetallic nanoslit structures is analyzed via a semi-analytical model. The model enables decomposition and quantitative analysis of SP generation at the aperture under plane-wave illumination. The nanostructured, metallic, thin films provide flexibility to integrate with microfluidics, allowing for simplified instrumentation and alignment. Calculation and experimentation demonstrate that bimetallic films afford an increase in RI sensitivity due to the addition of silver along with the biocompatibility of gold. The Ag/Au films were found to be non-diffusing, long-term stable (over several months), and provided an increase in sensitivity (about 53/RIU) over gold equivalents.

Introduction

Greatly enhanced transmission of light through a subwavelength aperture in a patterned metallic film with a regularly repeating periodic structure underlines the physics of the extraordinary transmission (EOT) phenomena,¹ which results in a variety of applications, such as bio-detection and biosensing schemes.² Nanostructures and nanostructured metal thin films can utilize the phenomena of surface plasmon resonance (SPR) to detect binding events of biomolecules by monitoring a refractive index (RI) change. SPR comes in two forms, a localized mode and a propagating mode. Localized surface plasmon resonance (LSPR) is where electrons oscillate back and forth inside of a nanoscale structure,³ such as nanoparticles,⁴ nanotriangles,⁵ nanostars,⁶ nanohole arrays,⁷ nanotriangle arrays,⁷ and other shapes.^{4, 8} Another form is surface plasmon polariton (SPP) occurred at the interface of a metal and a dielectric. Some techniques are used to accomplish SPP generation with light (photons), including end-fire coupling,⁹ high RI prisms,¹⁰ gratings,¹⁰ or nanostructures.¹¹ A nanostructured planar film has an additional benefit of allowing for transmission mode SPR, which can be easily integrated into microfluidics.¹² Nanostructures in gold planar films have been investigated previously,¹³ such as nanohole, nanocircle, and nanoslit arrays. In regards to sensitivity to RI changes near the surfaces, it was found that the nanoslit array was the most sensitive; 16% higher than the nanohole arrays and 5% higher than the nanocircle arrays.¹³

Metals are the materials of choice in plasmonics, since surface plasmons can couple light strongly to the metal surface and thereby greatly enhance light-matter

interactions.¹⁴ Other materials being investigated for their plasmonic potential include the alkali metals,¹⁵ transparent conducting oxides,¹⁵ and graphene.¹⁵⁻¹⁶ A desirable plasmonic material has a large plasma frequency, high conductivity, high polarizability (large $-\epsilon'$), low ohmic loss (small ϵ''), ability to fabricate nanostructures in the material.¹⁴ Only a few materials are effective at generating surface plasmons.¹⁷ Copper has interband transitions below 600 nm and oxidizes. Aluminum is good in the UV region but also forms oxides. Silver has the highest conductivity, longest SPP propagation distances, and the highest quality factor in the visible region. Gold has interband transitions below 480 nm¹⁸ and is the workhorse of SPR due to its chemical inertness. Compared to gold, silver has higher electromagnetic (EM) fields in the sensing area and less attenuation of its SPP generation. Silver has an added benefit of being shifted to longer wavelengths, into the window of 0.6 μm -1.2 μm . This region is outside of the biological auto-fluorescence region and therefore has an advantage of free of biological interference. A single metal does not possess all of the traits of a high quality plasmonic material, but a bimetallic chip potentially could. A device composed of silver and gold could incorporate the optical and electrical properties of silver underneath an inert layer of gold.

The bimetallic nanostructures provide composition-tunable plasmonic resonances for plasmon-based sensing and surface field-enhanced spectroscopy,¹⁹ and various structures such as core-shell nanoparticles,²⁰ nanoholes,²¹ and nanorods.²² Du et al. performed a theoretical investigation of a planar bimetallic SPR chip and found a 20% increase in the evanescent field strength and an 80% increase in the sensitivity compared

to the gold control chip.^{19a} Sharma et. al. presented a theoretical study of bimetallic nanoparticles and found that the sensitivity was tunable with metal ratio and that Ag/Au had the highest sensitivity of the alloys.^{19c} The Sohn group found that a bimetallic device was twice as accurate as gold equivalents, with peak widths half that of the gold.^{19d} They also showed a two-fold increase in sensitivity and a six-fold improvement in limit of detection (LOD).^{19e} Ong et al. discerned that a bimetallic film had a two-fold improvement in sensitivity over gold.^{19f} Multilayer of gold–silver array of prisms show SPR enhanced near-field fluorescence from quantum dots deposited at the surface of these platforms.^{19h} Murray-Me'thot et al. experimentally demonstrated the improved optical properties of Au/Ag bimetallic nanohole arrays over pure Au or Ag nanohole arrays and found the dependence of excitation wavelength, the RI sensitivity, and the transmission full width at half-maximum (FWHM) on the metal compositions.²¹ Kim et al. reported the tunability of surface plasmon by composition variation in nanorod structures and investigated the metallic composite impact on both the far-field and near-field scattering spectra.²²

The efficiency of surface plasmon (SP) generation of bimetallic systems and its effect on the sensitivity are rarely explored. This study presents an investigation of bimetallic (Ag/Au) nanoslit films with a focus on optical properties and RI sensitivity as a comparison to pure gold nanoslit films in light transmission measurements. A semi-analytical analysis and a Finite-Difference Time-Domain (FDTD) simulation were used to estimate the SP generation and optical response, respectively, for providing a

fundamental understanding of the dielectric sensitivity of these devices. The findings in this work show that bimetallic nanostructures can be attuned to enhance the sensitivity in surface plasmon resonance.

Results and Discussion

Metallic Nanoslit Film and Characterization

Metallic nanoslit films in Au and Ag/Au bimetallic were designed and fabricated. Figure 2.1 shows the structure and scanning electron microscopy (SEM) images for various periodicities (550 nm, 600 nm, 650 nm, and 700 nm) at 50 nm slit widths. The metal film was 100 nm thick. The SEM images clearly show straight nanoslit arrays in metallic films.

Stability of the bimetallic layers is important for this research. It is documented that silver and gold readily diffuse into one another in liquid and solid states.²³ Secondary ion mass spectrometry (SIMS) was used to investigate grain boundary diffusion of silver into gold in these bimetallic films. SIMS samples consisted of a range of Ag: Au ratios and covered a range of ages over a period of 10 months. Figure 2.1 shows that little inter-diffusion was observed for any of these films. The results of the SIMS analyses support the hypothesis that there is a distinct bimetallic interface and that the bimetallic film does not change over time. A clean, distinct bimetallic interface also helped simplify the simulation studies and experiments.

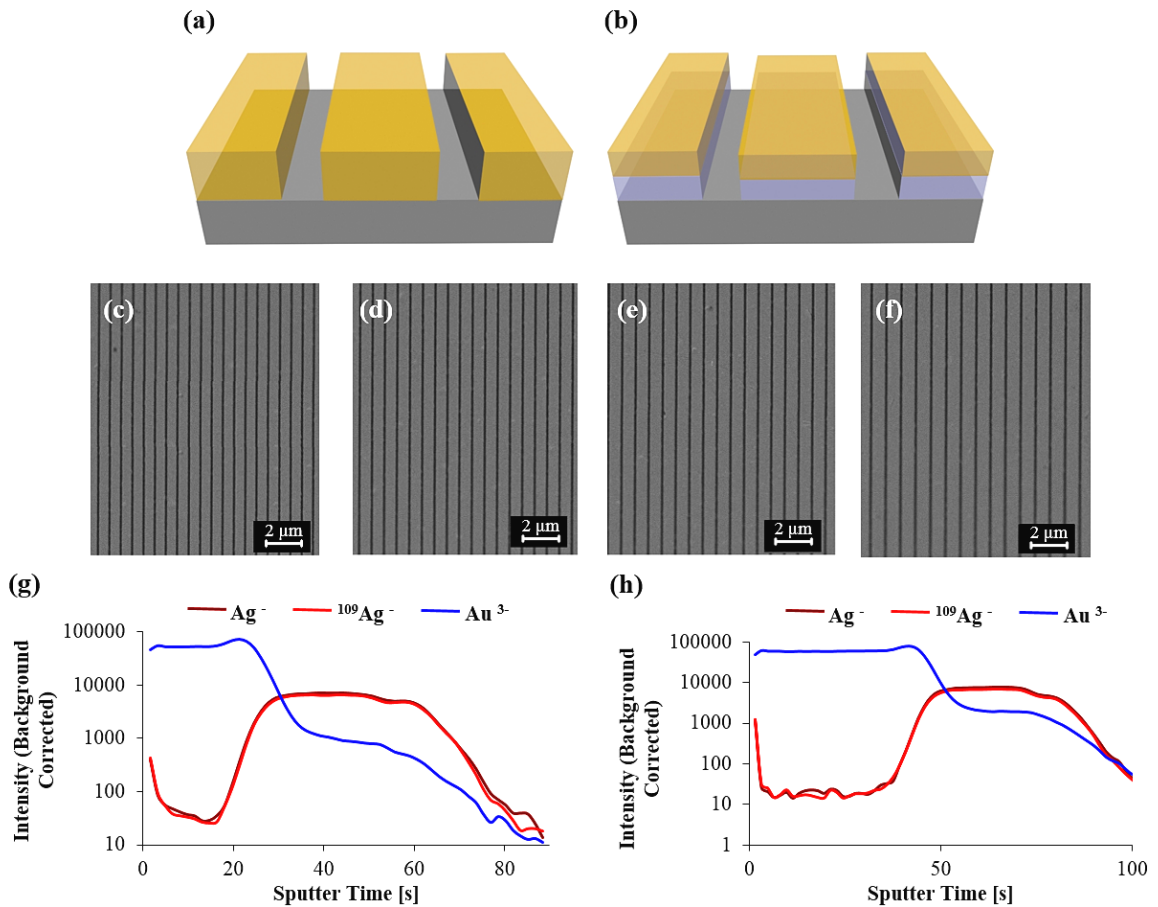


Figure 2.1. A Schematic Drawing of (a) Gold Nanoslit Structure and (b) Bimetallic Nanoslit Structure. SEM Images of a Representative Ag/Au Bimetallic Nanoslit Array with 50 nm Width and a Periodicity of (c) 550 nm (d) 600 nm (e) 650 nm (f) 700 nm. Results of SIMS Analysis for Two Ag/Au Bimetallic Devices (g) 9 Months after Fabrication and (h) 10 Months after Fabrication. (SEM Images of Au Nanoslit Devices in Figure A1, Appendix A.)

Transmission SPR Spectra

The bimetallic substrates showed a strong correlation between nanoslit period and transmission peak wavelength (Figure 2.2a). This is consistent with the FDTD results (Figure 2.2b). The primary resonant peak wavelength values were plotted as a function of

nanoslit period for FDTD results and experimental results (Figure 2.2c). There is a linear relationship between the nanoslit period and the primary resonant peak wavelength, which can be explained by the following Equation:¹³

$$\lambda_{SP} = P \sqrt{\frac{\epsilon_m \epsilon_d}{\epsilon_m + \epsilon_d}} = P \sqrt{\frac{\epsilon_m n^2}{\epsilon_m + n^2}}, \quad (\text{Eq. 1})$$

where λ_{SP} is the resonant surface plasmon wavelength, P is the periodicity between the nanostructures, ϵ_m is the dielectric constant of the metal, ϵ_d is the dielectric constant of the liquid dielectric (the sensing area), and n is the RI.²⁴ The aqueous media above the metal makes up ϵ_d . Hence, increasing the periodicity will result in increased primary resonant peak wavelength.

The EOT of a thin film nanostructure is important for SPR-based sensing. To verify that age would not adversely affect the optical properties of the bimetallic nanoslit films, transmission SPR (tSPR) spectra were collected in air over a 3-week period with no notable shift in the primary resonant peak wavelength. Furthermore, the tSPR spectra were collected in wavelength shift mode, which is temperature independent, as verified in Figure 2.2e. Ethanol-water mixtures were passed over a chip with 50 nm slits and a 550 nm periodicity for the temperature investigation. The temperature was altered with a heat gun and monitored by two thermocouples, with one placed on the chip and a second measuring the atmospheric temperature inside of an enclosed experimental box. The primary peak at 856 nm does not have an obvious shift between 27 °C and 38 °C,

indicating its good stability at about 30 °C. In addition, the heating is primarily applied to the metallic film and not the flowing ethanol-water solution. Coupled with the SIMS results above, the bimetallic nanoslit films showed non-diffusing and long-term stable properties.

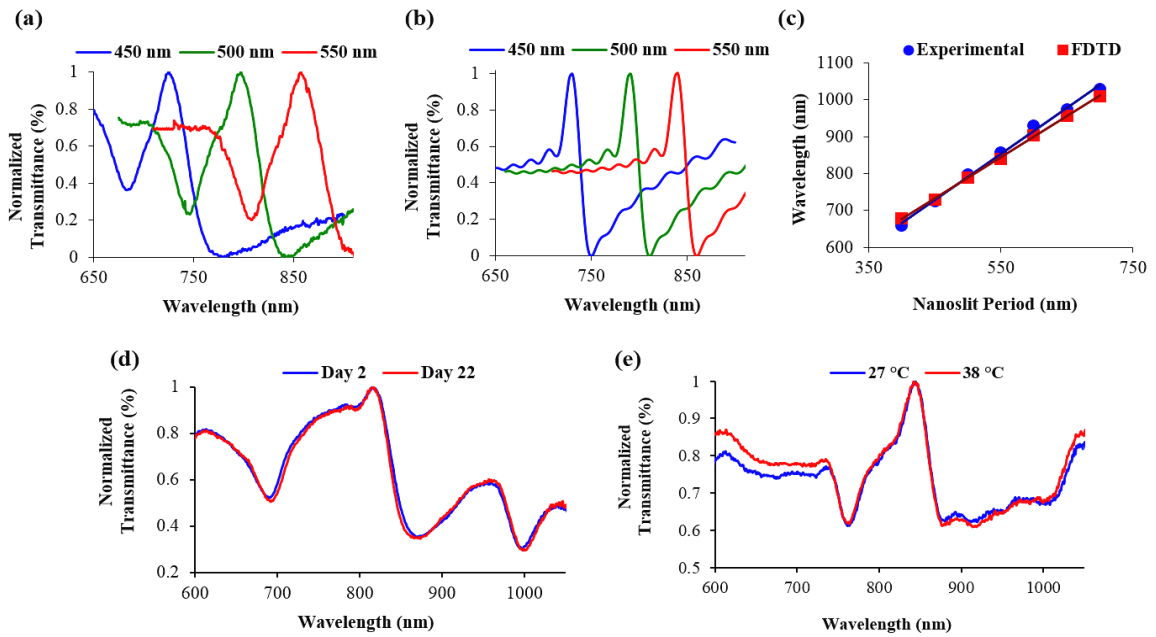


Figure 2.2. **(a)** Experimental and **(b)** FDTD Simulation Results Showing the Correlation of Resonant Peak Position with Nanoslit Period for 450 nm, 500 nm, and 550 nm Period Arrays. **(c)** Correlation of the Primary Resonant Peak Wavelength with Nanoslit Period for FDTD Simulation and Experimental Data. **(d)** Transmission Spectrum of a Bimetallic Chip with 50 nm Slits Collected in Air for Investigation of Optical Stability over Time. **(e)** The Effect of Temperature on Spectral Output Using 50 nm Slits in an Ethanol-Water Solution.

SP Generation Analysis of Metallic Nanoslit Films

It is important to study the SP generation of the metallic nanoslit films with respect to tuning the optical transmission and its sensitivity to the dielectric environment.

There are several parameters that can be adjusted to enhance the RI sensitivity in surface plasmon resonance.²⁵ Regarding the geometric diffraction with the bounded SPP modes launching on the flat interfaces surrounding the slits, a mechanistic description for SP generation is needed, especially the SPP scattering coefficients and efficiencies at the slit apertures. Note that SP generation efficiency is defined as the rate of SPP launching, propagation and scattering by matching the continuous electromagnetic fields quantities at the interface.²⁶ The schematic (Figure 2.3a,b) illustrates the parameters for the nanoslit structure and SP generation by a plane wave at normal incidence.

The w represents the slit widths, and the $\alpha^-_{(top)}$, $\alpha^+_{(top)}$, $\alpha^-_{(Ag)}$, $\alpha^+_{(Ag)}$, $\alpha^-_{(Au)}$, $\alpha^+_{(Au)}$ represent the SP generation coefficients at the two interfaces (red and blue arrows, respectively) with inverse propagation directions. The refractive indexes inside the slits and at the outer slits are presented by n_{air} of 1, and that for the SiO_2 is presented by n_{SiO_2} of 1.41.²⁷ Note that we focus on the SP generation at the flat metal/medium interfaces upon light excitation without considering subwavelength thickness of the metallic film.

The SP generation efficiency values (e) at the Ag– SiO_2 and Au– SiO_2 interfaces are plotted as a function of wavelength λ and scaled width w' from the visible to near-infrared (600-1200 nm) obtained by the semi-analytical model, with Ag– SiO_2 interface as $e_{(Ag)}=|\alpha^-_{(Ag)}(w/2)|^2=|\alpha^+_{(Ag)}(w/2)|^2$ (Figure 2.3c), Au– SiO_2 interface as $e_{(Au)}=|\alpha^-_{(Au)}(w/2)|^2=|\alpha^+_{(Au)}(w/2)|^2$ (Figure 2.3d), the $e_{(top)}$ as the same for both two nanoslit structures (Figure A2, Appendix A).

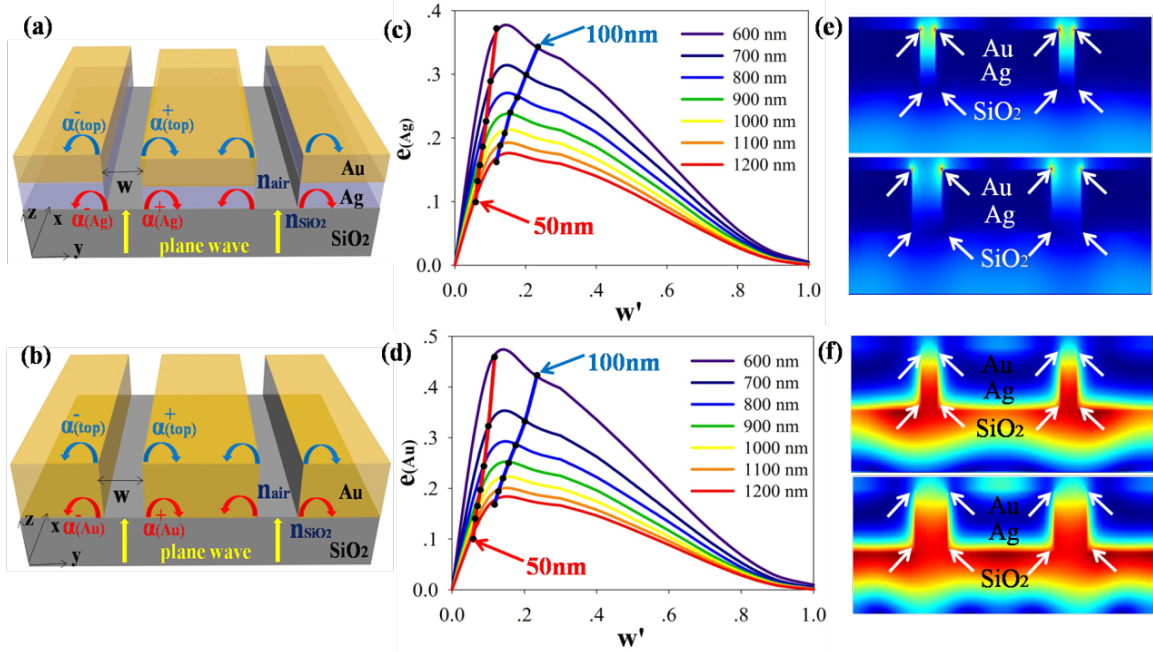


Figure 2.3. Semi-Analytical Analysis of SP Generation and FDTD Simulation of Nanoslit Array. **(a)-(b)** The Schematic Illustrates the Parameters for the Nanoslit Structure and Surface Plasmon Generation by a Plane Wave at Normal Incidence. **(a)** Bimetallic Nanoslit Structure. **(b)** Au Nanoslit Structure. **(c) - (d)** The SP Generation Efficiencies e at the Ag–SiO₂ and Au–SiO₂ Interfaces are Plotted as a Function of Wavelength λ and Scaled Width w' Obtained by the Semi-analytical Model. **(e) - (f)** FDTD Simulation of Transverse Electro-magnetic Field Intensity for the 50-450 nm Bimetallic Nanoslit Structure and 100-450 nm Bimetallic Nanoslit Structure with Hot Spots as White Arrows Shown. **(e)** Transverse Electric Field Intensities of 50-450 nm Nanoslit Structure (top) and 100-450 nm Nanoslit Structure (Bottom). **(f)** Transverse Magnetic Field Intensity of 50-450 nm Nanoslit Structure (Top) and 100-450 nm Nanoslit Structure (Bottom).

The SP generation is efficient at visible frequencies while e rapidly decreases with the increase of wavelength. Moreover, at a visible wavelength of 600 nm, the SP generation efficiencies are 0.372 at Ag–SiO₂ interface, 0.457 at Au–SiO₂ interface for 50 nm slit width and 0.346 at Ag–SiO₂ interface, 0.429 at Au–SiO₂ interface for 100 nm slit width. However, with the increase of wavelength, the SP generation efficiencies for 50

nm slit width are smaller than those for 100 nm slit width. It is expected that the total SP generation efficiency (e) will result from a “superposition” of the SPP arising from all the interfaces of the nanoslit structure. The maximum e is calculated as 0.603 (50 nm slit width) and 0.569 (100 nm slit width) for the bimetallic nanoslit structure with the incident wavelength of 600 nm. In contrast, FDTD simulation of transverse electro-magnetic field intensity for the 50-450 nm bimetallic nanoslit structure and 100-450 nm bimetallic nanoslit structure with hot spots were plotted as Figure 2.3e,f. Compared to gold nanoslit structure (Figure A3), the electro-magnetic field distributions reveal that the plasmonic excitations arise from the Ag-SiO₂ interface and the Au/air interfaces with the strength of Ag-SiO₂>Au-air, which is consistent with the results of the semi-analytical model for SP generation efficiencies of $e_{\text{Ag}} > e_{\text{top}}$ for the bimetallic nanoslit structure.

Responses to Refractive Index Changes

To compare the bulk sensitivity between gold and bimetallic devices, a series of glycerol-water solutions (0%-20%) were made, since glycerol-water mixtures have a linear relationship between RI and increasing glycerol percentage. The results for 50 nm slit, 450 nm period devices are shown for gold (Figure 2.4a) and for bimetallic (Figure 2.4b) chips. The slope of the plots in Figure 2.4c and 2.4d show that the gold chip had a sensitivity of 473 nm/RIU while the bimetallic was 526 nm/RIU, which agrees with the reports of bimetallic layer vs. single gold layer for fiber-optic or waveguide SPR sensors.^{19f, 19g} And the sensitivity of bimetallic nanoslit array here is much higher than that obtained by the bimetallic nanohole array (269 nm/RIU) for tSPR sensors.²¹

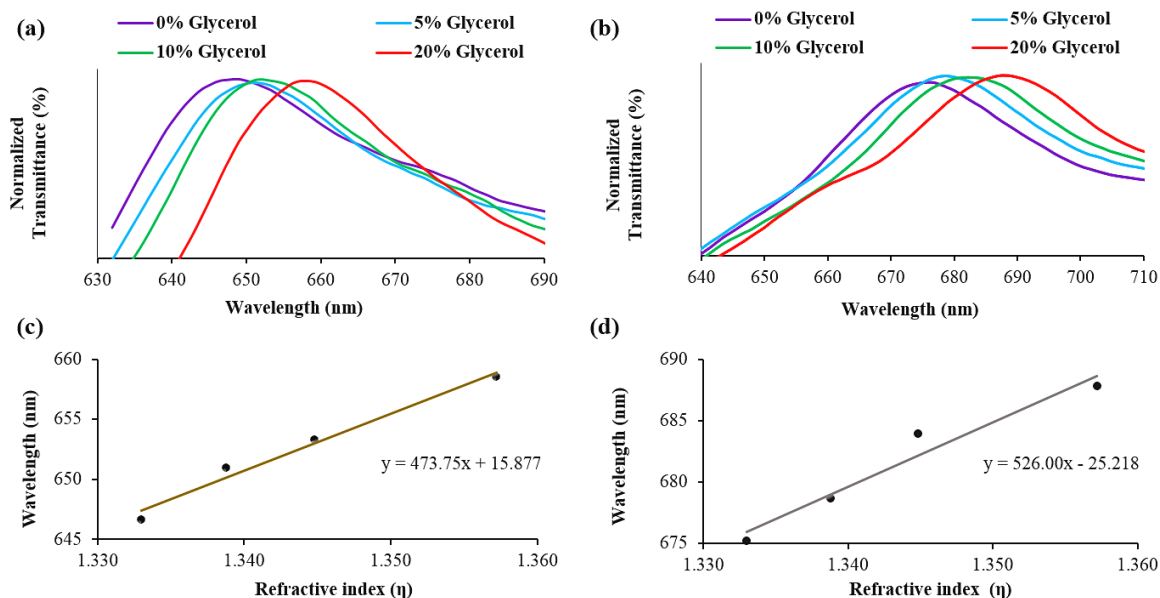


Figure 2.4. Transmission Spectra of (a) Au and (b) Ag/Au Devices in Glycerol/Water Solutions. Sensitivity Determination for (c) Au and (d) Ag/Au Devices.

The surface sensitivity was further investigated by use of self-assembly. A clean nanoslit device (Figure 2.5a) was then exposed to 16-mercaptohexadecanoic acid (16-MHDA) which was used as a self-assembled monolayer (SAM). A schematic of a nanoslit device with bound SAM is shown in Figure 2.5b. The binding event was monitored by a shift in the resonant peak wavelength and the gold chip had a peak wavelength shift of 2.5 nm while the bimetallic was 6.5 nm (Figure 2.5c). Note that 5 mM of the thiol, in ethanol, was flushed over the chip with a syringe pump. The total SP generation efficiency change has the similar dependence on the bulk media RI changes as the EOT peak shift. Considering that the RI near the metallic surfaces is increased inside the bimetallic nanoslit structure due to the addition of SAM induced RI change, the red

shift of the optical transmission after SAM formation is correlated to the decreased SP generation efficiency from 0.603 to 0.537.²⁸

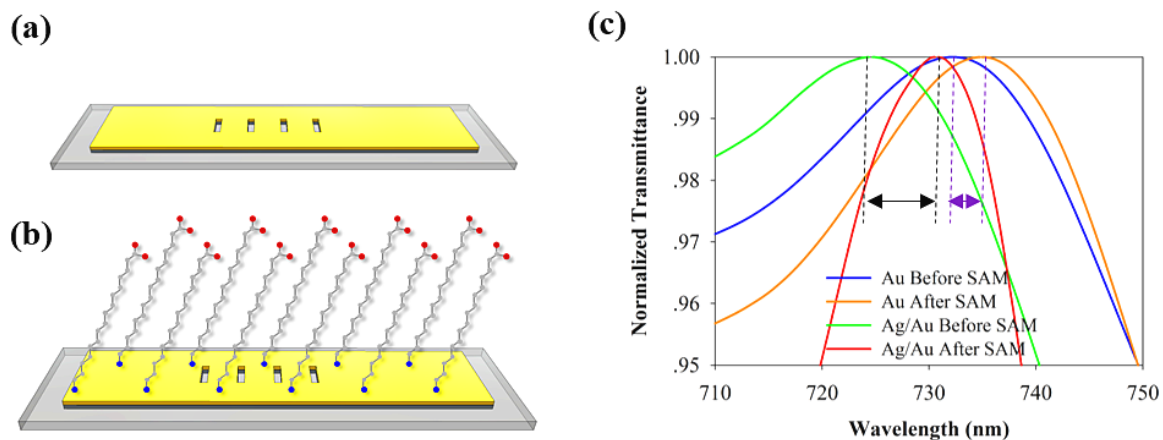


Figure 2.5. Schematic of the Nanoslit Device **(a)** Before Binding of the SAM and **(b)** After the SAM Formation. **(c)** Detection of SAM at the Au and Ag/Au Devices.

Conclusion

SPR on a silver/gold bimetallic substrate was shown to be stable without obvious inter-diffusion. The primary resonant peak was tunable with nanoslit periodicity. Increasing the period increased the resonant peak wavelength. The period to resonant peak wavelength behavior mirrored that of the FDTD simulations studies. The bulk sensitivity and surface sensitivity to RI changes were increased with the bimetallic devices as compared to the gold devices. Alkanethiols self-assembled and afforded a peak shift by the EOT spectra, by which the binding event was monitored. The bimetallic sensor devices were shown to be stable over time, with an improvement in sensitivity

over the gold control devices. The bimetallic substrate afforded the sensitivity of silver along with the chemical stability of gold.

References

1. W. L. Barnes, A. Dereux, T. W. Ebbesen, *Nature* **2003**, *424*, 824-830.
2. D. Habauzit, J. Chopineau, B. Roig, *Anal. Bioanal. Chem.* **2007**, *387*, 1215-1223.
3. Y.-T. Long, *Localized surface plasmon resonance based nanobiosensors*, Springer, Heidelberg ; New York, **2014**.
4. Y. Xia, N. J. Halas, *MRS Bull.* **2005**, *30*, 338-348.
5. A. Paul, B. Kenens, J. Hofkens, H. Uji-i, *Langmuir* **2012**, *28*, 8920-8925.
6. G. Chirico, *Gold Nanostars [electronic resource] : Synthesis, Properties and Biomedical Application*, Springer, Cham, **2015**.
7. D. Correia-Ledo, K. F. Gibson, A. Dhawan, M. Couture, T. Vo-Dinh, D. Graham, J.-F. Masson, *J. Phys. Chem. C* **2012**, *116*, 6884-6892.
8. X. Zheng, Y. Peng, X. Cui, W. Zheng, *Mater. Lett.* **2016**, *173*, 88-90.
9. X. Guo, J. Du, X. Luo, C. Du, Y. Guo, *Microelectron. Eng.* **2007**, *84*, 1037-1040.
10. S. A. Maier, *Plasmonics [electronic resource]: fundamentals and applications*, Springer, New York, **2007**.
11. K. Yu, M. S. Devadas, T. A. Major, S. S. Lo, G. V. Hartland, *J. Phys. Chem. C* **2014**, *118*, 8603-8609.
12. a) Z. Zeng, X. Shi, T. Mabe, S. Christie, G. Gilmore, A. W. Smith, J. Wei, *Anal. Chem.* **2017**, *89*, 5221-5229; b) J. Wei, S. Singhal, D. H. Waldeck, M. J. Kofke, *Vol. US 8158409 B2*, U.S.A., **2012**; c) J. Wei, M. Kofke, M. Rexius, S. Singhal, Y. Wang, D. H. Waldeck, *NSTI-Nanotech.* **2011**, *3*, 79-82.
13. K.-L. Lee, W.-S. Wang, P.-K. Wei, *Plasmonics* **2008**, *3*, 119-125.
14. G. V. Naik, V. M. Shalaev, A. Boltasseva, *Adv. Mater.* **2013**, *25*, 3264-3294.
15. A. Boltasseva, H. A. Atwater, *Science* **2011**, *331*, 290.

16. a) M. Jablan, M. Solja, H. Buljan, *Proc. IEEE* **2013**, *101*, 1689-1704; b) S. Xiao, X. Zhu, B.-H. Li, N. A. Mortensen, *Front. Phys.* **2016**, *11*, 117801.
17. M. G. Blaber, M. D. Arnold, M. J. Ford, *J. Phys. Condens. Matter* **2010**, *22*, 143201.
18. P. R. West, P. R. West, S. Ishii, G. V. Naik, N. K. Emani, *Laser Photonics Rev.* **2010**, *4*, 795-808.
19. a) L. Xia, S. Yin, H. Gao, Q. Deng, C. Du, *Plasmonics* **2011**, *6*, 245-250; b) Y.-H. Su, W.-L. Wang, *Nanoscale Res. Lett.* **2013**, *8*, 1-6; c) A. K. Sharma, G. J. Mohr, *J. Phys. D* **2008**, *41*, 055106; d) Y. K. Lee, K. S. Lee, W. M. Kim, Y. S. Sohn, *PLoS One* **2014**, *9*, e98992; e) Y. K. Lee, D. H. Jang, K. S. Lee, W. M. Kim, Y. S. Sohn, *Nanoscale Res. Lett.* **2013**, *8*, 344; f) B. H. Ong, X. Yuan, S. C. Tjin, *Fiber Integrated Opt.* **2007**, *26*, 229-240; g) Y. Chen, Y. Yu, X. Li, Z. Tan, Y. Geng, *Plasmonics* **2015**, *10*, 1801-1808; h) A. Garreau, M. Tabatabaei, R. Hou, G. Q. Wallace, P. R. Norton, F. Lagugné-Labarthe, *J. Phys. Chem. C* **2016**, *120*, 20267-20276.
20. a) C. Zhang, B.-Q. Chen, Z.-Y. Li, Y. Xia, Y.-G. Chen, *J. Phys. Chem. C* **2015**, *119*, 16836-16845; b) J. E. Lee, K. Chung, Y. H. Jang, Y. J. Jang, S. T. Kochuveedu, D. Li, D. H. Kim, *Anal. Chem.* **2012**, *84*, 6494-6500; c) R. Arenal, L. Henrard, L. Roiban, O. Ersen, J. Burgin, M. Treguer-Delapierre, *J. Phys. Chem. C* **2014**, *118*, 25643-25650.
21. M.-P. Murray-Méthot, M. Ratel, J.-F. Masson, *J. Phys. Chem. C* **2010**, *114*, 8268-8275.
22. D.-S. Kim, S.-H. Ahn, J. Kim, D. Seo, H. Song, Z. H. Kim, *J. Phys. Chem. C* **2016**, *120*, 21082-21090.
23. a) P. A. Turner, H. C. Theuerer, K. L. Tai, *J. Vac. Sci. Technol.* **1969**, *6*, 650-650; b) S. K. Sen, P. M. Klugeweiss, C. L. Bauer, *J. metals* **1979**, *31*, F43-F43; c) M. A. Nicolet, *Thin Solid Films* **1978**, *52*, 415-443.
24. J. Wei, M. Kofke, S. Singhal, D. Waldeck, *JSM Nanotech. Nanomed.* **2014**, *2*.
25. A. Shalabney, A. Shalabney, I. Abdulhalim, *Laser Photonics Rev.* **2011**, *5*, 571-606.
26. a) P. Lalanne, J. P. Hugonin, J. C. Rodier, *Phys. Rev. Lett.* **2005**, *95*, 263902; b) P. Lalanne, J. P. Hugonin, J. C. Rodier, *J. Opt. Soc. Am. A* **2006**, *23*, 1608-1615.

27. a) T. Murata, H. Ishizawa, I. Motoyama, A. Tanaka, *Appl. Opt.* **2006**, *45*, 1465-1468; b) S. Pal, G. De, *Mater. Res. Bull.* **2009**, *44*, 355-359.
28. Z. Zeng, M. N. Mendis, D. H. Waldeck, J. Wei, *RSC Adv.* **2016**, *6*, 17196-17203.

CHAPTER III

PROTEIN SENSING IN NANOEDGE STRUCTURES

This chapter has been published as: Zeng, Z.[#], Shi, X.[#], Mabe, T.[#], Gilmore, G., Smith, A. W., & Wei, J. (2017). Protein Trapping in Plasmonic Nanoslit and Nanoledge Cavities: The Behavior and Sensing. *Analytical Chemistry*, 89(10), 5221-5229. [#] Equal contribution.

Overview

A novel plasmonic nanoledge device was presented to explore the geometry-induced trapping of nanoscale biomolecules and examine a generation of surface plasmon resonance (SPR) for plasmonic sensing. To design an optimal plasmonic device, a semi-analytical model was implemented for a quantitative analysis of SPR under plane-wave illumination and a finite-difference time-domain (FDTD) simulation was used to study the optical transmission and refractive index (RI) sensitivity. In addition, total internal reflection fluorescence (TIRF) imaging was used to visualize the migration of fluorescently labeled bovine serum albumin (BSA) into the nanoslits; and fluorescence correlation spectroscopy (FCS) was further used to investigate the diffusion of BSA in the nanoslits. Transmission SPR measurements of free prostate specific antigen (f-PSA), which is similar in size to BSA, were performed to validate the trapping of the molecules via specific binding reactions in the nanoledge cavities. The present study may facilitate

further development of single nanomolecule detection and new nano-microfluidic arrays for effective detection of multiple biomarkers in clinical biofluids.

Introduction

The latest advances in manipulation, trapping, alignment, and separation of molecules embrace fields as diverse as quantum optics, soft condensed-matter physics, biophysics and clinical medicine.^{1,2} Many technologies, whether active techniques (external fields) or passive ones (hydrodynamic interactions or inertial effects),³⁻⁷ have been developed to counter and trap the Brownian motion of small molecules in solution. However, confinement of nanomolecules in the absence of external fields and visualizing the dynamics of nanomolecules in the nanometric-sized objects remain challenging. Total internal reflection fluorescence (TIRF) imaging could be a potential solution to these challenges, since the incident light creates a thin surface electromagnetic field (around 100 nm) enabling the detection of only the labeled fluorophores that are within the nanometric depth. In addition, fluorescence correlation spectroscopy (FCS), a time-resolved fluorescence method, could analyze the temporal fluctuations due to diffusion of fluorophores in and out of a nanostructure. This is done by utilizing a confocal laser beam with ~ 0.2 fL of volume to detect the diffusion of particles crossing the laser focus.⁸⁻¹¹ The recorded fluorescence fluctuations are then correlated for analysis, directly yielding information about the mobility of the diffusing particles.¹² Recently, FCS has been applied to measure tracer diffusion in nanofluids¹³ and to investigate membrane dynamics through nanoapertures.¹⁴

For practical purposes, stable nanomolecule trapping and detection have received intense attention because of the focus on in-vitro detection of target molecules. This approach makes use of the versatility of optical sensing and also the convenience of nanoplasmonic-chip-based device integration with different nanostructures, including pores, channels and slits.¹⁵⁻¹⁸ The useful phenomenon, which underlies the ability of such nanoapertures to light with high efficiency, is transmission surface plasmon resonance (T-SPR), which has sparked an interest in deeply understanding the fundamentals of T-SPR physics,¹⁹⁻²¹ and encouraged researchers to explore new ways for nanoscale molecule trapping, and creating novel, robust nanoscale sensors.²²⁻²⁵ It has been recently understood that nanoplasmonic devices, with strong plasmon excitation and stable convective trapping of nanomolecules, can be especially suitable for applications if they incorporate real metals with a finite conductivity,²⁶ sufficiently high intensity of light scattering,²⁷ extraordinary optical transmission (EOT),^{28,29} high refractive index (RI) sensitivity at the perforated metal films,³⁰ and a single nanometer-scale pore for single molecule thermodynamics and kinetics.³¹

Here, we present and investigate novel nanoledge aperture structures for convective molecular trapping and implement a quantitative analysis of surface plasmon (SP) generation using an earlier developed semi-analytical model.³² In addition, we perform numerical simulations using a finite-difference time-domain (FDTD) method to model optical transmission spectra and RI sensitivity as a function of the nanoledge device geometrical parameters.³³ Experimentally, we used the techniques of TIRF to

visualize the migration of Texas Red-labeled bovine serum albumin (TxR-BSA) molecules into the nanoslits and FCS to detect its dynamics in nanoslits with different widths. Later, the molecular trapping and sensing in the nanoledge structure were validated using a fabricated sub-wavelength gold-film nanoledge device which was integrated with a microfluidic channel allowing us to measure the SPR induced optical transmission, RI sensitivity, and detect the specific binding events of free prostate specific antigen (f-PSA) biomarkers to the gold surfaces functionalized with antibody of f-PSA in the nanoslit cavities.

Methods and Materials

Semi-analytical Analysis of SP Generation and FDTD Simulations

The SP scattering coefficients and efficiencies at the slit apertures can be determined from the analysis of diffraction of bounded SP modes originated on the flat interfaces surrounding the slits in order to study nanoledge geometries that are of interest in practice and consider the geometric diffraction with the bounded SP modes launching on the flat interfaces surrounding the slits. Moreover, FDTD simulations reiterated the previous study by adding additional 10 nm SiO₂ film at the top of Au layer.³² Refractive index of the SiO₂ film used in calculations was equal to 1.41. More details of the semi-analytical model analysis applied to the SiO₂ film topped nanoledge devices and results are provided in Appendix B.

Fabrication of Ledged Flow-through Nanoplasmonic Device

Standard photolithography was used to pattern soda lime glass slides (75x25 mm, Globe Scientific). Slides were fully covered with a 600 nm layer of aluminum by DC sputtering (PVD 75, Kurt Lesker). A dark field mask was designed in AutoCAD and printed on a transparency film using a 25400 dpi printer. The mask design, shown in Figure B5 in Appendix B, consisted of a flow channel with two dam structures, each of which was 30 μm wide. Shipley 1827 positive photoresist was applied to hexamethyldisilazane (HMDS) treated glass slides by spin coating. The slides were then exposed with deep UV using an OAI 8800 mask aligner and developed with Microposit MF-321 developer. The aluminum layer was wet etched using Aluminum Etchant Type A (Transene Company) and the glass was then wet or dry etched to yield an isotropic or anisotropic dam structure, respectively. This process is fully outlined in Figure B6. The patterned glass slides were covered with 2 nm Ti, 150 nm Au, and 10 nm of SiO_2 by electron beam evaporation (PVD75, Kurt Lesker). Focused ion beam milling (Zeiss, Auriga) was used to introduce the nanoledge structures atop the 30 μm dams. A slit, 50 nm wide, was milled completely through the SiO_2 and gold layers, followed by a 280 nm wide ledge that was milled through the SiO_2 and partially through the gold layer. The nanoledge channel was completely aligned with the direction of microchannels. The device was then enclosed using a poly(dimethylsiloxane) (PDMS) flow channel, which was also fabricated using standard lithographic techniques.³⁴

Total Internal Reflection Fluorescence (TIRF) Imaging

Nanoslits were fabricated by FIB on a glass coverslip. The coverslip soaked in detergent solution and IPA/water (50:50) accordingly. The coverslip was rinsed with excess Type I water and dried under nitrogen stream. Ozone plasma was used to further clean the surface of the coverslip. The coverslip was assembled in the AttoFluor sample chamber. TIRF imaging was recorded on a Nikon Eclipse Ti inverted microscope equipped with a 2 mW 488 nm diode laser (85-BCD-020-115, Melles Griot) and 100X TIRF objective (NA 1.47 oil, Nikon Corp., Tokyo, Japan). Fluorescence signal was collected by an EM-CCD camera (Evolve 512, Photometrics) with frame rate of 12 frames per second. The raw images were processed by ImageJ and the Mosaic Particle Tracker plugin for ImageJ was used to perform background subtraction and deconvolution of the raw images.

Fluorescence Correlation Spectroscopy (FCS)

FCS measurements were performed on a customized Nikon Eclipse Ti inverted microscope. Briefly, a 561 nm laser beam was picked out by 561 nm \pm 20 nm dichroic mirror from a pulsed continuum white light laser (9.7 MHz, SuperK NKT Photonics). And the beam was focused on the sample through a 100X TIRF objective (oil, NA 1.49, Nikon). The laser beam was carefully placed at the nanoslit position. The emitted photons were collected through the same objective and directed a single photon avalanche diode (SPAD) detector (Micro Photon Devices). Photons collected by the detector were recorded with a time-correlated single photon counting (TCSPC) card (PicoHarp 300)

which was synchronized with the white light laser source. Five times of 30 second measurements were performed at the same spot of each nanoslit and were averaged in the correlation analysis. Correlation analysis was then performed on a computer with a custom-written Matlab script.

Preparation of Immobilized mAb Detector at Nanoplasmonic Gold Surfaces

The approach, combining a self-assembled monolayer (SAM) and a crosslink reaction, was used for the immobilization of a monoclonal antibody (mAb) of f-PSA.³⁵ The gold coated chips were first cleaned with O₂ plasma (South Bay Technologies PC2000 Plasma Cleaner) for 15 minutes. Then, the chips were processed overnight by a SAM using incubation in a mixture of 1 mM 11-mercaptodecanoic acid (HSC₁₀COOH, Aldrich) and 8-mercapto-octanol (HSC₈OH, Aldrich) in absolute ethanol solution with 1:2 mole ratio. After that, the SAM was activated by incubation in a 10 mM phosphate buffer solution (pH 7.0) with 0.5 mM of EDC/NHS for 2 hours. The activated SAM was rinsed with 10 mM PBS and immediately moved to a freshly prepared 10 mM PBS containing 10 µg/mL of the detector mAb for a subsequent 4 hours incubation. Then, the chip was rinsed with the PBS again and was dipped into a 0.2 M glycine PBS solution for 10 minutes in order to deactivate the remaining active sites at the SAM. The immobilized mAb was then ready for f-PSA binding.

Experimental Setup for Flow Control

A New Era pump system (NE-300) was used to control the flow rate to inject the sample solution to the microfluidic channel where the nanoledge array located in the

center of the channel. Figure 3.1 shows the device sketch and an image of actual device topped with a PDMS microfluidic channel and connection with the syringe pump for flow sample injection and flow rate control.

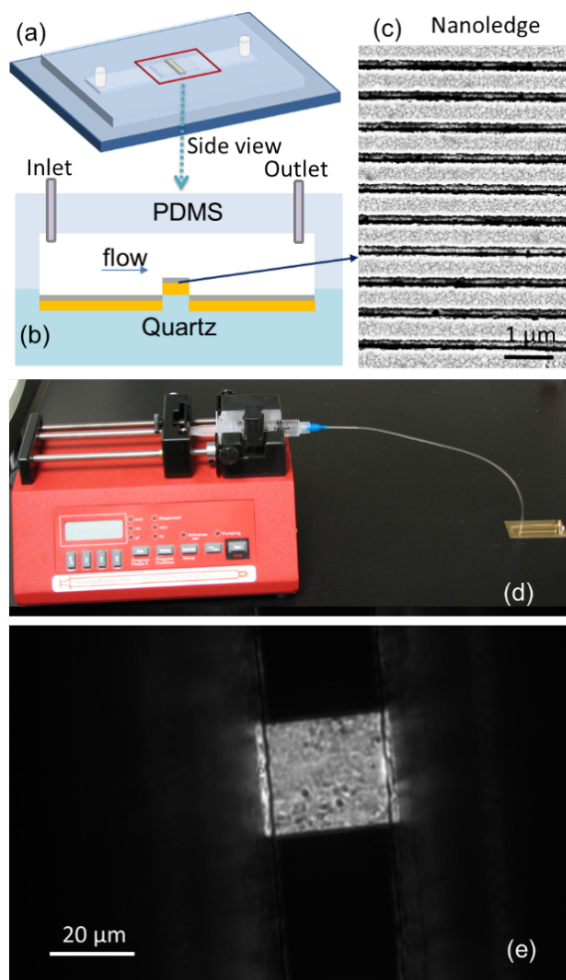


Figure 3.1. (a) Schematic Illustration of the Interface between the Nanoledge Array at the Quartz Chip and PDMS Microfluidic Channel, (b) Side View of the Micro-channel and, (c) a SEM Image of the Nanoledge Array. (d) Microfluidic Syringe Pump Connected to the PDMS Microfluidic Channel to Control the Flow Rates for Sample Delivery. (e) Bright Field Image of the Nanoledge Array Cross the “Dam” with a 60x Objective.

Results and Discussions

Two types of nanoledge structures, as shown in Figure 3.2a and 3.2b, were investigated. One nanoledge structure has an exposed gold surface and the other has a SiO₂ film (~10 nm thickness) coated atop the gold. The nanoledge array will allow for geometry induced nanoscale particle (e.g. proteins) trapping and plasmonic sensing using the metal film in the nanoledge cavity via T-SPR measurements. It is expected that the device, with the additional SiO₂ film, will allow for in-cavity detection with enhanced sensitivity.^{36,37} The in-plane nanoledge array platform is different from the well-recognized EOT nanohole flow-through pattern^{38,39} in which the sample flow direction is parallel to the incident light and normal to the chip plane. The nanoledge platform offers a solution-flow that is parallel to the chip plane and perpendicular to the incident light for plasmonic transmission in sensing applications. Hence, when used in clinical applications, like protein detection in whole blood or tissue lysates, it potentially provides a simple way to integrate with the microfluidic channels for nanometric-sized protein delivery to the nanoledge cavities, while larger particles (e.g. cells, or bio-fragments) simply flow over top of the nanoledge array. This allows for minimizing or avoiding the interference from non-specific bindings of cells or biofragments.

Semi-analytical Analysis of SP Generation and FDTD Simulation

Based on our recent fundamental work³² and the SP generation results of the open nanoledge structure, the optimal geometry of the plasmonic nanoledge slit has 280-300 nm open width and 50 nm bottom slit width. To develop the nanoledge structure for

investigating the trapping of molecules by the T-SPR measurement, we performed a proof-of-principle calculation of the SP generation at the flat interface of the nanoledge structures with and without the SiO₂ layer using a semi-analytical approach.^{32,40} A comparison of the semi-analytical decomposition analysis of SP generation efficiency, which is defined as the rate of surface plasmon polariton (SPP) launching, propagation and scattering by matching the continuous electromagnetic fields quantities at the interface,^{26,32} between the two different nanoledge structures are shown in Figure 3.2a, b. Predicted SP generation efficiencies e were calculated as functions of the nanoledge widths (top 280 nm and bottom 50 nm) and RIs ($n_1=1.41$, $n_2=n_3=$ bulk media RI, $n_4=$ stochastic RI) caused by a plane light wave ($\lambda=600$ nm) scattering at normal incidence to the nanoledge structure (details in SI). We found that when the RI of bulk media changed from 1.0 to 1.2, the absolute value of the total SP generation efficiency, $\Delta(e_1+e_2+e_3)$, decreased from 0.08 for the nanoledge structure with SiO₂ to the value of 0.06 for the nanoledge structure without SiO₂.

It has been found that the EOT peak shift, due to a weakened SP generation efficiency, correlates with a red shift of the optical transmission peak resulted from a coupling of dielectric changes with nanoledge geometry parameters.³² The in-gap surfaces of the nanoledge structure have a larger RI sensitivity than the top-of-gap surface mode; therefore the nanoledge structure with SiO₂ demonstrates higher sensitivity to the binding events when the molecule is trapped into the nanoledge gap. As the RI of the surrounding media is increased up to 1.5, this effect is further elucidated by an almost

three-fold decrease of the total SP generation efficiency. This value decreases from 0.16 to 0.06 for nanoledge structures with and without SiO₂ atop, respectively (Figure 3.2c, d).

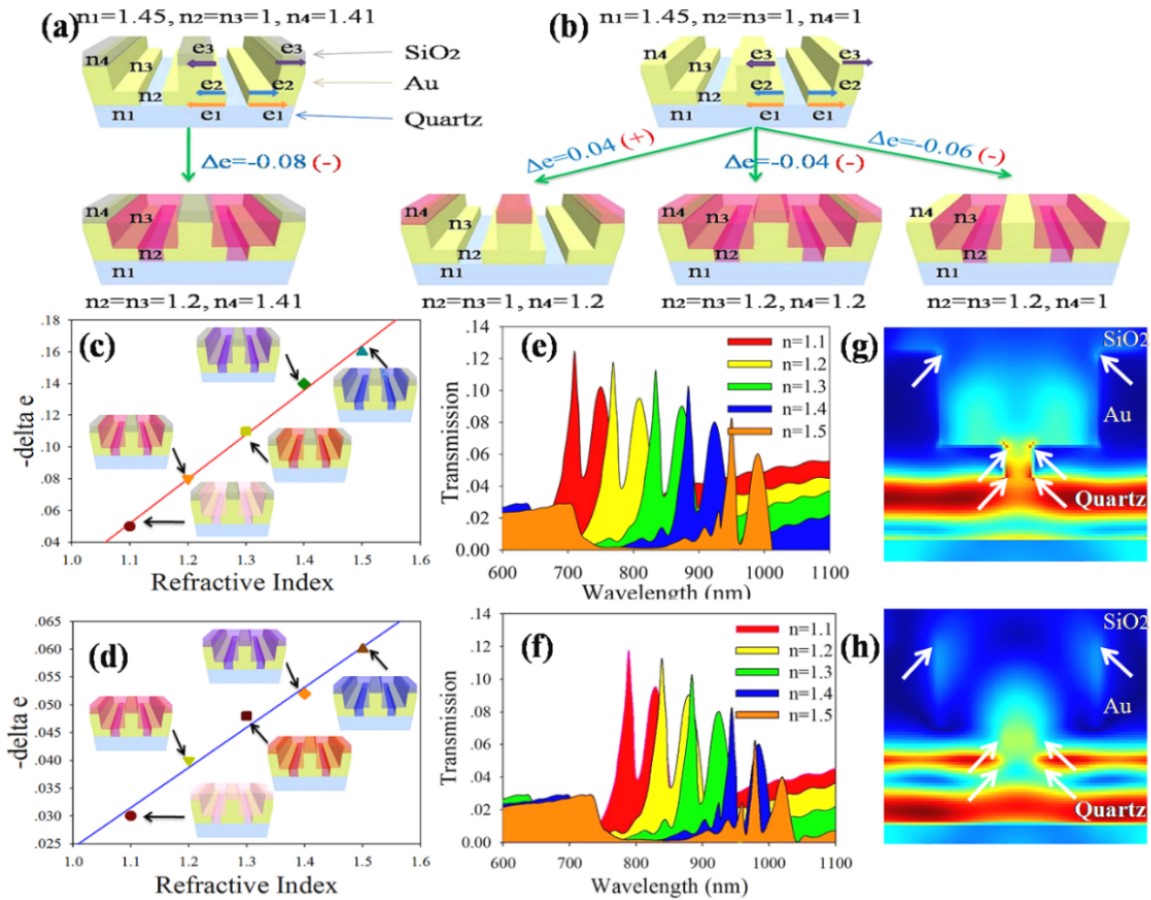


Figure 3.2. The SP Generation Efficiency Change, $\Delta(e_1+e_2+e_3)$, for the Nanoledge Geometry of 280-50 nm with on-top SiO₂ layer (a) and without on-top SiO₂ Layer (b) for the Bulk Media RI Ranging from 1.0 to 1.2. The SP Generation Efficiency for the Nanoledge with on-top SiO₂ layer (c) and without on-top SiO₂ layer (d) as the Surrounding Medium RI Increases from 1.1 to 1.5. The Calculated Transmission Spectra with on-top SiO₂ Layer (e) and without on-top SiO₂ Layer (f) as the Surrounding Medium RI Increases from 1.1 to 1.5. The TE Field Distribution (g) and TM Field Distribution (h) of the 280-50 nm Nanoledge with on-top SiO₂ Layer.

In concert with the semi-analytical analysis, Figure 3.2e-f summarizes the transmission spectra computed by a numerical 3D FDTD method for two selected nanoledges for RIs of a variety of surrounding medium from 1.1 to 1.5. Note that the setup of the FDTD method was similar to that of a previous study^{32,33} except the topped 10 nm SiO₂ surface layer. The peak wavelength shift of the nanoledge structure with SiO₂ (ca. 595 nm/RIU, Figure B1, Appendix B) was obtained and larger than that of the nanoledge structure without SiO₂ (ca. 556 nm/RIU³²).

We calculated the transverse electric (TE) and transverse magnetic (TM) modes for the nanoledge structure topped with SiO₂ (Figure 3.2g, h). Using a Drude dielectric function for bulk Au,^{33,41} we analyzed Au interfaces with quartz, air and SiO₂. It was found that the enhanced electromagnetic fields were located near in-gap surfaces for all three interfaces and those fields were higher in magnitude than in the nanoledge structure without SiO₂. This finding was further confirmed by computing the TE wave propagation through the simulation volume of 280-50 nm nanoledge system with SiO₂, as shown in Figure B2. The simulation results prove the higher SP generation, and enhanced sensitivity of the nanoledge structure topped with SiO₂ for detection of RI changes in the nanoledge gap area.

TIRF and FCS Studies of Protein Behavior

To study the diffusion of nanomolecules in the nanoledge structure, two kinds of nanoslit array chips were fabricated. These had slit widths of 100 nm or 300 nm and both had a period of 5.4 μm , as Figure B3. The 100 nm array can be located and observed with

reflection interference contrast microscopy (RICM) and transmitted light microscopy (TLM) (Figure 3.3 a, b). Since the size of the nanoslits is below the wavelength of visible light, diffracted features of the nanoslits were obtained. Once the nanoslits were located, a 561 nm laser was sent through the objective to allow TIRF imaging of the TxR-BSA molecules in the nanoslits. Note that the TIRF incident laser generates an evanescent excitation field, which decays exponentially from the substrate interface and penetrates to a depth of approximately 100 nm into the sample medium. Because the height of the nanoslits was 150 nm, the fluorescent signals picked up by TIRF imaging would be only due to the emission of fluorophores within the nanoslits (Figure 3.3 left panel). At first, the nanoslits appear to be totally non-fluorescent under TIRF imaging. Upon adding TxR-BSA to the medium, weak fluorescent signal was detected at the location of the nanoslits after 24 seconds (Figure 3.3c), indicating that TxR-BSA molecules entered the nanoslits. The fluorescent signal increased with longer observation time (Figure 3.3d, e) and finally reached a steady state. The TIRF imaging observation clearly demonstrates that TxR-BSA can diffuse into the 100 nm nanoslits. The gradual increase of the fluorescent signal suggests that the diffusion is driven by a concentration gradient and short-range energetic interactions at higher confinement grades.

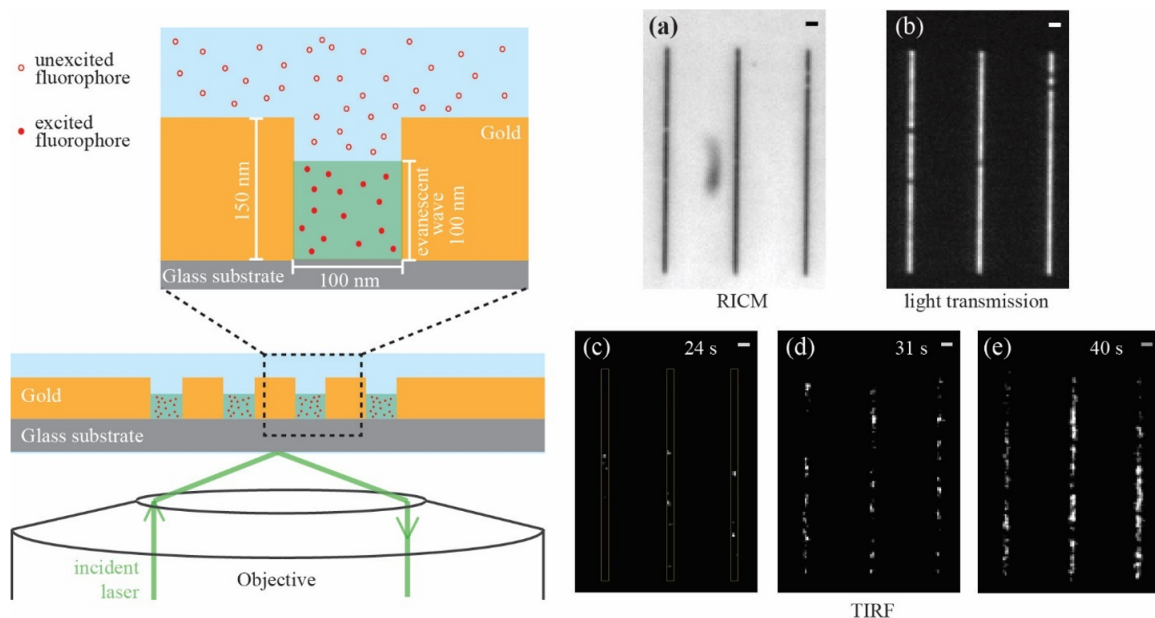


Figure 3.3. Left: Schematic Diagram of TIRF Imaging. TIRF Incident Laser Creates an Evanescent Wave That Only Excites Fluorophores within 100 nm Range from the Glass Substrate. With a Slit Depth of 150 nm, Only Those Fluorophores That Enter the Nanoslit Will be Excited and Observed. Right: (a) RICM and (b) TLM Image of 100 nm Nanoslits. (c-e) TIRF Images of TxR-BSA Diffusion into the Nanoslits at Time Points of 24 s, 31 s, and 40 s, Respectively. The Density and Intensity of Fluorescence Increase Along with Time, Indicating That TxR-BSA Molecule Can Diffuse into the Nanoslits. A Video Clip of the Process is Available in the SI. The Positions of Nanoslits Were Indicated by White Boxes. All Scale Bars are 1 μm .

The diffusion of TxR-BSA molecules was further studied by FCS (Figure 3.4a), which collects time-resolved fluorescence fluctuation caused by diffusion of fluorophores in and out of a confocal laser beam.⁴² The detection volume of the laser beam is diffraction limited, about 1.2 femtoliter, which makes FCS a single molecule sensitive method. The information of the diffusion of the molecules, which is concealed in the fluorescence fluctuation can be extracted by correlation:^{43,44}

$$G(\tau) = \langle \delta F(t + \tau) \delta F(t) \rangle / \langle F(t) \rangle^2 \quad (\text{Eq. 1})$$

where $\langle \rangle$ stands for a time average, $F(t)$ is fluorescence intensity at time t , and $\delta F(t) = F(t) - \langle F(t) \rangle$. The inflection point of the resulted auto-correlation function (ACF) curve represents the average dwell time (τ_D) of the diffusive molecule (Figure 3.4b). The τ_D of three-dimensional diffusion can be obtained by fitting the ACF curve with the three-dimensional diffusion model:

$$G(\tau) = G(0) / (1 + \tau/\tau_D) \sqrt{1 + [(\omega_0/z_0)]^2 \tau/\tau_D} \quad (\text{Eq. 2})$$

where ω_0 / z_0 is the ration of lateral and axial waist of the detection volume. The term ω_0 / z_0 is used to allow to float in the fitting process and only affects the fitting at the end of the decay. Uncertainty in ω_0/z_0 does not bias τ_D by more than a couple of percent. Once τ_D and ω_0 are calibrated, the diffusion coefficient (D , typically reported in $\mu\text{m}^2/\text{s}$) of the molecule can be calculated using

$$\tau_D = (\omega_0^2) / 4D \quad (\text{Eq. 3})$$

As illustrated in Figure 3.4a, the confocal laser beam was sent through the nanoslits to excite and detect fluorophores in the nanoslits. Since the size of the nanoslits is smaller than the diffraction limited laser beam, the actual detection volume is limited by the geometry of the nanoslits. A three-dimensional model is not perfectly fit for a slit structure to obtain the exact shape and size of the detection volume where the molecule is laterally confined, however, a standard method using a molecule with known diffusion

coefficient can be used to estimate the so-called effective detection volume. In order to quantify the lateral detection area, a standard dye molecule, fluorescein, with known D ($430 \mu\text{m}^2/\text{s}$) was used.⁴⁵ By measuring the average dwell time (τ_D) of fluorescein in the nanoslits, the effective detection area (A_{eff}) can be estimated using

$$\tau_D = A_{eff}/D \quad (\text{Eq. 4})$$

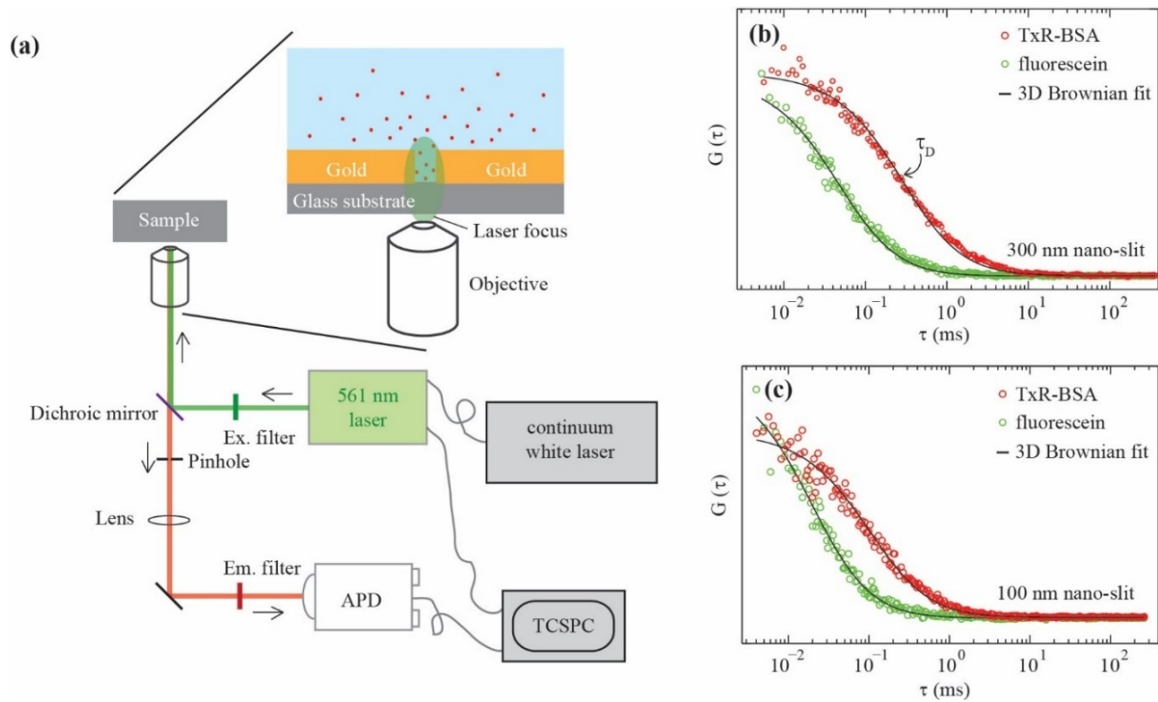


Figure 3.4. (a) Diagram of FCS Setup for Measuring Protein Diffusion in the Nanoslits. The Effective Detection Area, which is Defined by the size of the Nanoslits, is Smaller Than the diffraction Limited Confocal Detection Area (Laser Focus). Sample ACF curves of Fluorescein and TxR-BSA Diffusion in the 300 nm Nanoslits (b) and in the 100 nm Nanoslits (c). The Inflection Point of the ACF Curve Indicates the Average Dwell Time (τ_D) of Fluorescent Molecules within the Detection Volume.

The calibrated A_{eff} was then used for D calculation for BSA diffusion with the τ_D extracted from ACF curve. Figure 3.4b, c show examples of ACF curves of fluorescein motion in 300 nm and 100 nm nanoslits. The average dwell time (τ_D) of fluorescein in the 300 nm and 100 nm nanoslits is 0.052 ms and 0.028 ms, respectively. Based on the τ_D , the calculated A_{eff} for 300 nm and 100 nm nanoslits is $0.0224 \mu\text{m}^2$ and $0.0120 \mu\text{m}^2$. The data were summarized in Table 3.1.

Table 3.1
Results Obtained from FCS Measurements

	fluorescein τ_D (ms)	$A_{eff}(\mu\text{m}^2)$	TxR-BSA τ_D (ms)	TxR-BSA D ($\mu\text{m}^2/\text{s}$)
300 nm nanoslits	0.052±0.002	0.0224±0.001	0.320±0.006	69.9±1.3
100 nm nanoslits	0.028±0.006	0.0120±0.003	0.180±0.001	66.9±0.4

The diffusion of TxR-BSA was measured by FCS as well. As expected, the larger BSA molecule has a slower motion than the fluorescein molecule does. As shown in Figure 3.4b, c, the ACF curves of TxR-BSA motion shift towards the longer time domain. The τ_D extracted from the ACF curve is 0.320 ms and 0.180 ms for 300 nm and 100 nm nanoslits respectively, and the τ_D of TxR-BSA is one magnitude larger than that of fluorescein. Obviously, The D of TxR-BSA in 300 nm and 100 nm nano-slit are both around $70 \mu\text{m}^2/\text{s}$ (Table 3.1). Based on Stokes-Einstein equation:⁴⁶

$$D = kT / (6\pi r_h \eta), \quad (\text{Eq. 5})$$

where k is Boltzmann's constant, T is the temperature, r_h is the hydrodynamic radius, and η is the viscosity of the solvent. TxR-BSA molecules have a hydrodynamic radius of ~ 3 nm, which agrees with the reported size of BSA protein.⁴⁷ This result indicates that the diffusion of TxR-BSA within the two different sized nanoslits is Brownian motion with the same mobility. Combined with TIRF imaging results, the FCS measurements clearly demonstrate that TxR-BSA molecules can diffuse into the nanoslits via concentration gradient and short-range energetic interactions.

Protein f-PSA in Nanoledge Cavities and Sensing

Next, we performed a preliminary study to use the nanoledge structure for plasmonic sensing. We choose f-PSA biomarker for this performance due to its similar protein size with BSA. To detect such nanomolecule trapping experimentally, we employed a technique based on T-SPR spectrum measurements. A setup for flow-through nanoledge array, shown in Figure 3.1, was established to test the sample at the flow rate of $10 \mu\text{L}/\text{min}$. Note that the detection of T-SPR is under the condition of steady state of full-flow in the nanoledge slits. In this way, the nanoledge array was functioning as the nano-micro-fluidics that can direct sample delivery of analytes to the plasmonic sensing area by nanomolecule migration. The transmission spectra of the nanoledge array chip were measured in air and confirmed the SAM formation and mAb of f-PSA attachment to the nanoplasmonic sensing area in the gap.³⁵ Figure B4 displays the transmission spectra of the blank, alkanethiol SAM with carboxylic groups, and after mAb immobilization. The later peaks of the transmission were normalized to the maximum transmission of the

primary peak, as shown in Figure 3.5b. The primary peaks of the three spectra were located at 725.4 nm, 731.1 nm, and 746.5 nm for blank, SAM only, and SAM plus mAb, respectively.

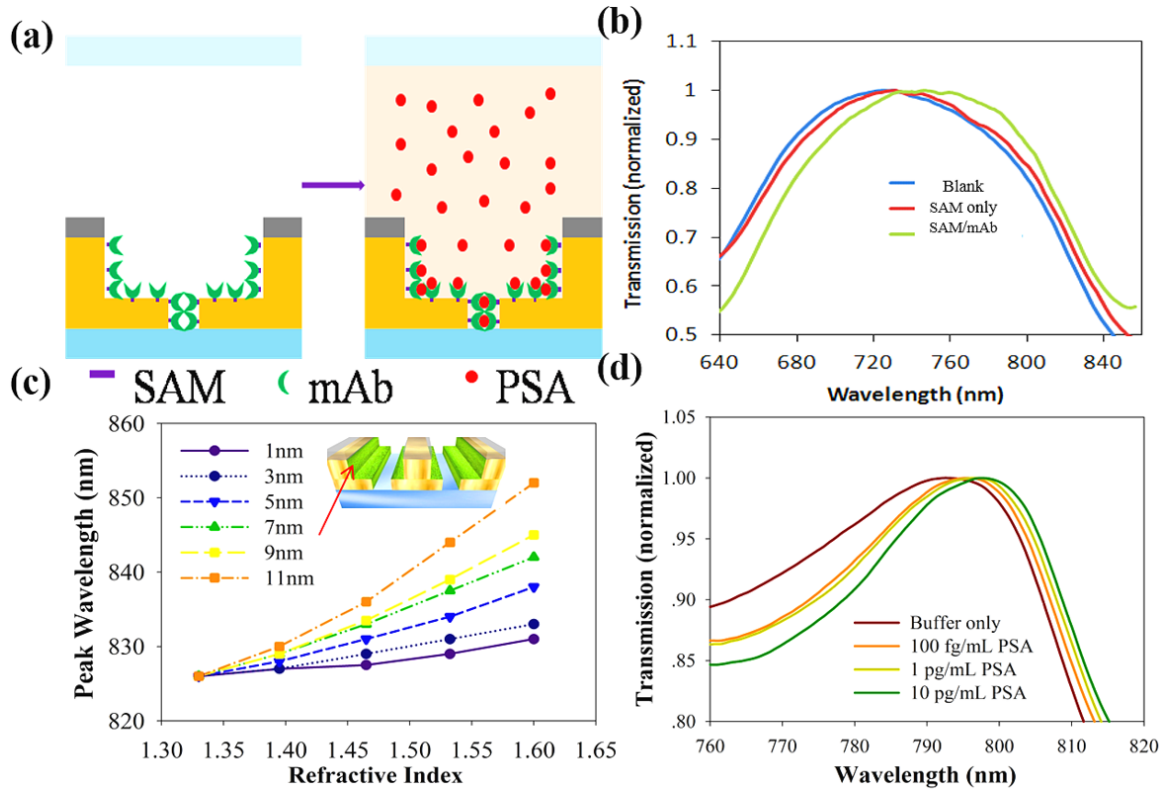


Figure 3.5. (a) An Illustration of the Immobilization of the Detection Antibody (mAb) at the SAM for f-PSA Binding. (b) Normalized Transmission Spectra of the Nanoledge Device at the Primary Peak. (c) FDTD Calculated Peak Wavelength for a Nanoledge Device in which the SAM was Located on the Walls within the Nanochannel for Varying Thickness Values of the SAM as the RI Index Varied from 1.33 (Water) to 1.6 (Protein SAM). (d) The Normalized Spectra of the Primary Peaks with Different Concentration of f-PSA in Buffer Solution.

The red shifts of the primary peak were 5.7 nm for SAM and 15.4 nm for mAb immobilization. Based on SPR sensing principle, it has been established to determine the

relationship between the peak wavelength and the thickness of added layer using the following equation:^{48,49}

$$\Delta\lambda = m(n_A - n_B) \left[1 - \exp(-2d_E/l_d) \right], \quad (\text{Eq. 6})$$

where $\Delta\lambda$ is defined as the peak wavelength shift after the addition of molecule layer to the precedent step modification, m is the RIU sensitivity, d_E is the effective thickness of the existing layer, l_d is the decay length of surface plasmon mode into the dielectric with 110 nm for the nanoledge dimension, and refractive indices of organic layer is taken to be 1.5 and that of air is 1.0.⁵⁰

Assuming the SAM is packed well at the surface with thickness of 1.1 nm, one is able to estimate the equivalent molecular thickness of mAb according to the following equation:

$$\frac{\Delta\lambda_{SAM}}{\Delta\lambda_{SAM+mAb}} = \frac{1 - \exp(-2d_{SAM}/l_d)}{1 - \exp(-2d_{SAM+mAb}/l_d)} \quad (\text{Eq. 7})$$

According to our measured average $\Delta\lambda$, the calculated equivalent thickness of mAb was found to be 1.9 nm. Moreover, the sensitivity was calculated as 576 nm/RIU, which agrees with the FDTD result above. To obtain a more realistic understanding of the device sensitivity to biological interactions through adsorption onto a SAM, a series of FDTD simulations were conducted in which the sidewall RI was changed while the background RI in the channel remained at 1.33. As we have seen from Figure 3.5c with

the nanoledge device, changing the thickness of organic layer on the sidewalls of the device resulted in marked red-shifts of peak wavelengths, since overall thickness of the organic layer increased, the magnitude of the RI increased as well.

In the end, we moved to the validation of f-PSA, with the same hydrodynamic radius of ~ 3 nm as BSA,⁵¹ trapping in the nanoledge gap and binding to the surface in the nanoledge cavities by measuring the peak wavelength shift using T-SPR sensing scheme. It was addressed by the transmission spectra of a series of f-PSA solutions of different concentrations, which were prepared for the f-PSA binding events at the SAM-mAb immobilized at the cavity gold surfaces, starting with incubation of buffer solution and increasing f-PSA concentration from 0.1 pg/mL to 10 pg/mL. Figure 3.5d shows the primary peak also has a red shift consistently within the concentration range of 0.1-10 pg/mL, which proves the trapping of f-PSA into the nanoledge structure array and plasmonic detection.

In this study, the nanoledge structure topped with SiO₂, which uses transmission SPR light signal transduction for sensing, provides a few advantages over traditional thin film SPR sensors that are based on total internal reflection of light with a prism. Specifically, the SiO₂-topped nanoledge offers a highly sensitive in-cavity detection mode,³⁷ and meanwhile avoid the nonspecific binding at the top surfaces. Even though the apparent bulk RI sensitivity (576 nm/RIU for the nanoledge) is smaller than that of traditional thin film SPR (usually thousands nm/RIU), the actual measurable sensitivity for affinity sensing is comparable or higher. This is because the evanescent field of LSPR

in the nanoledge has a much shorter decay and stronger near field enhancement than that of the propagating SPR along the thin film, greatly enhancing the sensitivity in detecting RI changes at the sensing vicinity of the metal/dielectric interface.⁵²⁻⁵⁴ In order to have strong SPR induced optical transmission for sensing, narrowed nanoslit (<100 nm) is necessary;³⁷ however it limits charged analytes (e.g. proteins) diffusion into the nanoslit due to the overlap of electric double layer effect in the nanochannel.^{55,56} The nanoledge structure, by combining narrow slit at the bottom and the wide open top, not only generates strongly coupled SPR induced optical transmission, but also overcomes the limit of small (<100 nm) nanochannels for migration of protein analytes into the channel, as shown in the results presented above. Moreover, it is expected that the SiO₂ topped nanoledge structure would not allow large biological species, e.g. cells, transporting into the ledge sensing area when it is used for protein detection from whole blood or serum samples. This research is underway and some preliminary results have been obtained.

Conclusions

In summary, we presented a new SiO₂ topped nanoledge aperture structure for nanometric-sized protein trapping and sensing. For the nanoledge structures, we applied the decomposition and quantitative analysis of SP generation by a semi-analytical model, and numerical simulation of optical transmission spectra and RI sensitivity by a FDTD method, which certificated that nanoledge structure with on-top SiO₂ layer had the potential to be effectively applied in T-SPR for protein detection. Experimentally, TIRF imaging showed that proteins can diffuse into the nanoledge structures (with 280 nm

open gap) by using similar size straight nanoslits (100 nm and 300 nm) to investigate the protein migration behavior. The diffusion of the labeled BSA into the nano-structure was measured by FCS with the results indicating that BSA molecules undergo Brownian motion and have a diffusion coefficient of approximately $70 \mu\text{m}^2/\text{s}$ in the nanoslit cavity, which agrees with its hydrodynamic radius of 3 nm. Further studies of the protein trapping and potential sensing applications were provided by fabricating a subwavelength nanoledge device and testing the SPR optical transmission shift and RI sensitivity for determining the binding events between the mAb and a cancer biomarker f-PSA in buffer solutions.

References

1. Krishnan, M.; Mojarad, N.; Kukura, P.; Sandoghdar, V. *Nature* **2010**, *467*, 692-695.
2. Zheng, B. Y.; Wang, Y.; Nordlander, P.; Halas, N. J. *Advanced Materials* **2014**, *26*, 6318-6323.
3. Cohen, A. E. *Physical Review Letters* **2005**, *94*, 118102.
4. Huang, L. R.; Cox, E. C.; Austin, R. H.; Sturm, J. C. *Science* **2004**, *304*, 987-990.
5. Singh, P. S.; Kätelhön, E.; Mathwig, K.; Wolfrum, B.; Lemay, S. G. *ACS Nano* **2012**, *6*, 9662-9671.
6. Cohen, A. E.; Moerner, W. E. *Proceedings of the National Academy of Sciences of the United States of America* **2006**, *103*, 4362-4365.
7. Krishnan, M.; Mönch, I.; Schwille, P. *Nano Letters* **2007**, *7*, 1270-1275.
8. Wenger, J.; Rigneault, H. *International Journal of Molecular Sciences* **2010**, *11*, 206-221.
9. Geissbuehler, M.; Bonacina, L.; Shcheslavskiy, V.; Bocchio, N. L.; Geissbuehler, S.; Leutenegger, M.; Märki, I.; Wolf, J.-P.; Lasser, T. *Nano Letters* **2012**, *12*, 1668-1672.
10. Foquet, M.; Korlach, J.; Zipfel, W. R.; Webb, W. W.; Craighead, H. G. *Analytical Chemistry* **2004**, *76*, 1618-1626.
11. Gérard, D.; Wenger, J.; Bonod, N.; Popov, E.; Rigneault, H.; Mahdavi, F.; Blair, S.; Dintinger, J.; Ebbesen, T. W. *Physical Review B* **2008**, *77*, 045413.
12. Mütze, J.; Ohrt, T.; Schwille, P. *Laser & Photonics Reviews* **2011**, *5*, 52-67.
13. Subba-Rao, V.; Hoffmann, P. M.; Mukhopadhyay, A. *Journal of Nanoparticle Research* **2011**, *13*, 6313-6319.
14. Kelly, C. V.; Wakefield, D. L.; Holowka, D. A.; Craighead, H. G.; Baird, B. A. *ACS Nano* **2014**, *8*, 7392-7404.

15. Nicoli, F.; Verschueren, D.; Klein, M.; Dekker, C.; Jonsson, M. P. *Nano Letters* **2014**, *14*, 6917-6925.
16. Chen, P.; Chung, M. T.; McHugh, W.; Nidetz, R.; Li, Y.; Fu, J.; Cornell, T. T.; Shanley, T. P.; Kurabayashi, K. *ACS Nano* **2015**, *9*, 4173-4181.
17. Lee, K.-L.; You, M.-L.; Tsai, C.-H.; Lin, E.-H.; Hsieh, S.-Y.; Ho, M.-H.; Hsu, J.-C.; Wei, P.-K. *Biosensors and Bioelectronics* **2016**, *75*, 88-95.
18. Lee, K.-L.; Chen, P.-W.; Wu, S.-H.; Huang, J.-B.; Yang, S.-Y.; Wei, P.-K. *ACS Nano* **2012**, *6*, 2931-2939.
19. Emam, A. N.; Mohamed, M. B.; Girgis, E.; Rao, K. V. *RSC Advances* **2015**, *5*, 34696-34703.
20. Cheng, Z.-Q.; Nan, F.; Yang, D.-J.; Zhong, Y.-T.; Ma, L.; Hao, Z.-H.; Zhou, L.; Wang, Q.-Q. *Nanoscale* **2015**, *7*, 1463-1470.
21. Baba, A.; Tada, K.; Janmanee, R.; Sriwichai, S.; Shinbo, K.; Kato, K.; Kaneko, F.; Phanichphant, S. *Advanced Functional Materials* **2012**, *22*, 4383-4388.
22. Malic, L.; Morton, K.; Clime, L.; Veres, T. *Lab on a Chip* **2013**, *13*, 798-810.
23. Wang, P.; Zhang, L.; Xia, Y.; Tong, L.; Xu, X.; Ying, Y. *Nano Letters* **2012**, *12*, 3145-3150.
24. Hill, R. T.; Kozek, K. M.; Hucknall, A.; Smith, D. R.; Chilkoti, A. *ACS Photonics* **2014**, *1*, 974-984.
25. Knoll, W. *Annual Review of Physical Chemistry* **1998**, *49*, 569-638.
26. Lalanne, P.; Hugonin, J. P.; Rodier, J. C. *Physical Review Letters* **2005**, *95*, 263902.
27. Kress, S. J. P.; Richner, P.; Jayanti, S. V.; Galliker, P.; Kim, D. K.; Poulikakos, D.; Norris, D. J. *Nano Letters* **2014**, *14*, 5827-5833.
28. Cetin, A. E.; Etezadi, D.; Galarreta, B. C.; Busson, M. P.; Eksioglu, Y.; Altug, H. *ACS Photonics* **2015**, *2*, 1167-1174.
29. Gordon, R.; Sinton, D.; Kavanagh, K. L.; Brolo, A. G. *Accounts of Chemical Research* **2008**, *41*, 1049-1057.
30. Melikyan, A.; Alloatti, L.; Muslija, A.; Hillerkuss, D.; Schindler, P. C.; Li, J.; Palmer, R.; Korn, D.; Muehlbrandt, S.; Van Thourhout, D.; Chen, B.; Dinu, R.;

- Sommer, M.; Koos, C.; Kohl, M.; Freude, W.; Leuthold, J. *Nat Photon* **2014**, *8*, 229-233.
31. Reiner, J. E.; Robertson, J. W. F.; Burden, D. L.; Burden, L. K.; Balijepalli, A.; Kasianowicz, J. J. *Journal of the American Chemical Society* **2013**, *135*, 3087-3094.
 32. Zeng, Z.; Mendis, M. N.; Waldeck, D. H.; Wei, J. *RSC Advances* **2016**, *6*, 17196-17203.
 33. Zeng, Z.; Liu, Y.; Wei, J. *TrAC Trends in Analytical Chemistry* **2016**, *75*, 162-173.
 34. Wei, J.; Rexius, M.; Kofke, M.; Wang, Y.; Singhal, S.; Waldeck, D. H. *Nanotechnology* **2011**, *3*, 79-82.
 35. Sanders, M.; Lin, Y.; Wei, J.; Bono, T.; Lindquist, R. G. *Biosensors and Bioelectronics* **2014**, *61*, 95-101.
 36. Eftekhari, F.; Escobedo, C.; Ferreira, J.; Duan, X.; Girotto, E. M.; Brolo, A. G.; Gordon, R.; Sinton, D. *Analytical Chemistry* **2009**, *81*, 4308-4311.
 37. Lee, K.-L.; Wang, W.-S.; Wei, P.-K. *Biosensors and Bioelectronics* **2008**, *24*, 210-215.
 38. Gordon, R.; Brolo, A. G.; McKinnon, A.; Rajora, A.; Leathem, B.; Kavanagh, K. L. *Physical Review Letters* **2004**, *92*, 037401.
 39. Escobedo, C.; Brolo, A. G.; Gordon, R.; Sinton, D. *Analytical Chemistry* **2010**, *82*, 10015-10020.
 40. Lalanne, P.; Hugonin, J. P.; Rodier, J. C. *J. Opt. Soc. Am. A* **2006**, *23*, 1608-1615.
 41. Vial, A.; Laroche, T. *Applied Physics B* **2008**, *93*, 139-143.
 42. Aouani, H.; Wenger, J.; Gérard, D.; Rigneault, H.; Devaux, E.; Ebbesen, T. W.; Mahdavi, F.; Xu, T.; Blair, S. *ACS Nano* **2009**, *3*, 2043-2048.
 43. Shi, X.; Li, X.; Kaliszewski, M. J.; Zhuang, X.; Smith, A. W. *Langmuir* **2015**, *31*, 1784-1791.
 44. Shi, X.; Kohram, M.; Zhuang, X.; Smith, A. W. *Langmuir* **2016**, *32*, 1732-1741.
 45. Petrášek, Z.; Schwille, P. *Biophysical Journal* **2008**, *94*, 1437-1448.
 46. De Santo, I.; Causa, F.; Netti, P. A. *Analytical Chemistry* **2010**, *82*, 997-1005.

47. González Flecha, F. L.; Levi, V. *Biochemistry and Molecular Biology Education* **2003**, *31*, 319-322.
48. Jung, L. S.; Campbell, C. T.; Chinowsky, T. M.; Mar, M. N.; Yee, S. S. *Langmuir* **1998**, *14*, 5636-5648.
49. Haemers, S.; Koper, G. J. M.; van der Leeden, M. C.; Frens, G. *Langmuir* **2002**, *18*, 2069-2074.
50. Chen, S.; Svedendahl, M.; Käll, M.; Gunnarsson, L.; Dmitriev, A. *Nanotechnology* **2009**, *20*, 434015.
51. Mulder, S. D.; Heijst, J. A.; Mulder, C.; Martens, F.; Hack, C. E.; Scheltens, P.; Blankenstein, M. A.; Veerhuis, R. *Annals of Clinical Biochemistry* **2009**, *46*, 477-483.
52. Yonzon, C. R.; Jeoung, E.; Zou, S.; Schatz, G. C.; Mrksich, M.; Van Duyne, R. P. *Journal of the American Chemical Society* **2004**, *126*, 12669-12676.
53. Haes, A.; Duyne, R. *Analytical and Bioanalytical Chemistry* **2004**, *379*, 920-930.
54. Lee, K.-L.; Chang, C.-C.; You, M.-L.; Pan, M.-Y.; Wei, P.-K. *Scientific Reports* **2016**, *6*, 33126.
55. Pennathur, S.; Santiago, J. G. *Analytical Chemistry* **2005**, *77*, 6772-6781.
56. Karnik, R.; Fan, R.; Yue, M.; Li, D.; Yang, P.; Majumdar, A. *Nano Letters* **2005**, *5*, 943-948.

CHAPTER IV

MICROFABRICATION OF A FLOW-OVER FLUIDIC DAM

Overview

A flow-over type dam is needed in fluidic channels for a variety of reasons. Those reasons include: forcing analytes to move towards an area of interest (a detection area) within a flow channel, to decrease diffusion times of analytes, and not clogging like flow-through systems have the potential to do. This chapter will serve as a technical chapter on the microfabrication of a flow-over fluidic dam. Standard photolithography, etching, and multi-layered resist will be addressed. The use of long pass wavelength filter to reduce T topping in SU-8 microstructures is also examined. Additionally, the close of the chapter will take readers through the microfabrication techniques that were attempted.

Introduction

Microfabrication processes used in the semiconductor industry have become widely used for the fabrication of biosensing devices. These devices often are made up of micro- and nanostructures. The ability to fabricate these small structures with complete control is paramount in making a functioning device. Having tunability of the spatial dimensions, spacing (pitch) between each structure, any curvature, and sidewall angles of a microstructure is needed to overcome problems that arise when devices are used for real-world biosensing, such as with whole blood samples. The “Holy Grail” for

biosensing devices would be the use of whole blood sample without any previous sample pretreatment. Scientists have tried to use whole blood in biosensors without much avail. The major issue lies in the “stickiness” of red blood cells, which leads to non-specific binding. Another issue is their large size compared to the protein biomolecules of interest. The large size provides a problem when researchers design and use flow-through systems which have the potential to clog. One concept is to perform in-line or on-chip separation of the blood cells from the protein biomarkers. A fluidic dam is one such mechanism. This chapter is a technical chapter and centers around the microfabrication approach to building a fluidic dam microstructure that is suitable for delivering proteins to the sensing area while excluding particles several microns in size. The devices, structures, and fluidic dams discussed are all in relation to a plasmonic biosensor.

Flow-over vs. Flow-through Sensing

A flow-through fluidic system is one in which the analytes are forced to flow through porous structures. In a plasmonic sensor that uses nanostructures for surface plasmon polariton coupling, not only are the nanostructures used for surface plasmon resonance (SPR), they are also used for conduits for fluid flow. A flow-through type system is shown in Figure 4.1. In a fluidic flow channel not all of the analytes in the sample diffuse to the surface. This is especially true when the channel height is the micrometers or millimeter range. Compared to the size of a typical 3 nm protein, a flow channel of 200 μm is extremely large. In such a channel, the protein or biomarker of interest has a long way to diffuse to the surface. It helps to put these numbers in

perspective; the distance from Washington DC to Philadelphia, PA is 126 miles. This distance, compared to a 6-foot tall man, is the same size correlation for the channel height to protein. This is a very long way for a protein to diffuse to the detection area. Flow-through sensing (Figure 4.1) utilizes nanoholes for sensing, but also as channels for fluid flow.^{1,2} This removes the diffusion bottleneck found with traditional fluidic sensors. With the flow-through setup, the analytes are forced through the metal surface, shortening the diffusion time. This can afford an order of magnitude increase in sensing rate. The surface ligand can also capture more analyte in a flow-through arrangement. The benefits of flow-through sensing are the following: the diffusion times become short, the K_a increases by a factor of 6 (Figure 4.1C), the sensitivity is increased as analytes go through the holes where there is maximum EM field confinement, and the limit of detection for the flow-through device is improved.^{2,3}

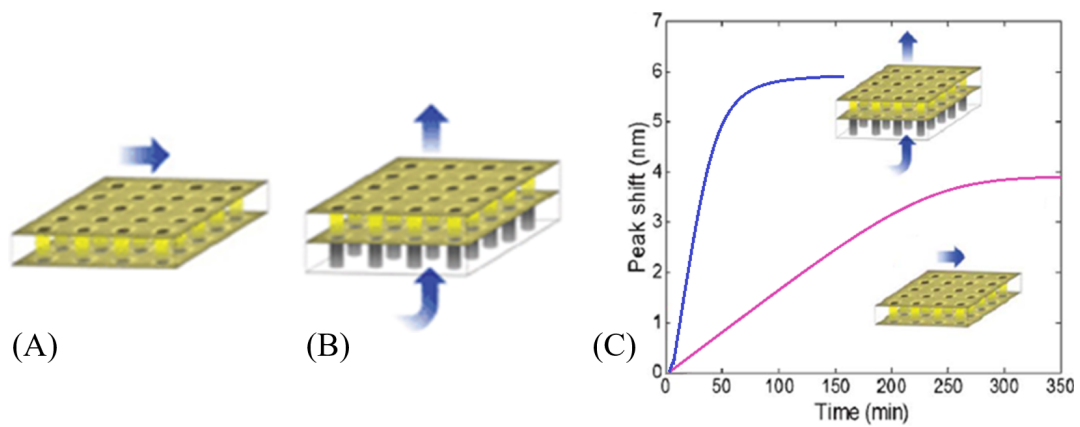


Figure 4.1. (A) Flow-over vs. (B) Flow-through Sensing with Red Balls Representing Analytes. (C) The Graph Shows the Peak Shift Per Unit Time. The K_a (Rate Constant) for the Flow-through is 6 Times Greater Than That of the Flow-over.²

Flow-through sensing requires several additional microfabrication steps in order to use nanostructures for their plasmonic ability and for conduits for fluid flow. When applying this type of system to a real-world sample, like whole blood, a major issue arises—large red blood cells several microns in size cannot pass through the nano-dimensioned structures, which causes clogging.

Analytes that typically would not bind in a standard flow channel do bind in a flow-through system because they are forced to flow within a few nanometers from the bound surface ligand in the flow-through setup. This makes binding a more likely event with the flow-through setup. Taking advantage of the flow-through system while avoiding the clogging issue would be a great advantage for plasmonic sensors that wish to use real-world samples without sample pretreatment. This can be accomplished by narrowing the channel in a flow-over system.

A flow-over system could show the benefits of the flow-through system by simply narrowing the flow channel by making a fluidic dam microstructure. Figure 4.2A presents a standard flow channel in cross section. Figure 4.2B shows a linear flow channel with raised isle, which we call a flow-over fluidic dam. Narrowing the top to bottom distance of the flow channel constricts the flow. This effect along with a laminar flow friction differential results in a net downward force on the particle, driving the analyte into the slit cavity. These factors along with diffusion, Brownian motion, and k_{on} and k_{off} of the analyte/ligand pair should afford sufficient force to drive the analytes to the slits.

A flow-over fluidic system with a nanostructured plasmonic detection platform (Figure 4.2B) is presented here. The flow-over fluidic dam needs to be made of a transparent material because it is intended for use in an optical system. Forming the flow-over dam out of patterning a glass substrate or by SU-8 photoresist is considered below.

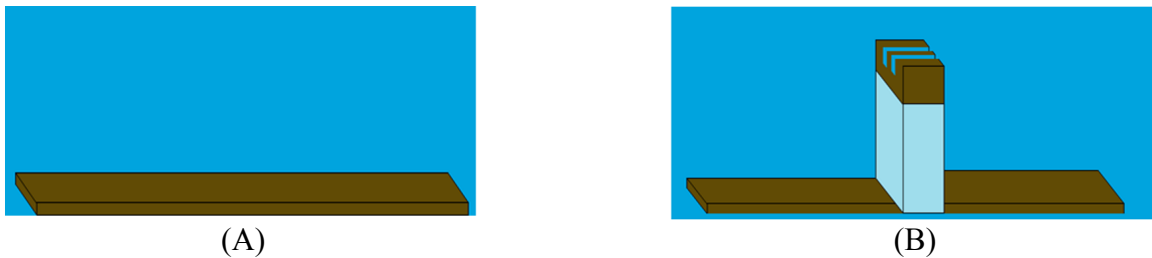


Figure 4.2. (A) Standard Gold Surface and Flow Channel. (B) Gold Surface with Linear Flow Channel Showing a Flow-over Dam (Raised Isle) with Gold Nanoslit Array.

Flow-over Dam Design

A schematic of a substrate with a single flow-over dam is shown in Figure 4.3. The insert shows a magnified view of the dam. The flow channel (shown in blue) is composed of either soda lime glass or quartz, while the top portion (shown in green) is the enclosed flow chamber made out of polyethylene. The fluidic dam has a gold film evaporated on top of the flow-over dam. The gold film is then nanostructured with a reference window and an array of nanostructures.

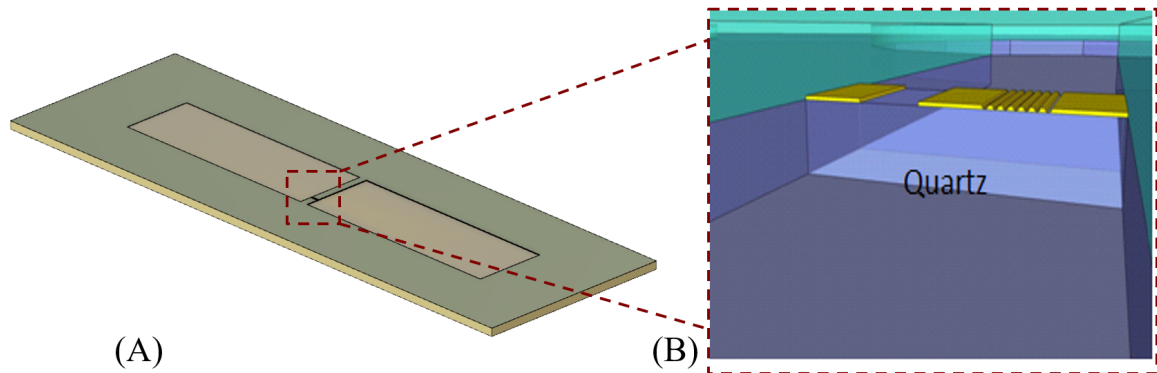


Figure 4.3. (A) Schematic of Chip with a Magnification on the Fluidic Dam. (B) a Cross section Schematic Showing a Flow-over Fluidic Dam with a Gold Thin Film on Top. A Reference Window and an Array of Nanostructures are Shown Milled into the Gold Thin Film.

A logical way to make a microstructure, such as a fluidic dam, is with lithography and etching. Figure 4.4 shows this sequence. A computer-aided design (CAD) software is used to make several designs (Figure 4.4A). One of more of these patterns are transferred to a quartz and chrome substrate or simply printed on a transparency film to generate a photomask. A substrate such as a glass wafer is cleaned and dehydrated (Figure 4.4B). Photoresist is spin applied to this cleaned substrate (Figure 4.4C). The photomask with the design of choice is then transferred onto the photoresist covered substrate via lithography (Figure 4.4D). The device is then etched to afford a three-dimensional structure into the glass substrate (Figure 4.4E). In order for the device to have plasmonic capability it needs a thin film of metal, such as gold. Considering the primary focus of this dissertation is in regards to plasmonic devices, we will continue with metal deposition here. The device is then covered with metal by evaporation (Figure 4.4F). The final step before nanostructuring the substrate would be oxide deposition. As previously

mentioned, the nanostructured oxide layer provides small proteins entry into the sensing area while excluding larger molecules.

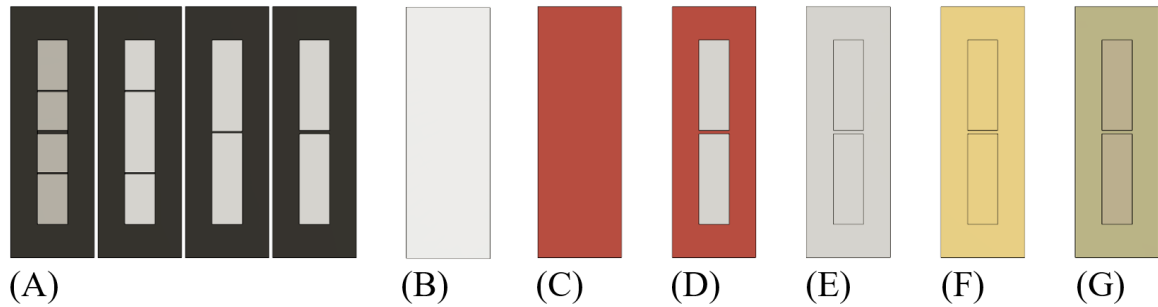


Figure 4.4. Fabrication Process Overview for a Fluidic Dam: (A) Mask Designed in CAD Software, (B) Glass Substrate Cleaned and Dehydrated, (C) Spin Apply Photoresist, (D) Lithography, (E) Etching, (F) Metal Deposition, and (G) Oxide Deposition.

Flow-over Dam Sidewall Profiles

The use of nanostructured thin metal films for surface plasmon polariton (SPP) coupling, as opposed to a prism, has a benefit of a linear, transmission arrangement (see introductory chapter). This linear alignment simplifies the optics and allows for use in point-of-care systems. In transmission surface plasmon resonance (tSPR) light is passed through nanostructures. When planar metal films are used, the majority of the film is largely opaque due to the metal coating. Metals films approximately 50 nm to 300 nm in thickness are then nanostructured. The addition of a fluidic dam to the tSPR system provides a hurdle that must be overcome—light escaping from the sidewalls of the fluidic dam. This is due to the sidewall angle of the fluidic dam structure.

The sidewalls of a microstructure made with lithography typically take on one of four shapes: straight 90° sidewalls, undercut trapezoid, T topped, or overcut trapezoid. These are shown in Figure 4.5, in cross-section.



Figure 4.5. Cross Section Sidewall Profiles in Patterned Photoresist Include (A) Straight Sidewalls, (B) Undercut Trapezoid, (C) T Topped Profile, and (D) Overcut Trapezoid.

The first three sidewall profiles (straight, undercut, and T topped) all have an issue in regards to tSPR. The issue for these shapes lies in their use in optical devices in transmission mode. In a transmission arrangement, light escapes from the sidewalls because the sidewalls would not be coated with metal during the evaporation of gold. Figure 4.6 shows a glass substrate with two fluidic dam structures with undercut sidewalls. The figure clearly shows that after metal deposition, there would be metal on the top of the dams, but there would be no metal on the sidewalls. This is because gold deposition by evaporation is a line-of-sight deposition technique. For the straight sidewalls and T topped sidewalls this also applies.

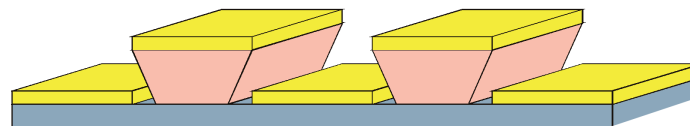


Figure 4.6. Glass Substrate with Two Fluidic Dams with Undercut Sidewalls. The Sidewalls Are Not Coated with Gold during Evaporation.

Nanostructures are milled into the top of the fluidic dam. Their function is to couple light into a surface plasmon. This plasmonic effect is diminished if the majority of the light escapes from the sidewalls of the fluidic dam. This is shown in Figure 4.7. When a light source is placed underneath a substrate that is transparent due to lack of metal on the sidewalls there is an issue. For an undercut, T topped, or straight sidewall profile this is the case.

The undercut shape was realized when using proximity printing. In proximity printing an exposure gap is placed between the photomask and the resist covered substrate. Doing so has the benefit of preserving the lifetime of the photomask and not pressing on the pristine photoresist surface. The T topped shape was realized when the exposure of the photoresist was performed in contact mode. In contact mode the photomask and the resist covered substrate come into contact. This significantly cuts down on the light diffraction through the photomask apertures. However, contact exposure yields a T topping effect (more on how to resolve this later in this chapter). Achieving the desired overcut profile with SU-8 was not achieved using as simple, single layer lithography. The methods that were considered to achieve an overcut profile were gray scale lithography and a multi-layered resist (MLR) method. MLR is discussed in the following experimental section.

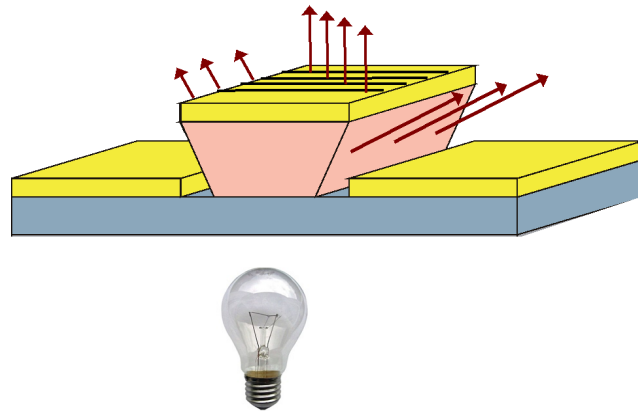


Figure 4.7. An Undercut Sidewall Made of Transparent Photoresist Will Be Transparent to Light When a Light Source is Placed Underneath the Substrate. With No Metal Coverage the Sidewalls Light Not Only Comes through the Intended Nanostructures, But It Also Escapes out of the Sidewalls, Dramatically Affecting the SPR Signal.

Materials and Methods

Optical Transmission Microscopy

Substrates with fluidic dams were set up in an Olympus BX41 microscope. An external light source (Ocean Optics, LS-1) was used to illuminate the underside of the substrate. Images were captured in reflection mode and in transmission mode. As shown in Figure 4.8A, the reflection image shows a fluidic dam structure covered in gold except for a reference window measuring $75\ \mu\text{m} \times 25\ \mu\text{m}$. In this area the gold was removed by focused ion beam milling, leaving a transparent window. The transmission image (Figure 4.8B) shows the external light source illuminating and exiting the reference window. Moreover, one can see the light escaping from the sidewalls of the fluidic dam structure. This is due to an undercut sidewall profile not being covered with metal during metal deposition.

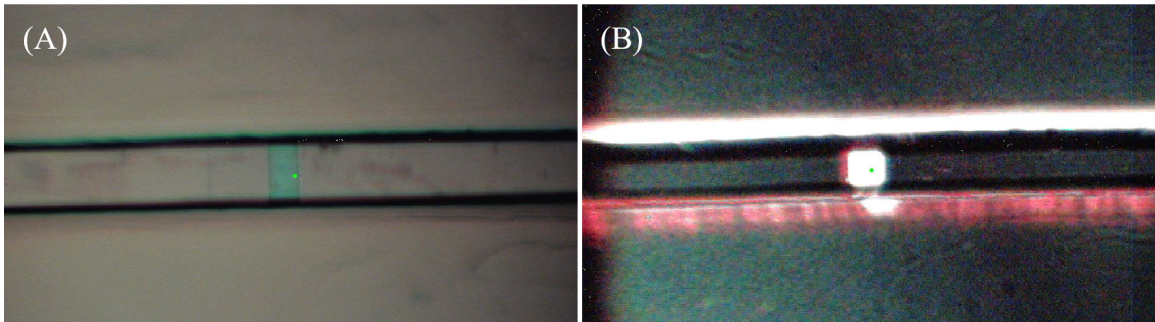


Figure 4.8. (A) Reflection Image of a Fluidic Dam with a $75\ \mu\text{m} \times 25\ \mu\text{m}$ Reference Box Milled into the Dam. (B) Transmission Image of a Fluidic Dam with Light Exiting the $75\ \mu\text{m} \times 25\ \mu\text{m}$ Box. Additionally, One Can See the Light Escaping from the Sidewalls. This is Due to an Undercut Sidewall Profile Not Being Covered with Metal during Metal Deposition.

Fluidic dams with an undercut profile, T topped profile, and an overcut sidewall profiles were investigated for light escaping from the sidewalls during transmission microscopy. Figure 4.9A shows a reflection microscope image of a $50\ \mu\text{m}$ flow-over dam. The dam is located $7\ \mu\text{m}$ above the base of the flow channel floor. In Figure 4.9B, a transmission image is captured for a fluid dam with undercut sidewalls with 122.9 degrees. Light is seen being transmitted through the transparent sidewalls. Figure 4.9C, shows a T topped sidewall. This T topped shaped was achieved by contact exposure of the photoresist. This afforded a microstructure with sidewalls with much less slope than the undercut dam (103.2° as opposed to 122.9° sidewalls). The transmission image still shows light escaping from the sidewalls. Figure 4.9D shows the flow-over dam without nanostructures with the light source on. This optical image is completely dark because the overcut sidewalls are opaque due to their $4\ \text{nm}$ titanium and $250\ \text{nm}$ gold coating. Figure 4.9E shows a reflection image of a flow-over dam with an array of milled nanostructures.

The nanostructures were milled so that they completely spanned the width of the fluidic dam. A transmission image of a fluidic dam with undercut sidewalls is seen in Figure 4.9F.

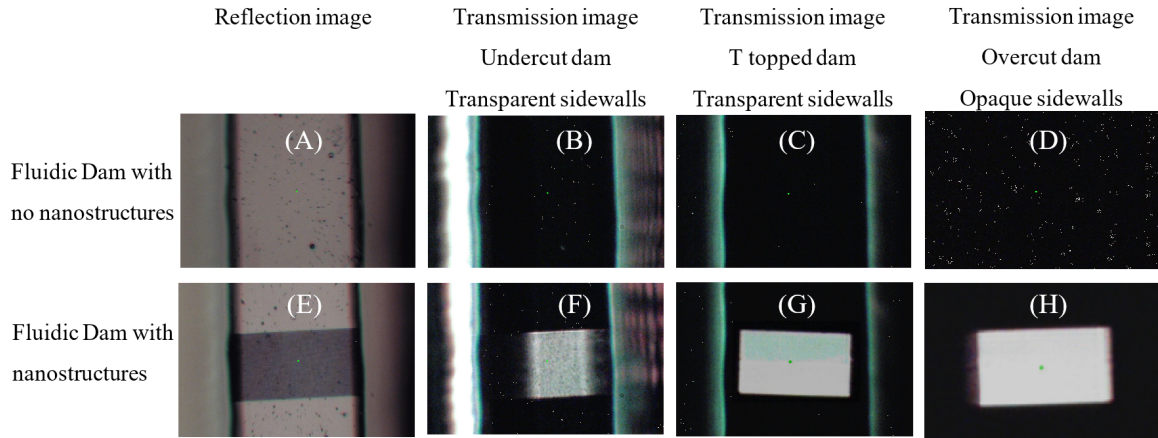


Figure 4.9. (A) Reflection Microscope Image of a Fluidic Dam without Nanostructures Milled into the Dam. Transmission Microscope Images Showing (B) Light Escaping from the Transparent Sidewalls of an Undercut Dam, (C) Light Escaping from the Transparent Sidewalls of a T Topped Dam, and (D) Opaque Sidewalls of an Overcut Dam. (E) Reflection Microscope Image of a Fluidic Dam with a Milled Nanostructure Array Measuring $25\ \mu\text{m} \times 50\ \mu\text{m}$. Transmission Microscope Images Showing (F) the Majority of Light Escaping through the Sidewall as Opposed to the Milled Nanostructures in an Undercut Dam, (G) a Portion of the Light Escaping the Sidewalls of a T Topped Dam, and (H) All of the Light Passing through the Milled Nanostructures in an Overcut Dam.

Similar to the case in Figure 4.9B, light is seen escaping from the sidewalls, which lack a metal coating. It should be noted that the nanostructures were milled the span the width of the fluidic dam. It looks as if the nanostructured array is smaller than the array in Figure 4.9E. This is not the case. The light escaping from the sidewalls affects the amount of light that passes through the nanostructured array. Figure 4.9G

shows the case where a fluid dam has an array of nanostructures milled into the top of the dam. The majority of the light passes through the nanostructures, but there is some light bleed from the sidewalls. Figure 4.9H shows the case of nanostructures milled into a fluidic dam with an overcut sidewall profile. Akin to Figure 4.9D, no light is visible through the sidewalls. All of the light passes through the nanostructured array.

Figure 4.9E shows a reflection image of a flow-over dam with an array of milled nanostructures. The nanostructures were milled so that they completely spanned the width of the fluidic dam. A transmission image of a fluidic dam with undercut sidewalls is seen in Figure 4.9F. Similar to the case in Figure 4.9B, light is seen escaping from the sidewalls, which lack a metal coating. It should be noted that the nanostructures were milled the span the width of the fluidic dam. It looks as if the nanostructured array is smaller than the array in Figure 4.9E. This is not the case. The light escaping from the sidewalls affects the amount of light that passes through the nanostructured array. Figure 4.9G shows the case where a fluid dam has an array of nanostructures milled into the top of the dam. The majority of the light passes through the nanostructures, but there is some light bleed from the sidewalls. Figure 4.9H shows the case of nanostructures milled into a fluidic dam with an overcut sidewall profile. Akin to Figure 4.9D, no light is visible through the sidewalls. All of the light passes through the nanostructured array.

T Topping

To create a fluidic dam that has a depth on the order of several micrometers, the exposure method (proximity vs. contact mode) and exposure wavelengths became

critical. Thick layers (more than a few microns) of SU-8 photoresist show unusual effects when wavelengths 365 nm and shorter are used for exposing the photoresist. An OAI 8008 mask aligner with a 1000-watt DUV-1000 Xenon Hg Arc lamp from Advanced Radiation Corporation was used for the exposure. Spectral lines of 436 (g-line), 405 (h-line), 365 (i-line), and 248 nm were generated. The issue of exposing SU-8 with shorter wavelength is that an effect, known as T topping, becomes evident. T topping is well documented and is when a microstructure takes on a T shape in cross section (Figure 4.5C).¹⁰⁻¹⁷ Yang and Wang best described T topping when they stated the following:

As the light beam penetrates the SU-8 resist layer from the top to the bottom, the light intensity drops gradually as the light is absorbed. As the result, the top part of SU-8 resist absorbs higher dosage than that at the bottom part, and frequently leads to over-dosage at the top and under-dosage at the bottom. This is one of the major reasons that inexperienced operator often produces mushroom types of microstructures in UV-lithography of SU-8.⁹

T topping of an SU-8 structure is shown in the SEM image in Figure 4.10. The cross-section image of the SU-8 structure shown in Figure 4.10 was created using contact exposure with a Xenon Hg Arc lamp without any wavelength filtering. The resultant T topping is evident.

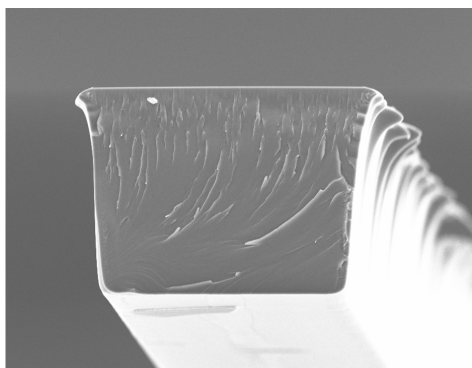


Figure 4.10. SEM Cross-section Image Showing a T Topped Photoresist. When Wavelengths Equal to 365 nm and Below Were Used to Expose SU-8 a T Topping Effect was Observed.

In the experiments reported in this dissertation, the Xenon Hg Arc lamp was used without a filter and with various filters in order to reduce the T topping effect found in SU-8 lithography. Wavelength filters, such as glass or PMMA, have been used in the past.⁹ We attempted to use several wavelength filters as long-pass filters in order to remove the wavelengths of 365 nm and shorter during the exposure of SU-8. Pieces of substrate that measured between 2 and 4 mm in thickness were investigated for their ability to filter out wavelengths 365 nm and shorter. A Varian Cary 6000i UV-Vis Spectrophotometer was used to investigate each substrate's ability to act as an optical filter and reduce T topping. The optical transmission spectrum of each filter is shown in Figure 4.11. Polystyrene did not start significantly attenuating the transmission until 290 nm and gave approximately 70% transmission at 365 nm. Soda lime glass showed 80% transmission at 365 nm. A filtering device purchased from Omega Filters (PL-360LP) was investigated showed 50% transmission at 365 nm. Acrylic and UV acrylic sheets

completely removed the majority of transmitted light at 365 nm. Polycarbonate showed a 27% transmission to the h-line (405 nm) and completely attenuated the i-line. Cross-linked SU-8 was also investigated as a potential long pass filter. SU-8 showed 21% transmission at 405 nm and 1% transmission at 365 nm. The Omega filter and the UV acrylic filter were the two filters of high interest after the results from the optical transmission test. The Omega filter allowed in some light at 365 nm while the UV acrylic completely removed this component. The UV acrylic sheet showed the biggest reduction in T topping while staying close in value to the original (unfiltered exposure) dose. The UV acrylic filter both filtered out most of the light components at and below the i-line.

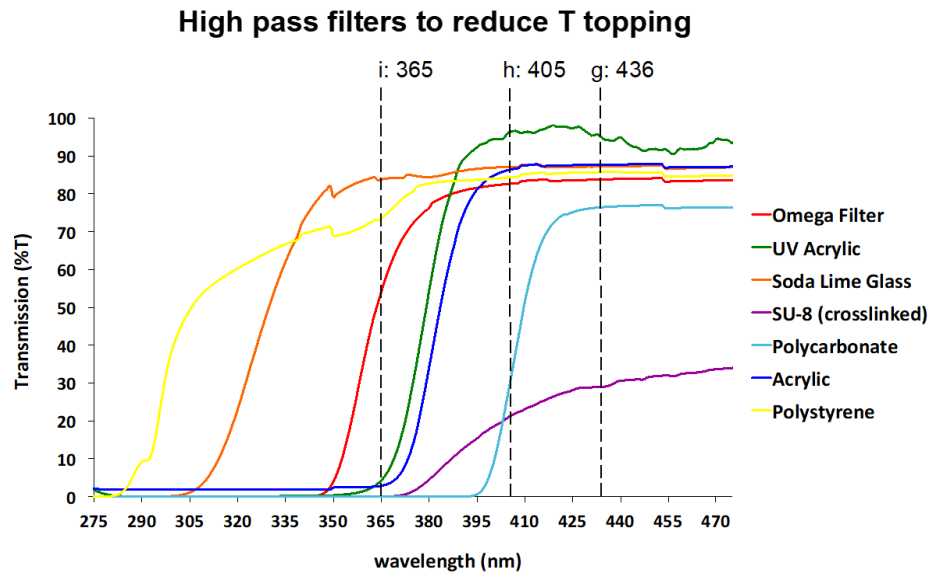


Figure 4.11. A Transmission Spectrum Showing Various Filters for Their Ability to Act as Long Pass Wavelength Filters. Removing Wavelengths Below 365 nm When Exposing SU-8 Reduces the T Topping Effect.

Out of all seven of the wavelength filters, the UV acrylic showed the most improvement in T topping while not having to drastically alter the exposure dose and recipe. This product was purchased from A&C Plastics (Optix 0001 Clear Acrylic, 0.60"). Therefore, the UV acrylic sheet was used as a wavelength filter for all of the experiments. Figure 4.12 shows the difference between a non-filtered SU-8 exposure and an exposure that was filtered using the UV acrylic. Figure 4.12A clearly shows the T topping effect. It is noticeable on both the left and right upper portions of the cross-section SEM image. However, in Figure 4.12 the SEM image shows a dramatic reduction in T topping.

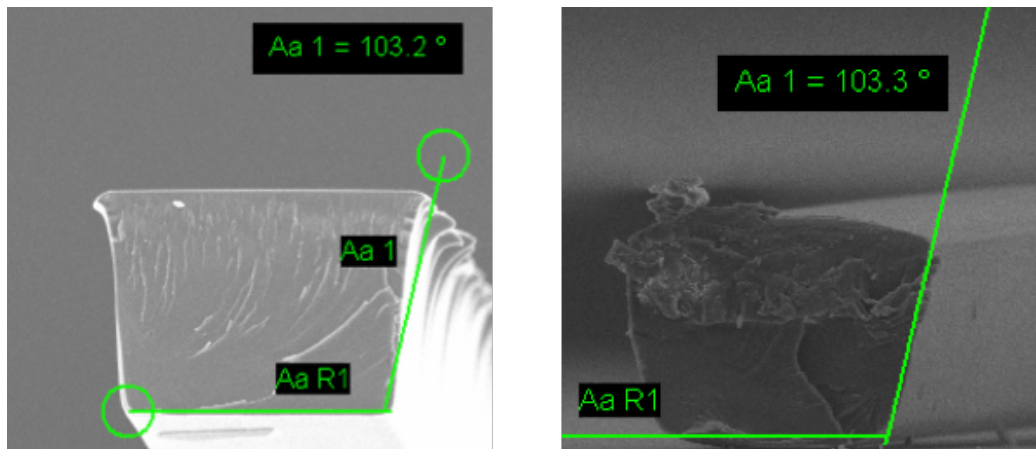


Figure 4.12. SEM Images Showing Cross-sections of Photoresist Structures. (A) T Topping is Noticed When the Photoresist is Exposed without a Longpass Wavelength Filter. (B) T Topping is Significantly Reduced When a Long Pass Exposure Filter is Used.

Device Fabrication (MLR)

Fluidic dams with overcut sidewalls were fabricated using SU-8 photoresist with a multi-layered resist (MLR) approach. SU-8 3005 was chosen because a DRIE tool was not available to etch deep trenches into glass substrates and SU-8 3005 had the following properties: optically transparent, easily etched with a standard RIE, a high refractive index material, good adhesion to SiO₂ and gold, thick layers could be patterned, and that SU-8 has been well documented as a structural layer.¹⁸⁻²² Using the MLR approach allowed for sidewalls to have slopes between 50° and 70°. Values in the range to be coated when using a line-of-sight deposition technique like e-beam evaporation. Positive tone photoresists do have overcut profiles, but the slopes are typically closer to 85°. Also, no positive tone photoresist met all of the needs listed above for SU-8 3005.

The MLR fabrication process is shown in Figure 4.13. Photomask designs were devised in CAD software. Each design contained fluidic dams of either 30 μm, 40 μm, 50 μm, or 75 μm widths. Glass substrates were thoroughly cleaned by immersion in a piranha bath (H₂SO₄ and H₂O₂), rinsed with H₂O, dried with a stream of N₂, and then further cleaned with O₂ plasma. The cleaned substrates were then dehydrated at 170°C on a hot plate for 10 minutes to evaporate off any H₂O. Adhesion promoter, HMDS (Microchem MCC Primer 80/20), was then coated on the substrate. SU-8 3050 (Microchem Corp.) was spin applied at 3000 rpm, which afforded a thickness of 35 μm, confirmed with a profilometer. This layer of SU-8 acted as a structural layer, which could be easily etched with a standard reactive ion etcher (RIE), as an ICP or DRIE system was

not available. The edge bead of the SU-8 was then removed. The substrate was then soft baked at 95°C on a hot plate for 20 minutes and ramped down to 30°C at a rate of 5°C/min. Using an OAI 8008 mask aligner the substrate was flood exposed (no photomask) using a piece of UV acrylic as a long-pass wavelength filter to remove wavelengths 365 nm and below. The exposure was performed at a dose of 450 mJ/cm² (29.35 seconds at 15.33 mW/cm²). A post exposure bake (PEB) was performed immediately after exposure. A hot plate was set to 95 °C for 8 minutes. The PEB time suggested on by the photoresist manufacturer was lengthened to provide optimal results. The PEB process was ramp down at 5°C/min and the substrate was removed at 30°C. A layer of 100 nm of SiO₂ was deposited by physical vapor deposition (Kurt Lesker PVD75). The substrate was then O₂ plasma cleaned. A second layer of photoresist (JSR Chemicals, NFR 016D2) was spin applied at 3000 rpm to yield a 3.5 μm thickness, confirmed with profilometer. A soft bake step ensued at 90°C on hot plate for 90 seconds. This was followed by exposure through the CAD designed photomask. A dose of 100 mJ/cm² (6.52 seconds with an intensity of 15.33 mW/cm²) was used to expose the photoresist. The optimal dose of 100 mJ/cm² was found after doing an exposure dose matrix and checking the dimensions with an optical microscope and profilometer. A PEB was performed on a hot plate at 90°C for 90 seconds. Develop ensued in PD523AD developer for 60 seconds. This was followed by immersion into a DI H₂O bath, rinsing with DI H₂O stream, and blown dry with N₂ gas. A reactive ion etcher (LAM Rainbow 4400) used CF₄ with 10% O₂ to etch the SiO₂ layer using the patterned JSR NFR resist as

an etch mask. The etch gases were then changed to purely O₂, which was used to etch the SU-8 layer. During the O₂ dry etch, the remaining JSR NFR resist was removed and the remaining SiO₂ layer acted as an etch mask for SU-8. This process yielded a fluidic dam with overcut sidewalls of 80° or less. Sidewalls with angles less than 80° are easily coated with a PVD process. The next step was metal deposition by evaporation. Titanium (4 nm), gold (250 nm), titanium (4 nm), and SiO₂ (100 nm) were deposited atop the substrate.

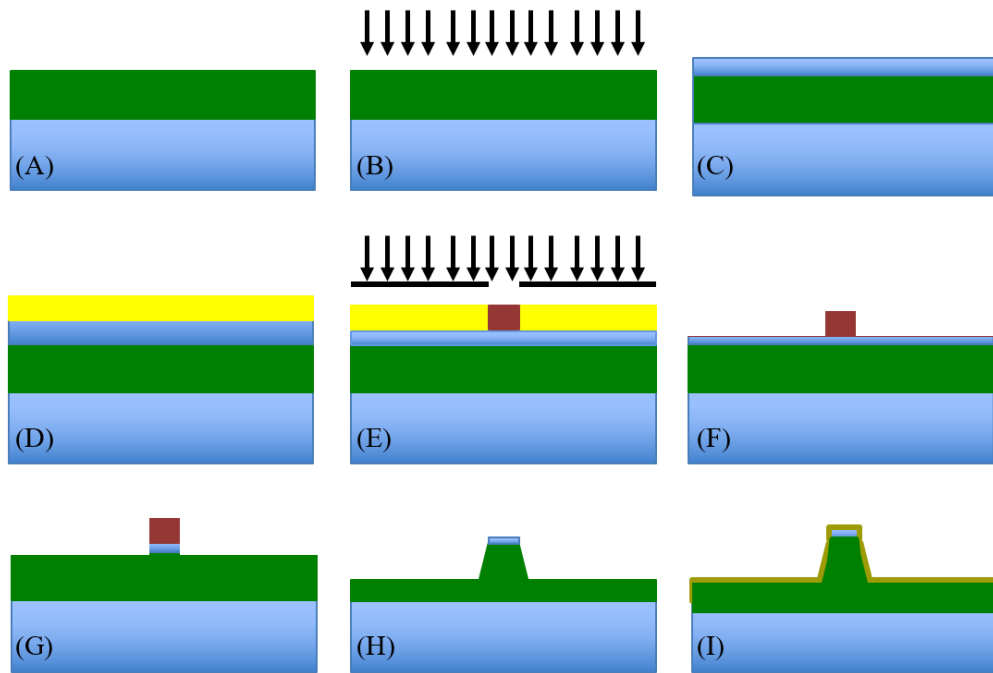


Figure 4.13. Fabrication Process for the Flow-over Fluidic Dam with Overcut Sidewall Profile Using a Multi-layered Resist (MLR) Method. (A) Spin Apply SU-8 Photoresist and Soft Bake, (B) Flood Expose and Post Exposure Bake the SU-8, (C) Deposit 100 nm of SiO₂ Atop the Cross-linked SU-8 Structural Layer, (D) Spin Apply JSR NFR 016D2 Photoresist, (E) Expose the JSR NFR Photoresist through the Photomask with Design of the Flow-over Dam, (F) Post Exposure Bake and Develop the JSR NFR, (G) Dry Etch the SiO₂ Layer with a CF₄/O₂ Plasma, (H) Dry Etch the SU-8 Layer with an O₂ Plasma, (I) Deposit 4 nm Ti, 250 nm Au, 4 nm Ti, and 100 nm SiO₂.

Optical Microscopy of Overcut Sidewalls

After the MLR method was employed, optical and electron microscopy was performed to visualize the structure and gain insight into the slope sidewalls. Figure 4.14A shows an optical microscope image (top-down view) of a fluidic dam made with the 50 μm mask. This fluidic dam was etched to a depth of 25 μm . This image clearly shows that the bottom portion of the fluidic dam is wider than the top. Figure 4.14B shows a cross-section SEM image of a fluidic dam. This fluidic dam was made with the 75 μm photomask design. The dam in this image was etched to a depth of 7.5 μm . The optical image in Figure 4.14C shows a top-down view of a fluidic dam made with a 75 μm photomask. This optical image shows a top dam width of 68.55 μm and a base of 89.59 μm . This dam was etched to a depth of 23 μm . Using a right triangle with the hypotenuse as 23.0 μm and one side with a length of 10.52 μm , the sidewall slope was calculated to be 62.78°. Figure 4.14D shows an optical image with the focus on the top portion of the dam. The image was then colored. This made it easy to see the in focus upper plane of the dam and the out of focus lower portion of the dam. The top portion of this dam measured 42.37 μm and the bottom portion measured 69.89 μm . This dam was also etched to a depth of 23 μm . Using another right triangle with the hypotenuse as 23.0 μm and one side with a length of 13.76 μm , the sidewall slope was calculated to be 53.25°.

After performing the MLR method, the device consists of a glass substrate with SU-8 and SiO₂ deposited (Figure 4.15A). Therefore, it is completely transparent. Only

after metal deposition does the substrate become opaque (Figure 4.15B). The metal deposition consists of a 4 nm Ti adhesion layer, 250 nm of Au, a second 4 nm Ti adhesion layer, and then a 100 nm SiO₂ layer, which functions to prevent non-specific binding to the surface. At this point, nanostructures are milled through the top layer of SiO₂ and through the metal layers.

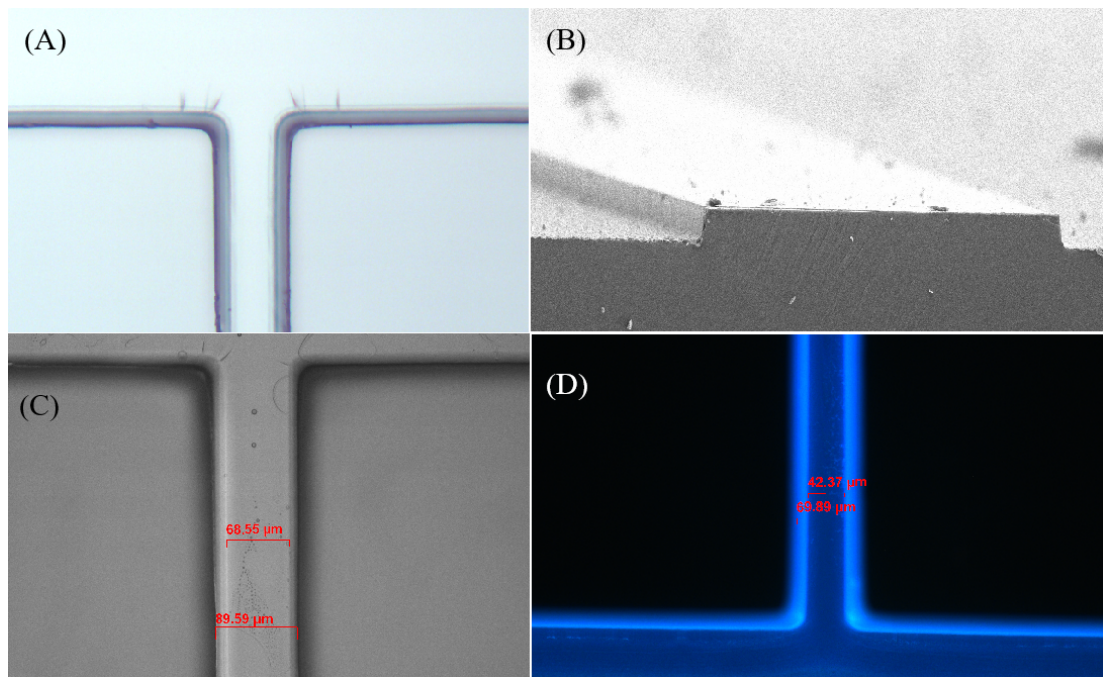


Figure 4.14. (A) Optical Microscope Image Showing an Overcut Fluidic Dam. (B) SEM Cross-section Image Showing the Overcut Sidewall Profile. Dimensions of Dam are 75 μm Wide x 7.5 μm Tall. (C) Optical Microscope Image Showing an Overcut Fluidic Dam. The Fluidic Dam Dimensions are 68.55 μm Wide at the Top of the Dam and 89.59 μm Wide at the Base of the Dam. (D) A Colored Optical Microscope Image Showing an Overcut Fluidic Dam. The Fluidic Dam Dimensions are 42.37 μm Wide at the Top of the Dam and 69.89 μm Wide at the Base of the Dam.

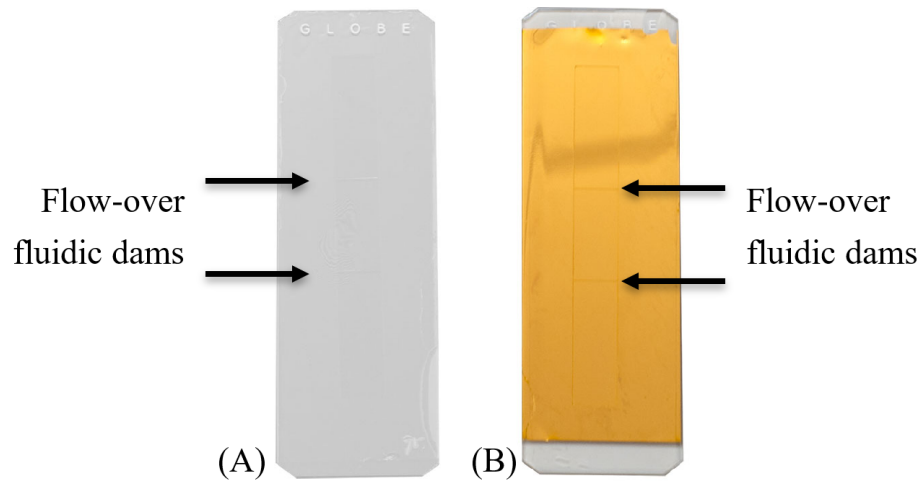


Figure 4.15. Photograph of a Glass Substrate (A) after Lithography with Clear SU-8 Forming Two Flow-over Dams on the Substrate and (B) after Metal Deposition.

Nanostructuring the Substrate

Focused ion beam (Zeiss, Auriga) milling was used to manufacture nanostructures into the planar top of the flow-over dam. Nanoledge structures (stair step features) were milled into substrates with and without a SiO₂ capping layer (Figure 4.16). First, a 280 nm wide ledge was milled 100 nm into the gold film. A 50 nm slit was milled into the center of the 280 nm step and was milled completely through the remaining gold film. The pair, 280 nm step with 50 nm slit, made a complete nanoledge. An array of these single nanoledge structures consisted of 100 nanoledges, evenly spaced 600 nm apart. The 280 nm ledge and the 50 nm inner slit were chosen as optimized structures. See our lab group's previous work (Chapter III) for details.²³

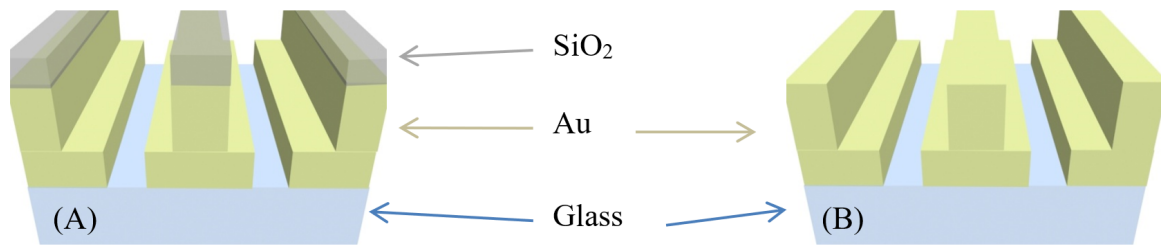


Figure 4.16. Schematic of FIB Milled Structure (A) with SiO₂ Capping Layer and (B) without SiO₂ Capping Layer.

Charge Accumulation When Nanostructuring Insulating Layers

Irradiation of an insulating layer, such as a SiO₂ capping layer (Figure 4.16A), with an ion beam can lead to some undesired effects. Ion beams are typically made of Ga⁺ ions. Therefore, the ion beams create a buildup of positive charge on the sample surface during milling. Charge from the ion beam accumulates on the dielectric layer. Without a path to ground, this accumulation of charge can cause a deflection of the ion beam. This leads to a drift in the milled structure. To showcase this, a rectangular design (Figure 4.17A) was entered into the focused ion beam patterning software. This shape was milled into a substrate with a SiO₂ capping layer. SEM microscopy was used to visualize the milled substrate. The SEM image (Figure 4.17B) shows a slanted rectangle that was milled with the ion beam. The drifting from charge accumulation is clearly evident. Figure 4.17C shows the resultant structure for ease of comparison to Figure 4.17A.

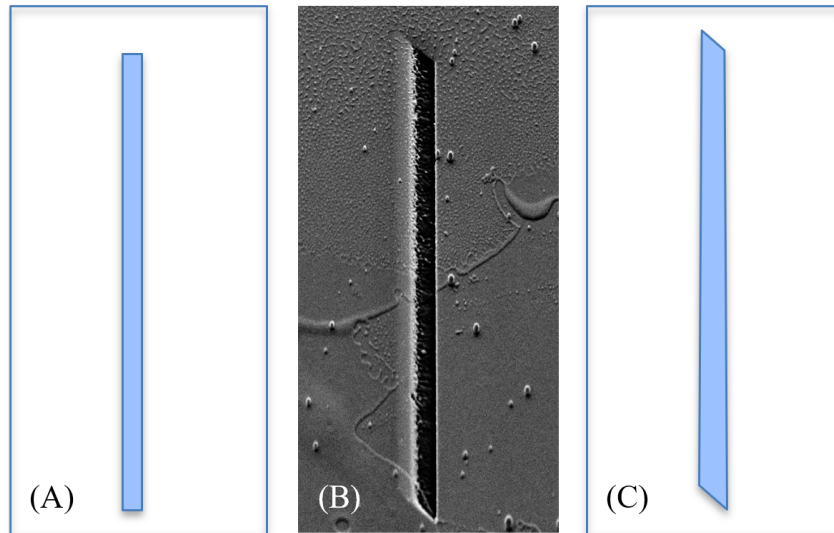


Figure 4.17. (A) A Schematic Showing the Rectangular Design That Was Entered into the Focused Ion Beam Patterning Software. (B) A SEM Image Showing a Nanoslit Structure That Was Milled into a Substrate with a SiO₂ Capping Layer. The Ends of the Rectangle Show a Slant Due to Charge Accumulation Which Caused Drifting. (C) A Schematic Showing the Resultant Slanted Rectangle.

Milling structures into an electrically conductive substrate, such as a metal substrate (Figure 4.16B), is preferred over substrates with insulating layers (Figure 4.16A) due to this charging effect and thus drifting of the structure. Typically, insulating layers are coated with a metal during a sputter coating that precedes ion beam milling. For optical devices this metal coating must be removed. It is not ideal to sputter coat the substrate and at a later time be required to fully remove the coating. Removal of a metal coating is time consuming and it becomes difficult to completely remove the metal layer. In light of this, a new method was formulated. In place of the metal coating, a metal foil is used to encase the substrate. The sample with SiO₂ capping layer was wrapped with a thin foil of aluminum (Figure 4.18), a small window cut in the foil near the area of

interest, and then FIB milling ensued. This drastically improves the charge accumulation and thus the drifting effect when milling structures.

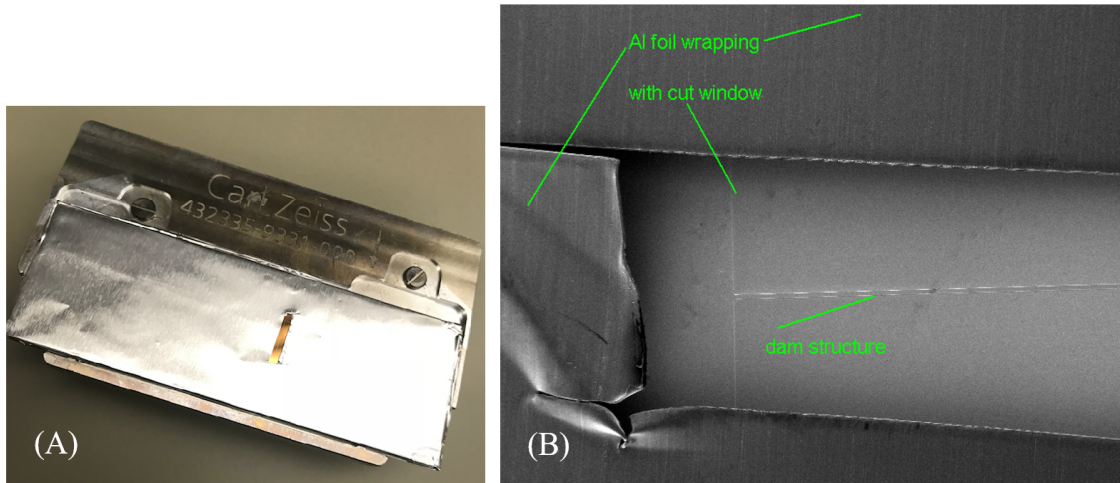


Figure 4.18. A Photograph of a Chip after the Microfabrication of the Fluidic Dam, Metal Deposition, and SiO₂ Deposition. The Chip is Wrapped with a Foil of Aluminum and a Small Window is Cut around the Area of Interest (the Fluidic Dam). The Foil Functions to Displace Charging and Minimize Drift during Milling without the Need for Sputter Coating the Chip.

Figure 4.19 shows a device with an SiO₂ capping layer that was milled using a foil wrap. Notice that on the left side of the flow-over dam a large box (100 μm x 75 μm) was milled into the dam. The edges and lines of the box are sharp and the box does not slant. On the right side of this SEM image is an array of 100 nanoedges, which are also straight with no slant. Figure 4.20 is a FIB image which shows a magnified view of the nanoedge array from Figure 4.19. The FIB image shows good contrast between the nanoedges (exposed gold) and the SiO₂ topped areas (areas that were not

nanostructured). The areas with exposed gold show up as bright while the areas covered in SiO₂ show up as darker in the FIB image.

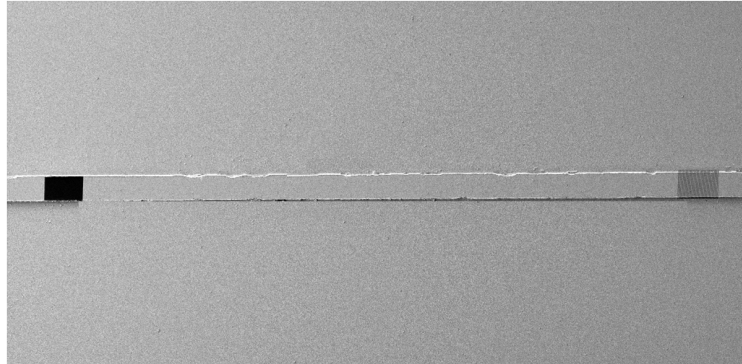


Figure 4.19. A SEM Image Showing a Flow-over Fluidic Dam with a Reference Window Milled on the Left Side and an Array of Nanostructures Milled on the Right Side of the Dam.

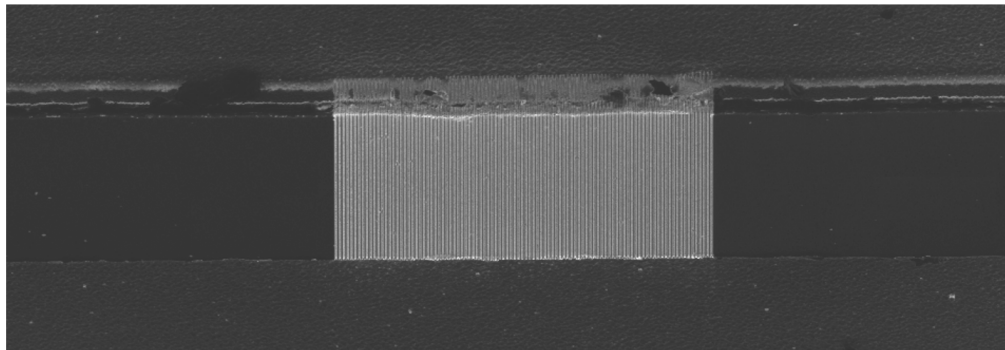


Figure 4.20. A FIB Image Showing a Flow-over Fluidic Dam with an Array of Nanoedge Structures Milled into the Dam.

Conclusion

Flow-over fluidic dams were fabricated for use in plasmonic biosensors. Fluidic dams had a range of sidewall angles, between 50° and 123°. The undercut and T topped

sidewalls were problematic for plasmonic biosensing due to their transparent sidewalls after metal deposition. A significant reduction in T topping was observed by using UV acrylic as a long pass wavelength filter during photoresist exposure. Overcut sidewalls (angles between 50° and 70°) were needed to yield opaque sidewalls after metal deposition. This was achieved with a multi-layered resist (MLR) approach. Nanostructuring on a dielectric (SiO₂) topped substrate was achieved without a sputter coating by wrapping the device in a foil of aluminum and cutting a small window in the foil around the area of interest. With the foil wrap and without a metal coating, no charging or drifting was noticed during the nanostructuring of the SiO₂ capped substrates.

Discussion of Techniques

Why Use the Multi-Layered Resist (MLR) Method?

Several traditional microfabrication techniques were pursued before attempting the MLR method. Access to only a standard reactive ion etcher (RIE) was the reason some of the techniques below were unsuccessful. The experience of attempting these techniques is written here to benefit those in a similar setting and who lack access to a RIE with a powerful plasma, such as an ICP-RIE or DRIE system. The techniques that were originally pursued include the following: (a) wet etching with a photoresist etch mask, (b) dry etching with a photoresist etch mask, (c) dry etching with metal etch mask, (d) dry etching with SU-8 etch mask, (e) the use of polymeric substrates, and (f) backside exposure of photoresist. Brief descriptions of each process are outlined below.

Wet etching with a photoresist etch mask. A glass substrate was thoroughly cleaned (piranha solution, O₂ plasma), dehydrated, and then adhesion promoter (HMDS, hexamethyldisilazane) was spin applied. Shipley 1827 photoresist was spin applied, baked, exposed through a photomask with a fluidic dam structure, developed, and hard baked. The photoresist was to serve as an etch mask. The device was wet etched with a 6:1 BOE (Transene, buffered oxide etchant) solution. The photoresist was stripped and the substrate was inspected by optical and electron microscopy.

An electron microscope image of the dam structure is shown in Figure 4.21. The fluidic dam shows rough sidewalls, likely due to under etching due to poor photoresist adhesion. To remedy this problem, another adhesion promoter (Microchem Corp., MCC Primer 80/20) was attempted but to no avail.

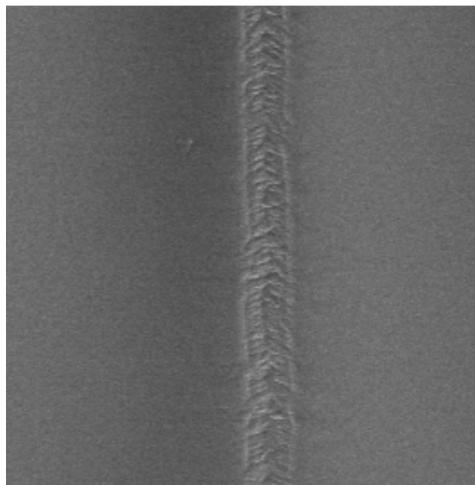


Figure 4.21. SEM Image Showing a Flow-over Dam with a Rough Surface Due to Under Etching and a Non-planar Top to the Dam.

Several other photoresist were attempted, yet the situation did not improve dramatically. A second issue, also apparent from the SEM image (Figure 4.21), is that wet etching removed the planar top portion of the dam. This became an issue because it was very difficult to perform focused ion beam (FIB) milling on a non-planar substrate.

Dry etching with a photoresist etch mask. Using the same protocol that is outlined above in wet etching with a photoresist etch mask, the substrate was dry etched as opposed to wet etched. A LAM Rainbow 4400 reactive ion etcher (RIE) was used to transfer the pattern of the photoresist into the glass substrate. The etch selectivity between the soft photoresist etch mask and the glass substrate led to a problematic situation. The photoresist etch mask was completely removed and etched away before the glass substrate was etched vertically to a sufficient depth. The glass was only etched to a depth of a few hundred nanometers before the photoresist etch mask was removed.

Dry etching with a metal etch mask. In order to solve the issue in dry etching with a photoresist etch mask and increase the etch selectivity between the etch mask and the substrate, a metal etch mask was used. The process for obtaining a metal etch mask on the glass substrate is outlined in Figure 4.22. Briefly a glass slide was cleaned and a metal (Al or Ni) was evaporated onto the substrate. A photoresist was applied and patterned. The metal layer was wet etched using the photoresist as a wet etch masking layer. The photoresist layer was stripped and what remained was patterned metal on a glass substrate.

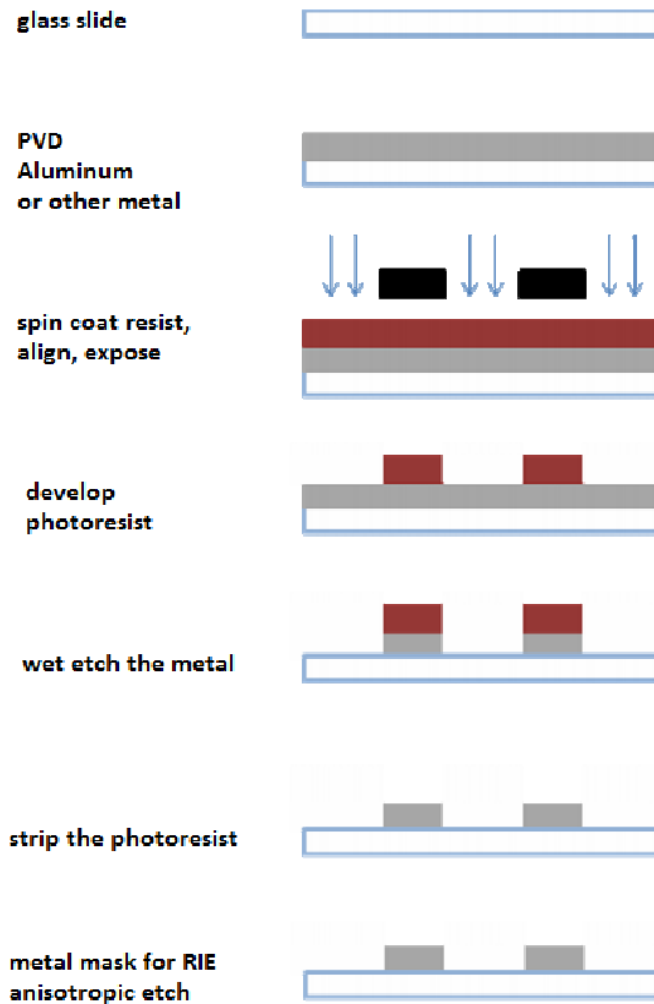


Figure 4.22. Process for Making a Metal Etch Mask.

A very rough surface was observed with SEM (Figure 4.23). A micro-masking effect was observed. Micro-masking is when small pieces of the metal etch mask are lifted during the dry etch process. They are then re-deposited on the glass portion of the substrate. This leads to a situation where metal micro-particles act as etch masks on areas of the device that were intended to be metal free. This leads to a very rough surface.

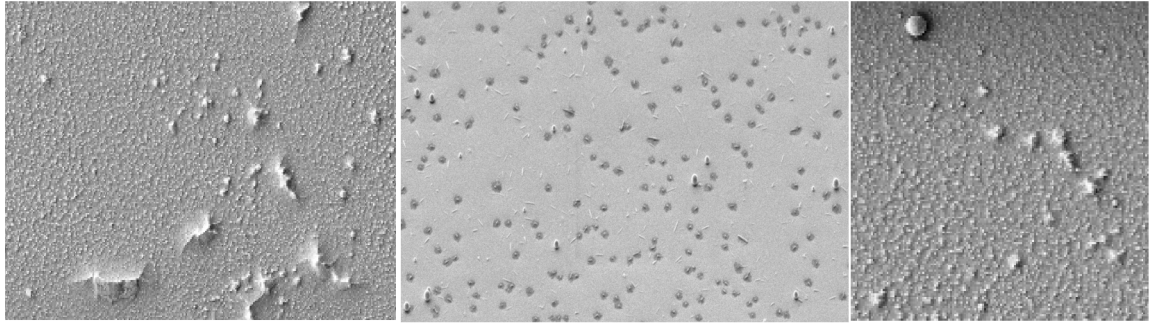


Figure 4.23. SEM Image Showing a Rough Surface. The Roughness is Due to Micro-masking When Reactive Ion Etching a Glass Substrate with a Metal (Al, Ni) Etch Mask.

Dry etching with SU-8 etch mask. It is well documented that SU-8 photoresist (Microchem Corp) has high etch selectivity when compared to other photoresists. Therefore, SU-8 photoresist was patterned onto a glass substrate and was to be used as an etch mask. A SU-8 etch mask was thought to have high etch selectivity (similar to the metals above) but would not cause micro-masking. No micro-masking was observed and SU-8 provided good etch selectivity. The primary issue with this method was that the LAM Rainbow 4400 did not have the plasma power to etch the glass substrate to a micron level depth in a reasonable amount of time. Figure 4.24 shows a profilometry scan of a glass substrate after dry etching for 1.5 hours. The etch depth achieved was 180 nm in this time. Therefore, it would take 58.3 hours to reach the desired depth of 7 μm .

Profilometry of dry etched glass substrate

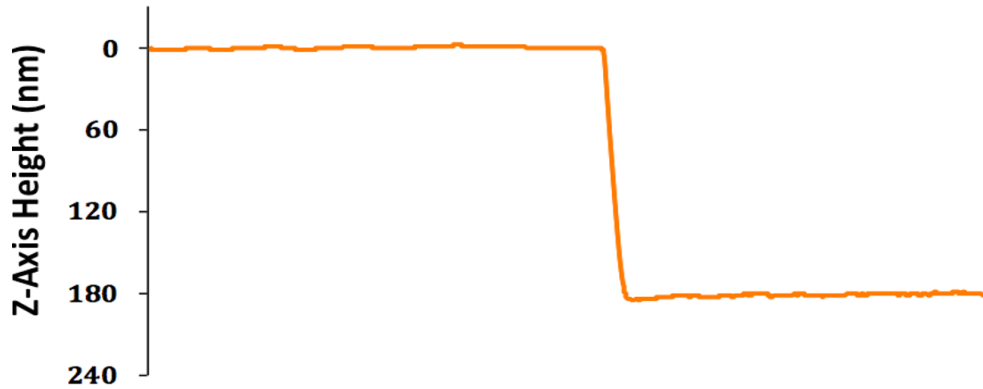


Figure 4.24. Profilometry Scan Showing an Etch Depth of 180 nm after a 1.5-hour Dry Etch.

The use of polymeric substrates. Polymers are easily etched in an O₂ plasma while glass substrates are difficult to etch to a micron depth without a high-powered plasma. Thus, several polymeric substrates were considered. Acrylic, polystyrene, and polycarbonate substrates were investigated to replace the glass substrates, which were proving very difficult to etch. Most all of the photoresists used were found to be compatible with the polymeric substrates. A major issue was in the development step. During the development of the exposed photoresist, the developer solution etched away at the polymer substrates. This is clearly shown in the photograph in Figure 4.25.

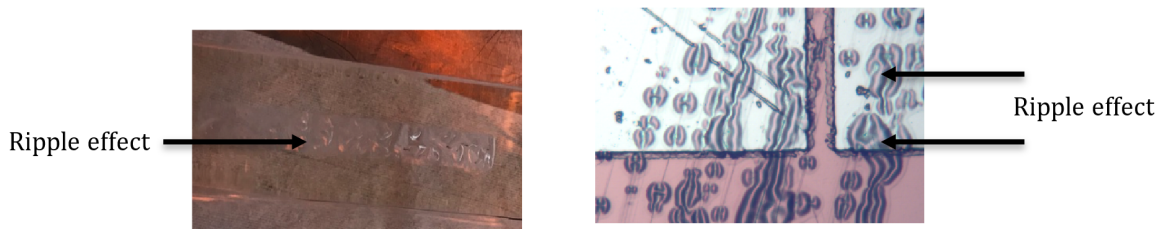


Figure 4.25. (A) A Photograph Image of a Polymeric Substrate; the Center Region Shows a Ripple Effect from the Developer Solution Dissolving the Polymer Substrate, (B) An Optical Microscope Image of a Polymeric Substrate with Patterned Photoresist Shown in Red. The Fluidic Dam is Shown with the Arrow. There is a Clear Reaction between the Substrate and the Developer Solution. The Substrate Starts to Wrinkle/Ripple in Certain Areas. This is Unacceptable, Especially for an Optical Device That Requires That Light Pass through the Substrate.

Backside exposure of photoresist. Topside exposure of SU-8 photoresist affords sidewalls that have an undercut profile. In theory, if one were to expose the photoresist from the backside (through-the-wafer), then an overcut profile could potentially be achieved with SU-8. This was attempted by exposing SU-8 from the top side with an air gap, from the topside in soft contact mode, and from the backside in soft contact mode. Figure 4.26 shows a schematic of the various types of exposure with resultant photoresist sidewall profile.

Cross-section SEM images showed the resultant sidewall angles for each type of exposure. Figure 4.27A shows a sidewall angle of 122.9° for the device exposed through the topside with an exposure gap of 1 mm. Figure 4.27B shows a sidewall angle of 98.7° for the device exposed through the topside with no gap (soft contact mode). Finally, the device that was exposed though-the-wafer (backside) in soft contact mode did improve

the sidewall angles. The sidewalls were 89.1° , as shown in Figure 4.27C. These straight sidewalls could not be coated when metal was evaporated onto the substrate.

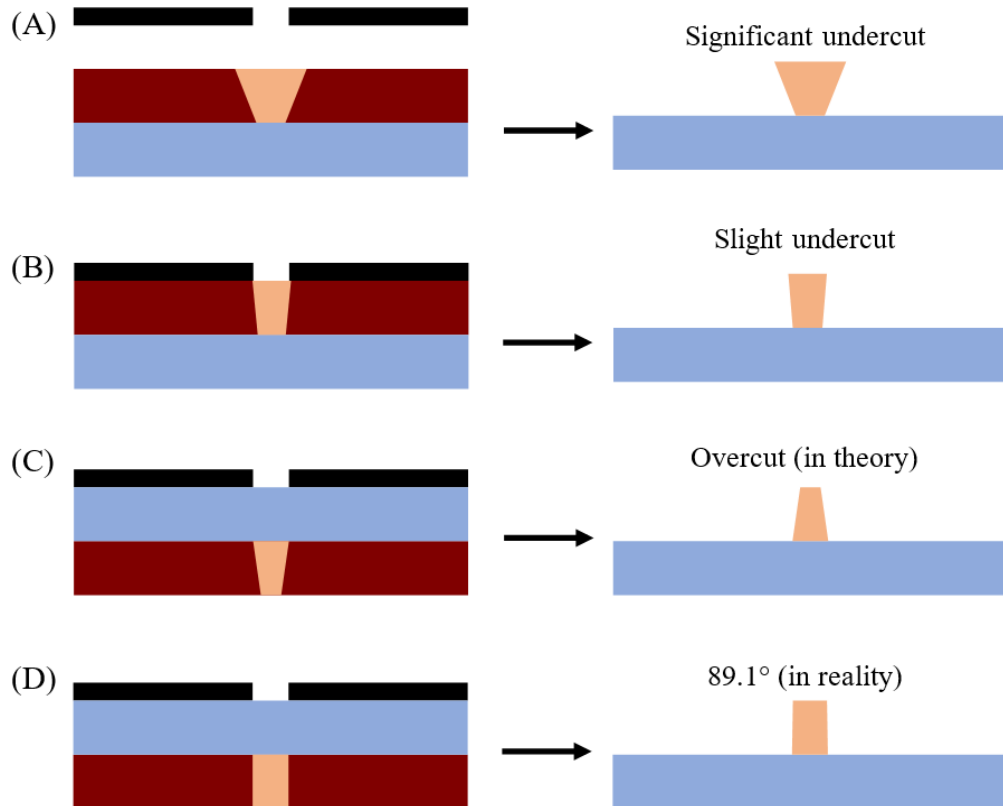


Figure 4.26. Schematics Showing Topside and Backside Exposure of a Photoresist through a Photomask and the Resultant Shape of Patterned Photoresist. Glass Substrate is Shown in Blue, Photoresist in Red, Cross-linked Photoresist in Orange, and the Photomask in Black. (A) Topside Exposure through an Exposure Gap Results in a Structure with Significant Undercut on the Photoresist Sidewalls. (B) Topside, Soft Contact Exposure Results in a Slight Undercut. (C) In Theory a Backside (Through-the-Wafer) Exposure in Soft Contact Mode Should Result in an Overcut Profile. (D) But in Reality, Backside Exposure in Soft Contact Mode Results in a Structure That Has 89.1° Sidewalls.

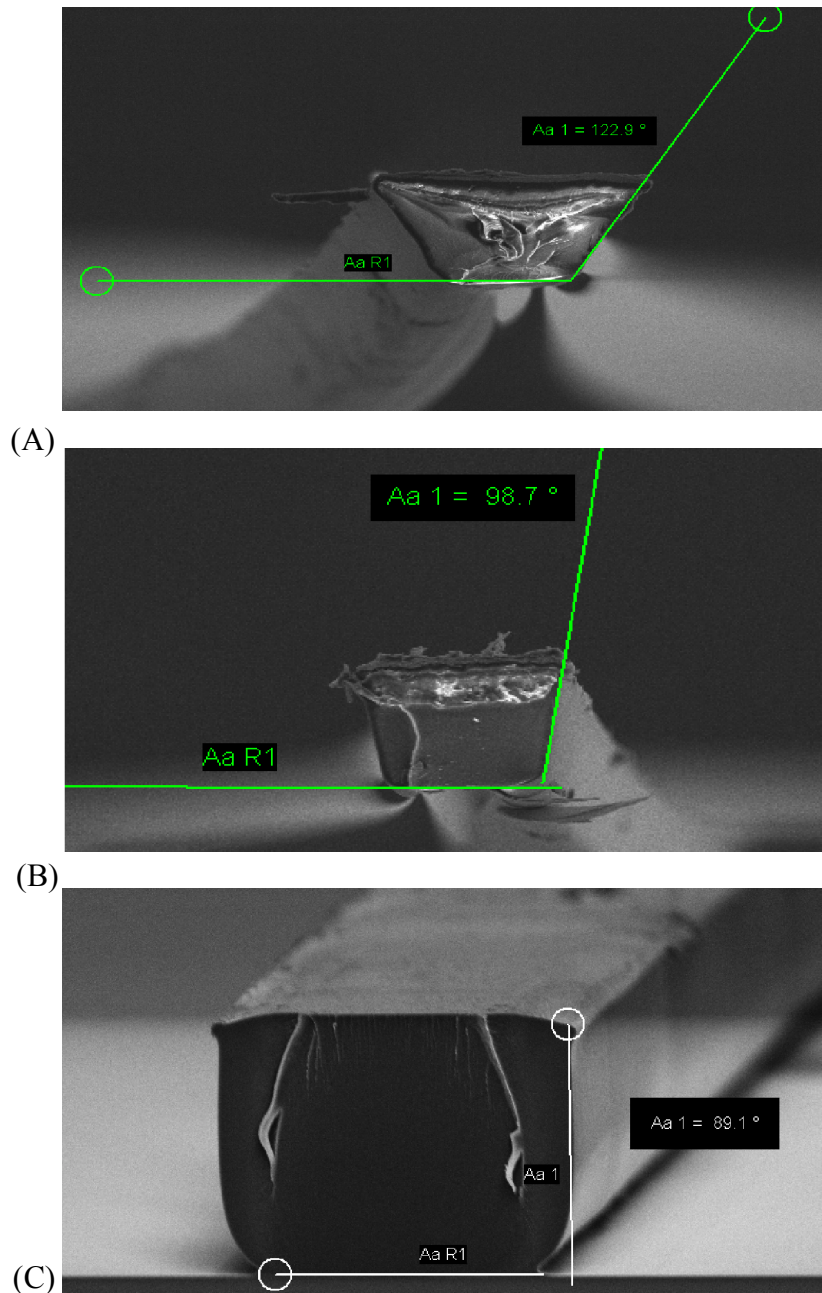


Figure 4.27. SEM Cross-section Image of a Photoresist Exposed from the (A) Topside with an Exposure Gap Yielded a Sidewall Angle of 122.9° (Undercut Profile), (B) Topside in Soft Contact Mode Yielded a Sidewall Angle of 98.7° (Undercut Profile), (C) Backside in Soft Contact Mode Yielded a Sidewall Angle of 89.1° (Straight Sidewall Profile).

References

1. Gordon, R.; Sinton, D.; Kavanagh, K. L.; Brolo, A. G., A New Generation of Sensors Based on Extraordinary Optical Transmission. *Accounts of Chemical Research* **2008**, *41* (8), 1049-1057.
2. Eftekhari, F.; Escobedo, C.; Ferreira, J.; Duan, X.; Girotto, E. M.; Brolo, A. G.; Gordon, R.; Sinton, D., Nanoholes As Nanochannels: Flow-through Plasmonic Sensing. *Analytical Chemistry* **2009**, *81* (11), 4308-4311.
3. Escobedo, C., On-chip nanohole array based sensing: a review. *Lab Chip* **2013**, *13* (13), 2445-63.
4. Toner, M.; Irimia, D., Blood-on-a-chip. *Annu Rev Biomed Eng* **2005**, *7*, 77-103.
5. Emami Ardestani, M.; Zaerin, O., Role of Serum Interleukin 6, Albumin and C-Reactive Protein in COPD Patients. *Tanaffus* **2015**, *14* (2), 134-140.
6. Terao, K.; Shimizu, K.; Miyanishi, N.; Shimamoto, S.; Suzuki, T.; Takao, H.; Oohira, F., Size-exclusion SPR sensor chip: application to detection of aggregation and disaggregation of biological particles. *Analyst* **2012**, *137* (9), 2192-2198.
7. Terao, K.; Hiramatsu, S.-i.; Suzuki, T.; Takao, H.; Shimokawa, F.; Oohira, F., Fast protein detection in raw blood by size-exclusion SPR sensing. *Analytical Methods* **2015**, *7* (16), 6483-6488.
8. Breault-Turcot, J.; Masson, J.-F., Microdialysis SPR: diffusion-gated sensing in blood. *Chem. Sci.* **2015**, *6* (7), 4247-4254.
9. Yang, Ren and Wanjun Wang. 2005. " A numerical and experimental study on gap compensation and wavelength selection in UV-lithography of ultra-high aspect ratio SU-8 microstructures." *Sensors and Actuators B* 110: 279-288.
10. Cameron, James F, Sheri L Ablaza, Guangyu Xu, and Wang Yueh. 1999. "Design and Chemistry of Advanced Deep-UV Photoresists: The Role of the Photoacid Generator." *Journal of Photopolymer Science and Technology* 12(4): 607–20.
11. Wen, Justin. 2015. "T-Topping Study Report T-Topping Study Report."

12. Lee, S.J., W. Shi, P. Maciel, and S.W. Cha. 2003. "Top-Edge Profile Control for SU-8 Structural Photoresist." Proceedings of the 15th Biennial University/Government/ Industry Microelectronics Symposium (Cat. No.03CH37488): 389–90.
13. Lenhart, Joseph L. et al. 2002. "Probing Surface and Bulk Chemistry in Resist Films Using near Edge X-Ray Absorption Fine Structure." *Journal of Vacuum Science & Technology B: Microelectronics and Nanometer Structures* 20(6): 2920. <http://scitation.aip.org/content/avs/journal/jvstb/20/6/10.1116/1.1524970>.
14. Yang, Ren. 2006. "Ultra-Violet Lithography of Thick Photoresist for the Applications in Biomems and Micro Optics." *Design* (August).
15. Limited, Semiconductor Complex. 2002. "Progress in Deep-UV Photoresists." 25(6): 553–56.
16. Wangler, N. et al. 2011. "High-Resolution Permanent Photoresist Laminate TMMF for Sealed Microfluidic Structures in Biological Applications." *Journal of Micromechanics and Microengineering* 21(9).
17. Tx, Austin. 1999. "TFAA TBA T." 4.
18. Lee, Dong E., Hang-Ping Chen, Steven A. Soper, and Wanjun Wang. 2003. "Electrochemical Micropump and Its Application in a DNA Mixing and Analysis System." In eds. Holger Becker and Peter Woias. , 264. <http://proceedings.spiedigitallibrary.org/proceeding.aspx?doi=10.1117/12.478141> (October 9, 2018).
19. Ling, Zhong G., Kun Lian, and Linke Jian. 2000. "Improved Patterning Quality of SU-8 Microstructures by Optimizing the Exposure Parameters." In ed. Francis M. Houlihan. *International Society for Optics and Photonics*, 1019. <http://proceedings.spiedigitallibrary.org/proceeding.aspx?doi=10.1117/12.388266> (October 9, 2018).
20. Lee, Dong E., Hang-Ping Chen, Steven A. Soper, and Wanjun Wang. 2003. "Electrochemical Micropump and Its Application in a DNA Mixing and Analysis System." In eds. Holger Becker and Peter Woias. , 264. <http://proceedings.spiedigitallibrary.org/proceeding.aspx?doi=10.1117/12.478141> (October 9, 2018).
21. P. D. Curtis, S. Lezekiel, R. E. Miles, and C. R. Pescod, "SU-8 as a material for integrated all-optical microwave filters," *Microwave Eng.*, April 2001, pp. 51–56.

22. Thorpe, J.R., D.P. Steenson, and R.E. Miles. 1998. "High Frequency Transmission Line Using Micromachined Polymer Dielectric." *Electronics Letters* 34(12): 1237. http://digital-library.theiet.org/content/journals/10.1049/el_19980872 (October 9, 2018).
23. Z. Zeng, M. N. Mendis, D. H. Waldeck, J. Wei, *RSC Adv.* **2016**, 6, 17196-17203.

CHAPTER V

TROPONIN T BIOSENSING

Overview

Nanostructured metal films were studied for biosensing of Troponin T protein using a DNA aptamer with localized surface plasmon resonance (LSPR) in wavelength shift mode. Here, we account a device with a microstructured, fluidic, flow-over dam with nanoledge (stair-step) features milled into the top of the dam. Fluorescent microspheres were shown to hang up on flow-over dams with undercut sidewall angles and pass over top of the dams with overcut sidewall angles. Arrays of nanoledge structures were used in the detection of Troponin T, one of the biomarkers for acute myocardial infarction (MI) or a heart attack.

Introduction

Myocardial infarction (MI), also known as a heart attack, is a condition that is one of the leading causes of death for both men and women.¹ Each year approximately 735,000 Americans suffer from a heart attack.² Chest pains are one of the early symptoms of a MI. In the United States approximately 7 million patients visit the emergency department with a complaint of chest pain.³ An estimated 50-70 % of patients presenting with chest pain in the emergency department will be placed in observation or admitted to the hospital. Approximately \$10 billion are spent annually to evaluate chest pain.⁴ Almost

100% of these patients are treated by first responders and are transported to hospitals in an ambulance.⁵ Emergency calls in regards to chest pains are one of the leading calls placed into 911 services and emergency care services. First responders are only equipped with an EKG, which is instrumentation that gives them insight into the electrical activity of the heart.⁶ An EKG (electrocardiogram) diagnoses an MI as either a STEMI or NSTEMI.⁷ For the STEMI (ST-elevation myocardial infarction) cases there is a ST wave elevation that is visible on the instrument read out.⁷ This makes diagnosing a STEMI more straightforward than a NSTEMI. In contrast to the STEMI, a NSTEMI (non-ST-elevation myocardial infarction) shows no visible ST wave elevation.⁷ With the NSTEMI cases, which make up approximately 30% of heart attacks, using electrical activity to diagnose a heart attack becomes problematic.⁸ If first responders had a point-of-care (POC) device that could definitively diagnose the STEMI and NSTEMI cases then there would be a huge benefit to the patient. Pre-hospital biomarker measurements for MI would allow for smarter triage decisions and thus faster diagnosis and treatment. There would be faster routing of patients to a facility with appropriate care. Patients with a positive troponin assay could be quickly prioritized to facilities that are equipped with a cardiac catheterization lab, which is an on-site catheterization lab. Patients with a negative troponin and a negative EKG could be monitored but not prioritized like a patient with a positive result. The time during travel to a hospital could be used to perform a biomarker (i.e. Troponin) assays. Biomarker assays in a pre-hospital environment would allow for the assignment of degrees of urgency to patients.

Lab-on-a-chip (LOC) technology and microfluidics provide key advantages over more traditional technologies. These advantages include small sample requirements, fast reaction times, multiplexing (multiple samples at one time), compact instrumentation, and portability.⁹ LOC devices with channels and dimensions on the micro- and nanoscale can be manufactured with standard lithographic techniques and therefore can be mass-produced, yielding inexpensive devices.⁹

Surface plasmon resonance (SPR) is a detection method that is gaining popularity due to its label-free and real-time detection coupled with the ability to handle complex samples.¹⁰ SPR has been reported to handle samples in complex matrices, including serum samples without sample pretreatment.¹⁰ SPR that makes use of nanostructures and/or nanostructured metal films are of further interest owing to their ability to simplify the instrumentation.¹⁰ This type of detection platforms makes a likely candidate for creating a point-of-care (POC) sensor that is easy to use, reliable, and sensitive enough to measure low concentrations of protein targets. SPR detection coupled with microfluidics and LOC technology could afford a handheld device that is capable of measuring protein biomarkers in many settings, such as a pre-hospital setting.

Surface plasmons are very sensitive to a change in refractive index (dielectric constant) and thus are well suited to detecting binding events that occur between a bound ligand and a free protein biomarker.¹¹ Localized surface plasmon resonance (LSPR) is a phenomenon that occurs when the metal structures are smaller than the wavelength of light.¹² LSPR is caused by waves of electrons (plasmons) which are “localized” within

the nanostructure.¹² Nanostructures such as nanoparticles and other shapes have been studied.¹² In addition, nanostructured metal films have also been studied.¹³ These nanostructured films contain nanostructures milled directly into the metal film. Shapes milled into the metal films include circles, lines, and rings.¹⁴ Metal films perforated with subwavelength structures make use of a phenomenon called extraordinary optical transmission (EOT).¹⁵ Researchers found that arrays of nanostructures fashioned in a periodic arrangement would transmit far more light than expected by classical theory at certain wavelengths.¹⁶ Nanostructured metal films also allow for a linear alignment of light source and detector. This type of SPR, transmission SPR (tSPR), is of interest to researchers in the field of POC sensing devices. The linear alignment and the sensitivity due to the EOT and LSPR effects could allow for a new LOC technology. Additionally, avoiding the prism, precision optics, and temperature control, which are common to total internal reflection SPR, further adds to the applicability of tSPR based sensor into a compact, handheld format.

In the work outlined here, we report on a chip (Figure 5.1) with a nanostructured metal film in transmission SPR mode amidst a flow-over fluidic dam structure for detection of troponin T protein. The flow-over dam (Figure 5.1) was fabricated with various lithographic techniques to yield a range of sidewall angles. Confocal microscopy of fluorescent beads gave insight into the ability of the micron-sized beads to pass over top of the fluidic dam. Self-assembled monolayers (SAMs) were formed on exposed gold surfaces. This allowed for easy linkage of aminated DNA aptamers to the surface. Then

troponin T protein was monitored by a wavelength shift after binding between the DNA aptamer and troponin T protein ensued.

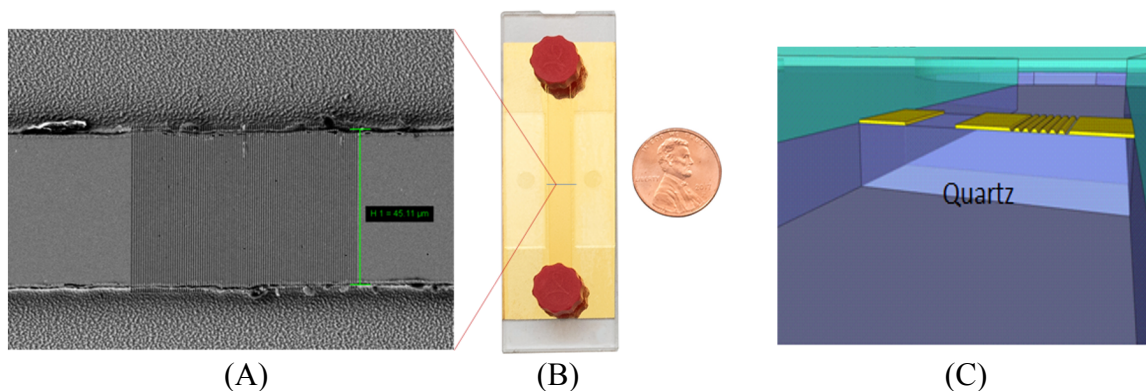


Figure 5.1. (A) Scanning Electron Microscope (SEM) Image of an Actual Flow-over, Fluidic Dam with Nanostructures Milled into the Top of the Dam; the Dam Measures 45 μm in Width and is 7 μm in Height, (B) A Plasmonic Chip with Enclosed Polyethylene Flow Chamber; the Penny is for a Scale/Size Comparison, (C) A Drawing of the Cross-section View of a Dam with Gold Thin Film atop the Dam; Into the Gold Film are a Reference Window and an Array Nanostructures.

Experimental

Device Fabrication

Devices were fabricated using lithography and focused ion beam (FIB) milling. A multi-layered resist (MLR) method was used in order to achieve sidewalls sloped in the desired direction. Several photomask designs were devised in a CAD software. Each design contained fluidic dams of either 30 μm , 50 μm , or 75 μm widths. Glass substrates were thoroughly cleaned by immersion in a piranha bath (H_2SO_4 and H_2O_2), rinsed with H_2O , dried with a stream of N_2 , and then further cleaned with an O_2 plasma. The cleaned substrates were then dehydrated at 170°C on a hot plate for 10 minutes to evaporate off

any H₂O. Adhesion promoter, HMDS (Microchem MCC Primer 80/20), was then coated on the substrate. SU-8 3050 (Microchem Corp.) was spin applied at 3000 rpm, which afforded a thickness of 35 μm, confirmed with a profilometer. This layer of SU-8 acted as a structural layer, which could be easily etched with a standard reactive ion etcher (RIE), as an ICP or DRIE system was not available. The edge bead of the SU-8 was then removed. The substrate was then soft baked at 95°C on a hot plate for 20 minutes and ramped down to 30°C at a rate of 5°C/min. Using an OAI 8008 mask aligner the substrate was flood exposed (no photomask) at a dose of 450 mJ/cm² (29.35 seconds at 15.33 mW/cm²). A post exposure bake (PEB) was performed immediately after exposure. A hot plate was set to 95 °C for 8 minutes. The PEB time suggested on by the photoresist manufacturer was lengthened to provide optimal results. The PEB process was ramp down at 5°C/min and the substrate was removed at 30°C. A layer of 100 nm of SiO₂ was deposited by physical vapor deposition (Kurt Lesker PVD75). The substrate was then O₂ plasma cleaned. A second layer of photoresist (JSR Chemicals, NFR 016D2) was spin applied at 3000 rpm to yield a 3.5 μm thickness, confirmed with profilometer. A soft bake step ensued at 90°C on hot plate for 90 seconds. This was followed by exposure through the CAD designed photomask. A dose of 100 mJ/cm² (6.52 seconds with an intensity of 15.33 mW/cm²) was used to expose the photoresist. The optimal dose of 100 mJ/cm² was found after doing an exposure dose matrix and checking the dimensions with an optical microscope and profilometer. A PEB was performed on a hot plate at 90°C for 90 seconds. Develop ensued in PD523AD developer for 60 seconds. This was followed

by immersion into a DI H₂O bath, rinsing with DI H₂O stream, and blown dry with N₂ gas. A reactive ion etcher (LAM Rainbow 4400) used CF₄ with 10% O₂ to etch the SiO₂ layer using the patterned JSR NFR resist as an etch mask. The etch gases were then changed to purely O₂, which was used to etch the SU-8 layer. During the O₂ dry etch, the remaining JSR NFR resist was removed and the remaining SiO₂ layer acted as an etch mask for SU-8. This process yielded a fluidic dam with overcut sidewalls of 80° or less. Sidewalls with angles less than 80° are easily coated with a PVD process. The next step was metal deposition by evaporation. Titanium (4 nm), gold (250 nm), titanium (4 nm), and SiO₂ (100 nm) were deposited atop the substrate.

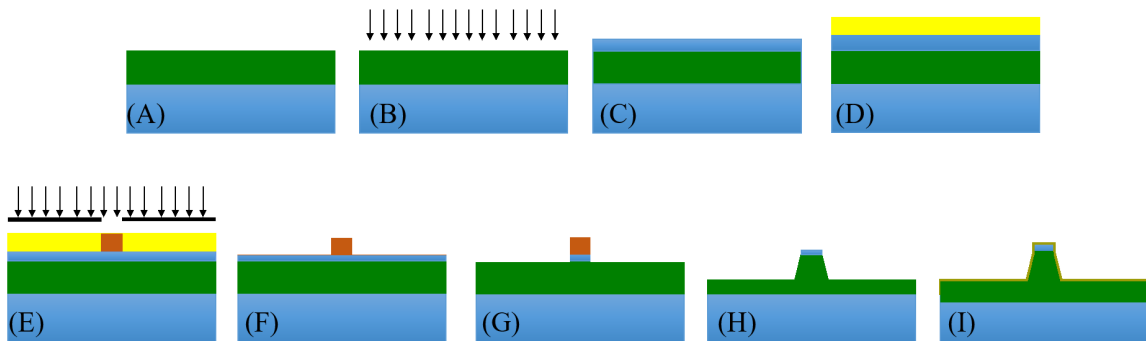


Figure 5.2. Fabrication Process for the Flow-over Fluidic Dam with Overcut Sidewall Profile Using a Multi-layered Resist (MLR) Method. (A) Spin Apply SU-8 Photoresist and Soft Bake, (B) Flood Expose and Post Exposure Bake the SU-8, (C) Deposit 100 nm of SiO₂ atop the Cross-linked SU-8 Structural Layer, (D) Spin Apply JSR NFR 016D2 Photoresist, (E) Expose the JSR NFR Photoresist through the Photomask with Design of the Flow-over Dam, (F) Post Exposure Bake and Develop the JSR NFR, (G) Dry Etch the SiO₂ Layer with a CF₄/O₂ Plasma, (H) Dry Etch the SU-8 Layer with an O₂ Plasma, (I) Deposit 4 nm Ti, 250 nm Au, 4 nm Ti, and 100 nm SiO₂.

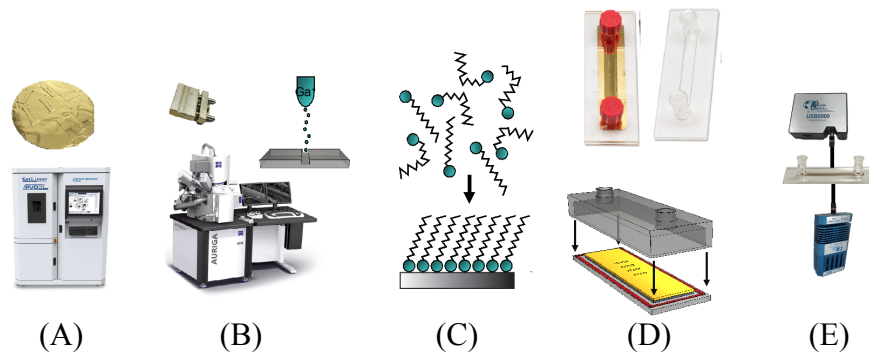


Figure 5.3. An Overview of the Fabrication Process is as Follows: (A) Thin Film Deposition, (B) Nanostructuring by Focused Ion Beam Milling, (C) Surface Chemistry by Self Assembly, (D) Flow Chamber Fabrication and Bonding to Chip, and (E) Transmission SPR Measurement.

Nanostructuring the Substrate

Focused ion beam (Zeiss, Auriga) milling was used to manufacture nanostructures into the planar top of the 75 μm dam. A step feature, 280 nm wide, was milled completely through the SiO_2 capping layer and 100 nm into the gold film. A 50 nm slit was milled into the center of the 280 nm step and was milled completely through the remaining gold film. The pair, 280 nm step with 50 nm slit, made a complete nanoledge. An array of these single nanoledge structures consisted of 100 nanoledges, evenly spaced 600 nm apart. The 280 nm ledge and the 50 nm inner slit were chosen as optimized structures. See our lab group's previous work for details.¹⁷

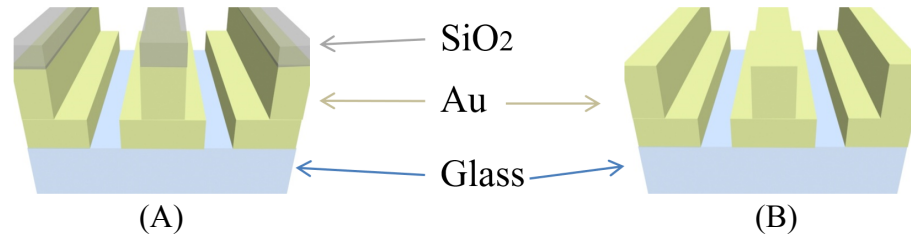


Figure 5.4. Schematic of FIB Milled Structure (A) with SiO₂ Capping Layer and (B) without SiO₂ Capping Layer.

Milling a metallic substrate is straightforward and provides no obstacles and requires no sputter coating. However, nanostructuring a substrate with non-conductive top layer, such as SiO₂, provides a charging obstacle. It is not ideal to sputter coat the substrate and at a later time be required to fully remove the coating. In light of this, a sample preparation method was developed. The sample with SiO₂ capping layer was wrapped with a thin foil of aluminum, a small window cut in the foil in the area of interest, and then FIB milling ensued, as shown in Figure 5.5. This drastically improves the charging effect and improves the drift when milling an array of nanostructures.



Figure 5.5. A Photograph of a Chip after the Microfabrication of the Fluidic Dam, Metal Deposition, and SiO₂ Deposition. The Chip is Wrapped with a Foil of Aluminum and a Small Window is Cut around the Area of Interest (the Fluidic Dam). The Foil Functions to Displace Charging and Minimize Drift during Milling without the Need for Sputter Coating the Chip.

Self-assembled Monolayer Formation

The self-assembled monolayer (SAM) was established using cystamine and glutaraldehyde chemistry. These compounds were chosen over the more typical EDC-NHS method as it has fewer process steps and affords a similar result. The step-by-step formation of the SAM is shown in Figure 5.6. A chip surface was thoroughly cleaned with an ethanol rinse, O₂ plasma clean, ethanol rinse, N₂ dry, and UV/Ozone treatment. The oxygen plasma treatment was for 5 min at 100 W in an oxygen plasma cleaner (South Bay Technologies PC-2000 Plasma Cleaner) at an O₂ pressure of 178.6 mTorr and a DC bias of -783 volts. A 5 mM solution of cystamine in 90% ethanol solution was used to form a SAM with the reaction catalyzed by a chemical microwave. The disulfide bond within the cystamine molecule breaks and yields two sulfur-gold bonds to the surface of the chip. The substrate was then rinse with a 90% ethanol solution and then rinsed with DI water in order to remove the unbound molecules. The terminal amine, sticking up from the surface, is then able to bond to a carbon oxygen double bond on next molecule, glutaraldehyde, forming an imine bond. A 2.5% solution of glutaraldehyde was used to self-assemble atop of the formed cystamine layer. This provided a terminal aldehyde group to which an aminated DNA aptamer could bind. The DNA aptamer for Troponin T-1 had the following sequence from 5' to 3':

ATACGGGAGCCAACACCAGGACTAACATTATAAGAATTGCGAATAATCATTG
GAGAGCAGGTGTGACGGAT.¹⁸ This aptamer contained 71 base pairs and had a molecular weight of 22.1 kDa, which is approximated 3 nm in size. A stock solution of

100 μM of DNA aptamer was diluted with a 10% glycerol solution to yield a 10 μM working solution. This solution was delivered to the nanostructured area of the chip and allowed to bond for several hours. The entire chip was encased in a high humidity environment during this time. Afterwards, the chip was rinsed with DI water and dried with a N_2 stream. Available sites on the metal film were blocked with a 200 μM solution of thiolated PEG 800 (poly ethylene glycol) in order to control non-specific binding.

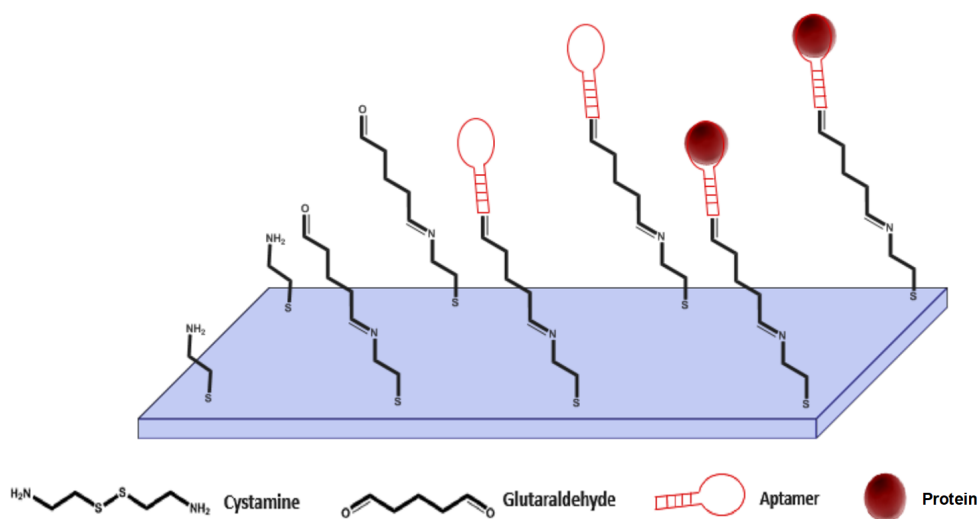


Figure 5.6. A Schematic Showing the Stepwise Sequence of the SAM Formation, DNA Aptamer Attachment, and Protein Binding to the DNA Aptamer.

The chips were reusable depending on the type of bonding used to seal the chip to the flow chamber (see Figure 5.7). In order to regenerate the clean metallic surface, the adsorbed SAM could be removed by subjecting the substrates to oxygen plasma (South Bay Technologies, PC-2000 Plasma Cleaner) for 5 minutes at 100 W. The plasma treated substrates were then exposed to sonication in acetone, ethanol, then water¹⁹ and then

cleaned for 20 minutes by UV/Ozone exposure²⁰ using a Bioforce UV/Ozone ProCleaner. It has previously been demonstrated that plasma cleaning does not adversely affect the metallic surfaces and does not add roughness to the surface.²¹ This is in contrast to the roughness and pinholes²² that can occur by some cleaning methods, such as the use of piranha (H_2SO_4 and H_2O_2).

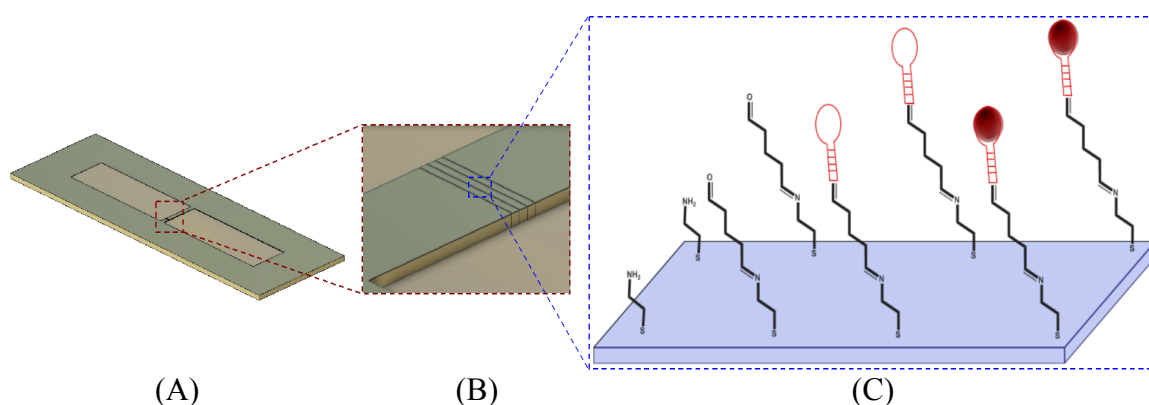


Figure 5.7. (A) A Schematic of a Chip with Fluidic Dam in the Center of the Flow Channel. (B) Magnification of the Schematic to Show the Nanostructures atop the Flow-over Dam. (C) A Procedural Drawing Showing the SAM Formation, DNA Aptamer Attachment, and Protein Binding in Single Steps (from Left to Right). The Metal Surface Forms a Bond to Cystamine, to Which Glutaraldehyde Forms an Imine Bond. An Aminated Aptamer Bonds to the Free Aldehyde of Glutaraldehyde. Troponin Protein Binds to the DNA Aptamer.

Chip and Flow-Chamber Setup

The metallic substrate with nanostructures functioned as the bottom to an enclosed flow cell with the top portion composed of a polyethylene (PE) flow chamber. This top substrate contained the flow channel, which had the dimensions 50.0 x 5.0 x 0.4 mm and a total volume of 100 μL . Prior to sealing the two pieces together, the PE flow

chamber was cleaned with a series of solvents (acetone, isopropanol, DI water) and subjected to O₂ plasma (Plasma Etch Inc. PE-100 Plasma Etch). One of three methods was used to seal the two pieces together: an adhesive (3M, VHB), polydimethyl siloxane (PDMS), or a UV active photoresist (Microchem, SU-8 3050). A syringe pump (Harvard, PHD 2000) was used to manipulate fluids through the enclosed chip and was connected to a degasser (Biotech, 2003 Degasser) to remove air bubbles from the system.

Optical Measurements

The transmission measurements through the nanostructured arrays were monitored in the spectral range of 450 nm to 1100 nm. Transmission surface plasmon resonance (tSPR) was used to monitor the binding between protein and DNA aptamer by a local RI change. This was seen as a redshift in the primary resonant peak. A tungsten halogen white light source (Ocean Optics, LS-1) was fed through a fiber optic cable and into a holder that was CAD designed and printed with a 3D printer. Fiber optics was used in order to achieve placement and focusing of the light source onto the underside of the chip. The light was collected by a 50X objective (Olympus LMPlanFLN) on an Olympus BX-41 microscope. The CCD of a Horiba Xplora was used for data collection.

Measurements were taken in real-time over the nanoslit array, a reference box of the same dimensions as the nanoslit array, and a dark background measurement, which corrected for the small amount of light that potentially transmitted through the thin metallic film. The nanostructured film, which consisted of 4 nm Ti, 250 nm Au, 4 nm Ti, and 100 nm SiO₂ in thickness, essentially blocked all of the light. The ‘dark’

measurements, those taken at a location without an opening or aperture, showed intensities in the range of 10 to 50 counts in comparison to 12000 counts for the apertures. Therefore, the light collected by the CCD was due to the extraordinary optical transmission (EOT) effect.³² The transmission was calculated as follows:

$$Transmittance = 100 \times \frac{slit - dark}{ref. - dark}$$

Sample Characterization

A scanning electron microscope (SEM) with focused ion beam (FIB) capability (Auriga Dual Beam FIB/SEM, Carl Zeiss) was used to mill the nanostructures as well as image the fluidic dam microstructure and milled nanostructures. In order to corroborate the dimensions of each nanoledge array and reference box both SEM and FIB imaging was used. SEM images were captured with a secondary electron detector while using a 7 kV acceleration voltage and a 4.7 mm working distance. FIB imaging gave better contrast between the milled gold ledge and the SiO₂ planar top. This allowed for ease of visualization with the 280 nm wide ledge. A step profilometer (KLA Tencor, P-10) was also used to give insight into the microstructures, particularly the fluidic dam.

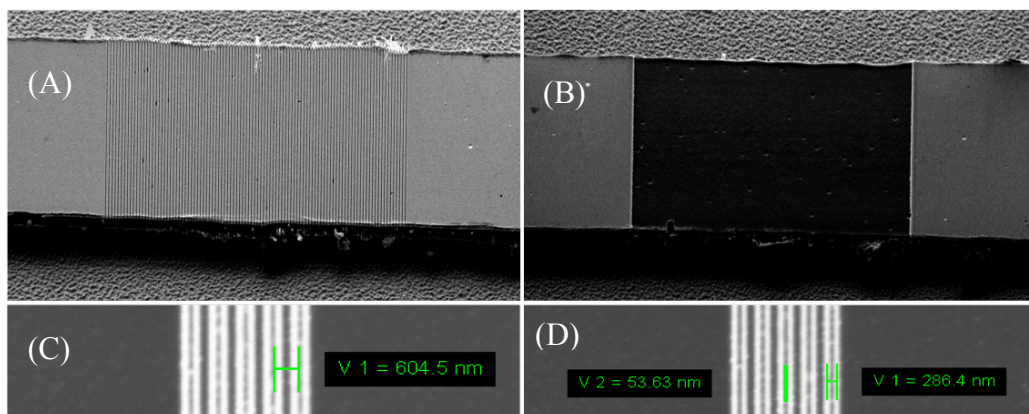


Figure 5.8. Scanning Electron Microscope (SEM) Images of a Flow-over Dam with Milled (A) Nanoedge Array and (B) Reference Box. Focused Ion Beam (FIB) Images of Milled Nanoedges Showing the (C) Periodicity, Which is the Center-to-center Spacing (604.5 nm) and (D) the Dimensions of the Nanoedge Slit (53.63 nm) and Outer Ledge (286.4 nm).

Results

Confocal Analysis of the Fluidic Dam

One of the primary objects in this work was to design and fabrication a device that could have real world utility. Using samples such as whole blood without any sample pretreatment would be ideal for point-of-care sensors in the field. The problems that arise when using whole blood samples are related to the viscosity, turbidity, and stickiness of samples with large red blood cells. Blood cells further add to the potential for non-specific binding. To embark on this issue, we have designed a flow-over, fluidic dam that could potentially size discriminate the large blood cells from the protein biomarkers of interest. As a first step and to mimic red blood cells, we have chosen to follow the paths of fluorescent polystyrene microspheres (Polysciences', Fluoresbrite) through their journey over the fluidic dam and through the fluidic channel. These microspheres were

close in size to a red blood cell and were a first step approximation of how red blood cells may behave in whole blood samples. The microspheres were used to study the flow and potential hang up under and near the sidewalls of the flow-over dam. The microspheres were 1.00 μm in size and contained fluorescein dye, which gave an emission at 486 nm. The microspheres were diluted to 0.25% aqueous suspension and passed through sealed fluidic chips by means of a syringe pump at a flow rate of 300 $\mu\text{L}/\text{min}$. Fluidic dams with an undercut sidewall profile (Figure 5.9) were shown to capture and retain the microspheres while dams with an overcut sidewall profile did not.

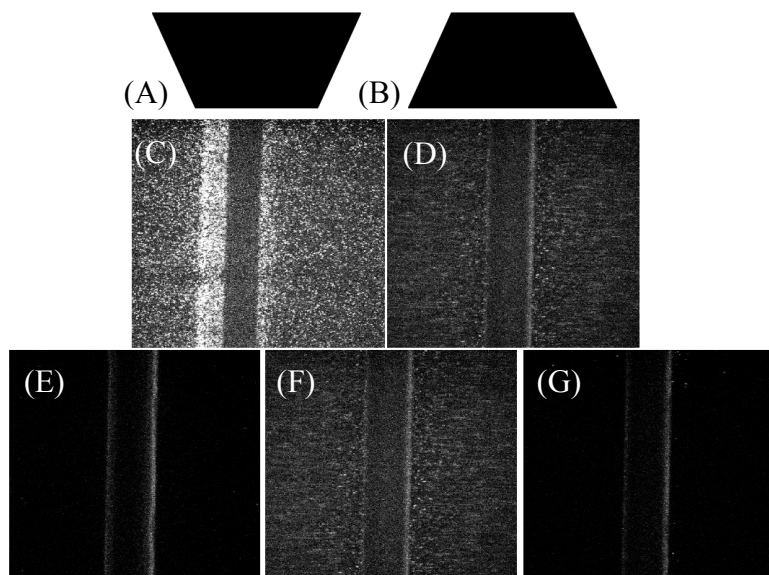


Figure 5.9. A Cross-section View of a Drawing of a Fluidic, Flow-over Dam with an (A) Undercut Profile and a (B) Overcut Profile. Confocal Microscopy Analysis of Polystyrene Microspheres Passing over the Flow-over Dam. The Images are Shown Top-Down (Not in Cross-section). Fluorescent Microspheres Shown (C) Hanging up at a Dam with Undercut Sidewalls and (D) Shown Passing over a Dam with Overcut Sidewalls. Using a Flow-over Dam with Overcut Sidewalls One Can See the Dam (E) before Entry of the Microspheres, (F) during Flow of the Microspheres, and Then (G) Completely Rinse Away by Flow of DI Water, Showing No Microspheres Adhered to the Sidewalls of the Dam.

tSPR Measurements

In order to detect the binding of troponin T the sensor must first be functionalized with a selective ligand that binds only the target analyte. A ligand with high selectivity is needed in order to avoid non-specific binding. Troponin was used as the protein free in the running solution while a self-assembled monolayer and DNA aptamer was functionalized to the chip surface.

Before the addition of any self-assembled monolayer or DNA aptamers to the surface, tSPR measurements were taken in air to gain insight into the resonant peak locations. As shown in optical transmission spectra in Figure 5.10, the primary resonant peak locations are as follows: 744, 809, and 970 nm. The light source was placed underneath the substrate and shone directly onto the underside of the dam, which contained the nanoledge structures. After attachment of the self-assembled monolayers and the DNA aptamer there was a red shift to longer wavelengths. The binding of the troponin T protein to the DNA aptamer resulted in a further red shift. The shift is governed by the following equation:²³

$$\Delta\lambda_{SPR} = S(n_{troponin} - n_{air})[1 - e^{(-2T_{troponin}/l_d)}]$$

$\Delta\lambda_{SPR}$ represents the resonant peak shift in nm, S is the sensitivity in nm/RIU, $n_{troponin}$ is the refractive index of troponin (a value of 1.45 is common for most proteins), n_{air} is the refractive index of air (1.00), T_{ligand} is the thickness of the organic layer that is attached to the surface (SAM and DNA aptamer), $T_{troponin}$ is the thickness of the binding element

(troponin protein in this case), l_d is the length of decay of the surface plasmon wave into the dielectric layer at the nanoledge array. A value of 30 nm is often used,²⁴ but with nanoledge arrays 110 nm is the decay length.²⁵ Our group's previous work with nanoledge arrays has shown sensitivity values of 576 nm/RIU.²⁵

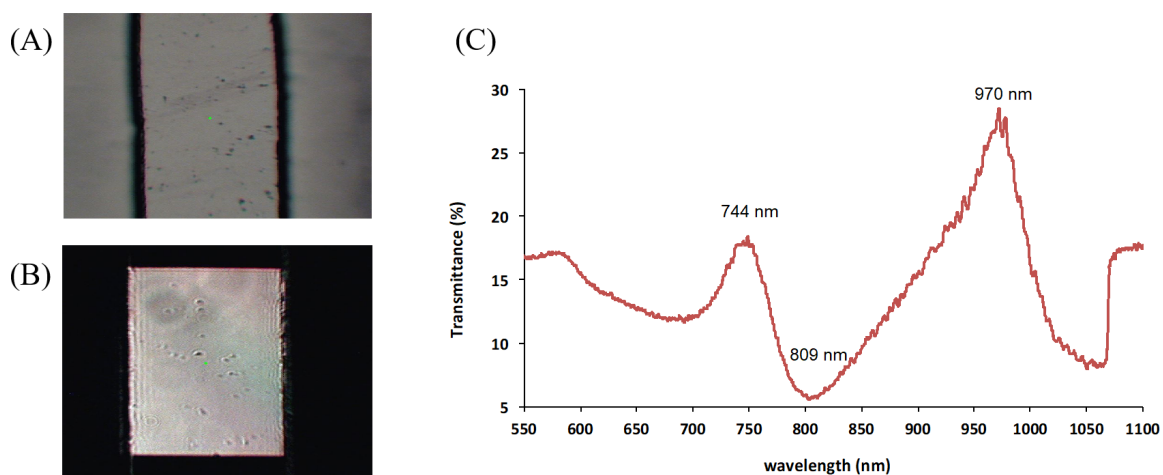


Figure 5.10. (A) A Reflection Optical Microscope Image of a Flow-over Fluidic Dam. (B) A Transmission Optical Microscope Image of a Flow-over Fluidic Dam with Milled Aperture. (C) Optical Transmission through a Flow-over Dam with Milled Nanoledge Structures Showing Primary Resonant Peaks at 744, 809, and 970 nm.

Solutions of increasing troponin T content were made and studied with tSPR. Solutions of troponin were made in Tris buffer, passed over the surface via a syringe, allowed to bond for 15 minutes, the unbound molecules rinsed away, the solution was forced out of the channel with a syringe. At this point the substrate was very gently blown with a N₂ stream and then the substrate was allowed to dry. At this point the tSPR measurement was taken. As expected, the increasing troponin concentration gave a larger peak shift. As shown in Figure 5.11, the starting point for the peak shifts was at 0 ng/mL

(no troponin in the solution). From here a peak shift of 2.11 nm was observed for the low concentration of 1 ng/mL of troponin T. The second concentration of troponin T was 10 ng/mL. This solution yielded a peak shift of 5.32 nm. Finally, the third concentration of troponin was 100 ng/mL. This yielded a peak shift of 7.37 nm from the 0 ng/mL concentration.

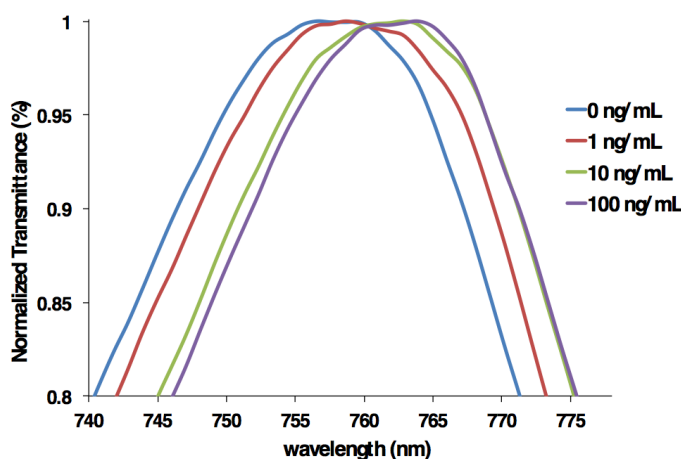


Figure 5.11. Optical Transmission Spectrum through a Nanoledge Array Showing Peak Shifts to Longer Wavelengths with Increasing Concentration of Troponin T Protein.

The dependency of peak wavelength shifts on the protein (troponin T) concentration is displayed in Figure 5.12. Three experiments were performed at each concentration and the values averaged. As the sensor is exposed to more troponin, more binding occurs. This increase in protein at the surface yields a peak shift due to the increase in dielectric constant. The data was fit with a logarithmic function. Figure 5.12A has linear concentration axis (x-axis) while Figure 5.12B has a logarithmic concentration axis. Both were fit with a logarithmic function and had a R^2 value of 0.98405.

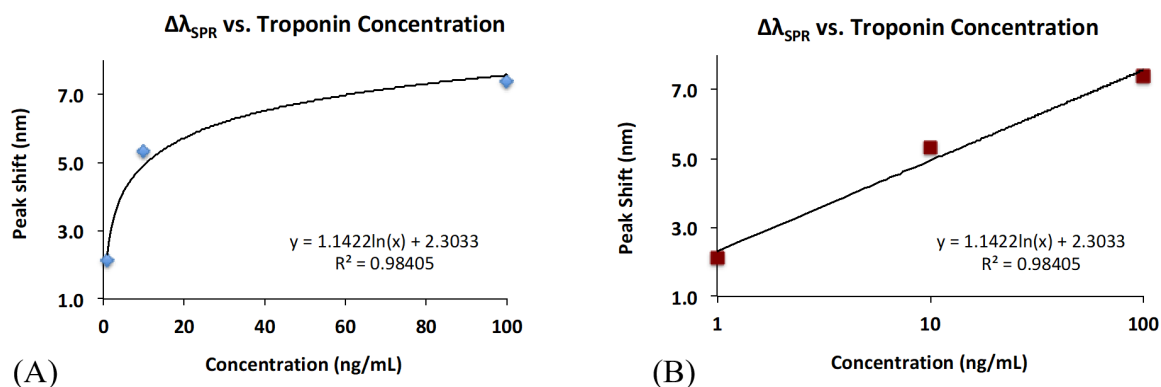


Figure 5.12. The Dependence of the Peak Wavelength Shift ($\Delta\lambda_{\text{SPR}}$) on the Concentration of Troponin T Protein is a Logarithmic Relationship. (A) A Graph with a Linear x-axis and a (B) Graph with a Logarithmic x-axis.

Control experiments were performed to ensure that the binding was in fact between the DNA aptamer and troponin T. To investigate this matter, a second protein was needed. Interleukin 6 (IL-6) has a molecular weight of 23,718 daltons while troponin T has a molecular weight of 35,760 daltons. IL-6 contains 185 amino acid residues while troponin has 298 residues. The availability of and similarity in size to troponin T is the reason why IL-6 was chosen for the control experiments. The sensor surface remained exactly the same. Cystamine and glutaraldehyde self-assembly chemistry was used followed by attachment of the same DNA aptamer (with binding specific towards troponin T). This DNA aptamer should only show binding towards troponin T and not towards other protein molecules. Figure 5.13 shows that this is indeed the case. A solution of 0 ng/mL of IL-6 was introduced and then tSPR measurement taken. This was repeated two more times. This gave a primary resonant peak at 756.53 nm. Then a high concentration (1000 ng/mL) solution of IL-6 was syringed into the channel and tSPR

measurement taken. This was also repeated two more times for a total of three measurements. The resonant peak did shift but only very slightly. The peak location was 757.38 giving a peak shift of 0.85 nm with a very high concentration of IL-6 protein.

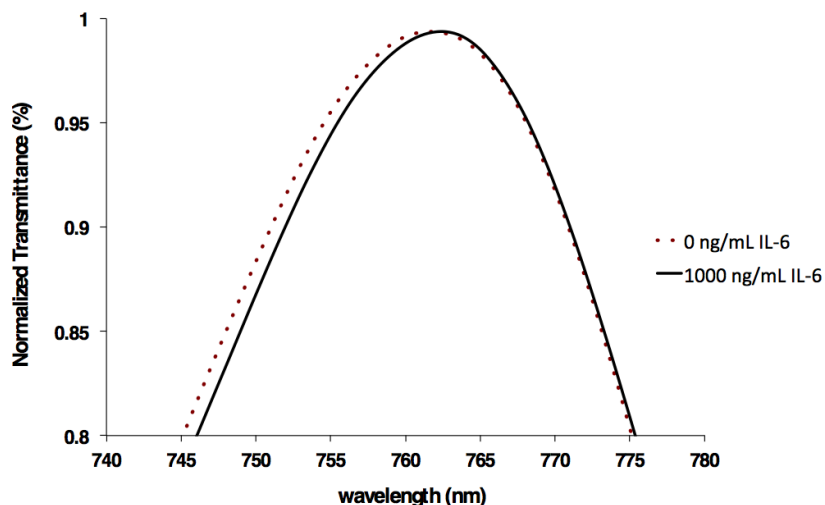


Figure 5.13. Optical Transmission Spectrum through a Nanoledge Array Showing Little to No Peak Shift with Interleukin-6 (IL-6) Protein in the Running Solution. This Experiment with Troponin T DNA Aptamer Bound to the Sensor Surface and IL-6 in the Running Solution was Performed as a Control Experiment.

Conclusion

A metal/SiO₂ film, atop a flow-over dam, with nanoledge arrays was investigated as a transmission SPR biosensor, utilizing the phenomena of extraordinary optical transmission. A flow-over fluidic dam was fabricated using a multi-layered resist (MLR) method. Micron sized fluorescent beads were shown to hang up on dams with undercut sidewalls and flow over top of dams with overcut sidewalls. FIB milling on top of the SiO₂ capped dam became problematic with charging and drifting. This was solved with a

wrap of metallic foil around the chip before nanostructuring and afforded the ability to skip sputter coating and eventually being required to remove the coating before optical measurements. Arrays of nanoledge structures were used in the detection of Troponin T, one of the biomarkers for acute myocardial infarction (MI). SAM chemistry and DNA aptamers were used to functionalize the sensor surface. Troponin T protein bound to the DNA aptamer to give resonant peak shifts to longer wavelengths. A logarithmic relationship was found between increasing troponin concentration and the peak wavelength shift. A red shift of the resonant peak was observed as the refractive index increased at the sensor surface.

References

1. Heart Disease Facts & Statistics | cdc.gov. (2017). Retrieved October 4, 2018, from <https://www.cdc.gov/heartdisease/facts.htm>
2. Mozaffarian D, Benjamin EJ, Go AS, et al. Heart disease and stroke statistics—2015 update: a report from the American Heart Association. *Circulation*. 2015;131:e29-322.
3. Cotterill, P. G., Deb, P., Shrank, W. H., & Pines, J. M. (2015). Variation in Chest Pain Emergency Department Admission Rates and Acute Myocardial Infarction and Death Within 30 Days in the Medicare Population. <https://doi.org/10.1111/acem.12728>
4. Yau, A. A., Nguyendo, L. T., Lockett, L. L., & Michaud, E. (2017). The HEART Pathway and Hospital Cost Savings. *Critical Pathways in Cardiology*, 16(4), 126. <https://doi.org/10.1097/HPC.0000000000000124>
5. EMS STEMI Evidence Based Measures - Emergency Medical Services - County of Santa Clara. (n.d.). Retrieved October 4, 2018, from <https://www.sccgov.org/sites/ems/services/qi/Pages/EMSCQISTEMI.aspx>
6. Johnston, S., Brightwell, R., & Ziman, M. (2006). Paramedics and pre-hospital management of acute myocardial infarction: diagnosis and reperfusion. *Emerg Med J*, 23, 331–334. <https://doi.org/10.1136/emj.2005.028118>
7. Liu, C. H., & Huang, Y. C. (2011). Comparison of STEMI and NSTEMI patients in the emergency department. *Journal of Acute Medicine*, 1(1), 1–4. <https://doi.org/10.1016/J.JACME.2011.08.001>
8. Richard N. Fogoros. (2018). NSTEMI: Non-ST-Segment Myocardial Infarction Explained. Retrieved October 4, 2018, from <https://www.verywellhealth.com/non-st-segment-elevation-myocardial-infarction-nstemi-1746017>
9. Dittrich, P. S., & Manz, A. (2006). Lab-on-a-chip: microfluidics in drug discovery. *Nature Reviews Drug Discovery*, 5(3), 210–218. <https://doi.org/10.1038/nrd1985>
10. Olaru, A., Bala, C., Jaffrezic-Renault, N., & Aboul-Enein, H. Y. (2015). Surface Plasmon Resonance (SPR) Biosensors in Pharmaceutical Analysis. *Critical Reviews*

in *Analytical Chemistry*, 45(2), 97–105.
<https://doi.org/10.1080/10408347.2014.881250>

11. Akimoto, T., Sasaki, S., Ikebukuro, K., & Karube, I. (1999). Refractive-index and thickness sensitivity in surface plasmon resonance spectroscopy. *Applied Optics*, 38(19), 4058. <https://doi.org/10.1364/AO.38.004058>
12. Willets, K. A., & Van Duyne, R. P. (2007). Localized Surface Plasmon Resonance Spectroscopy and Sensing. *Annual Review of Physical Chemistry*, 58(1), 267–297. <https://doi.org/10.1146/annurev.physchem.58.032806.104607>
13. Arai, T., Kumar, P. K. R., Rockstuhl, C., Awazu, K., & Tominaga, J. (2007). An optical biosensor based on localized surface plasmon resonance of silver nanostructured films. *Journal of Optics A: Pure and Applied Optics*, 9(7), 699–703. <https://doi.org/10.1088/1464-4258/9/7/022>
14. Rodríguez-Lorenzo, L., Romo-Herrera, J. M., Pérez-Juste, J., Alvarez-Puebla, R. A., & Liz-Marzán, L. M. (2011). Reshaping and LSPR tuning of Au nanostars in the presence of CTAB. *Journal of Materials Chemistry*, 21(31), 11544. <https://doi.org/10.1039/c1jm10603a>
15. Liu, H., & Lalanne, P. (2008). Microscopic theory of the extraordinary optical transmission. *Nature*, 452(7188), 728–731. <https://doi.org/10.1038/nature06762>
16. Gay, G., Alloschery, O., Viaris de Lesegno, B., O'Dwyer, C., Weiner, J., & Lezec, H. J. (2006). The optical response of nanostructured surfaces and the composite diffracted evanescent wave model. *Nature Physics*, 2(4), 262–267. <https://doi.org/10.1038/nphys264>
17. Z. Zeng, M. N. Mendis, D. H. Waldeck, J. Wei, *RSC Adv.* **2016**, 6, 17196-17203.
18. Bruno, J. (2011). Methods and compositions of nucleic acid ligands for detection of clinical analytes related to human health. Retrieved from <https://patents.google.com/patent/US20120135540>
19. J. Benesch, J. F. Mano, R. L. Reis, *Acta. Biomater.* **2010**, 6, 3499-3505.
20. a) H. Ron, S. Matlis, I. Rubinstein, *Langmuir* **1998**, 14, 1116-1121; b) C. G. Worley, R. W. Linton, *Journal of Vacuum Science & Technology A: Vacuum, Surfaces, and Films* **1995**, 13, 2281-2284.
21. D. Berman, J. Krim, *Thin Solid Films* **2012**, 520, 6201-6206.

22. J. Kang, P. A. Rowntree, *Langmuir* **2007**, *23*, 509-516.
23. Wei, Jianjun & Kofke, Matthew & Singhal, Sameer & H Waldeck, David. *JSM Nanotechnology & Nanomedicine* **2014** *2*. 1024.
24. Jung YS, Sun Z, Wuenschell J, Kim HK, Kaur P, Wang L, et al. High-sensitivity surface plasmon resonance spectroscopy based on a metal nanoslit array. *Applied Physics Letters* 2006;*88*:243105-3.
25. Zheng Zeng, Xiaojun Shi, Taylor Mabe, Shaun Christie, Grant Gilmore, Adam W. Smith, and Jianjun Wei. *Analytical Chemistry* **2017** *89* (10), 5221-5229

CHAPTER VI

FABRICATION OF A PLASMONIC PHOTOCURRENT DEVICE

Zheng Zeng, **Taylor Mabe**, Wendi Zhang, Bhawna Bagra, Zuowei Ji, Ziyu Yin, Kokougan Allado, Jianjun Wei. "Plasmon-exciton coupling in photosystem I based biohybrid photoelectrochemical cells." *ACS Applied Bio Materials*. **2018**.

Overview

The light-induced property of photosystem I (PSI) has been utilized to convert solar energy to electrical energy in photoelectrochemical cells. Here we provide new results on the relationship between surface plasmon generation (SPG) efficiency of nanoslits and the experimentally obtained photocurrent by immobilizing PSI on the gold nanoslit electrode surfaces regarding different nanoslit widths. The photocurrent increases with the increment of SPG efficiency. This finding can be attributed to the phenomenon of plasmon-exciton coupling effect on the PSI in the nanoslits. The enhancement of photocurrent generation is discussed on the basis of plasmonic light trapping and plasmon-induced resonance energy transfer.

KEYWORDS: photosystem I, surface plasmon resonance, plasmon-exciton coupling, photocurrent, photoelectrochemistry

Introduction

Because of the photoelectric effect firstly discovered in 1839, photosystem I (PSI, ~500 kDa protein super-complex) has been widely used to efficiently capture sunlight for

achieving efficient biohybrid photo-energy conversion devices.¹⁻³ In the photosynthesis process, photoexcited electrons are transported at a 1 μ s time scale across the thylakoid membrane by using PSI as a photodiode at a quantum efficiency closing to 100%.⁴⁻⁵ Within PSI, though an internal electron-transfer chain including chlorophylls, phylloquinones, and iron-sulfur cluster, the electron-transfer happens between the photoexciting P700 reaction center and iron-sulfur clusters terminating at the F_B cluster.⁶⁻

⁷ Based on the rapid electron transfer and high energy conversion efficiency of PSI, Greenbaum firstly photoreduced platinum upon the chloroplast's surface by using the reducing power of PSI.⁸ And then Gerster successfully measured the photocurrent using a single PSI and obtained a photocurrent of 10 pA by a near-field scanning optical microscopy.⁹ By electrochemically integrating an electrode with PSI, Baldo developed a photovoltaic device (solid-state) by employing PSI as the active species.¹⁰ Based on molecular wires on the gold electrode, a current density was obtained to be 88 nA/cm², achieving an enhancement factor of 2.2 over that of the earlier reported system.¹¹⁻¹² Moreover, the electrode with a nanostructured gold layer has been conducted to act as a positive factor by increasing the photocurrent of PSI.¹³⁻¹⁴ Over the past decade, to improve biohybrid devices, many researches have been conducted to electrochemically integrate an electrode with PSI via creating covalent attachments,¹⁵ increasing surface area,¹⁶ improving cell design,¹⁷ increasing film thickness,¹⁸ and applying semiconducting electrode,¹⁹ etc.

Conforming to these reports, light-harvesting enhancement has been considered to be one of the critical factors to design a biohybrid photoelectrochemical cell.²⁰ To improve the coupling efficiency of plasmonic resonance and active species in biomaterial based systems, the strategies based on the plasmon-induced resonance energy transfer (PIRET)²¹⁻²² and metal particle-enhanced light emission have been developed.²³⁻²⁴ Recently, to increase the light absorption and photocurrent generation of PSI, surface plasmon enhancement related coupling of plasmonic resonance and active species was used focusing on the localized surface plasmon resonance (LSPR) by improving the photoactivity of PSI with the gold nanoparticles due to confined collective electronic oscillations.²⁵⁻²⁹ This is because that the properties of PSI could be tuned by the enhanced fields derived from the spatially confined LSPR corresponding to the optical excitation at/near the resonant energies. Generally, LSPR and surface plasmon polariton (SPP) are two distinct forms of surface plasmon resonance. According to the origin of SPP, visible or near-infrared frequency electromagnetic waves occur at the interface of metal-dielectric materials.³⁰⁻³¹ To date, rare reports focus on the SPP effect on PSI and the metallic nanostructure in combination with PSI for implementation of its photoelectric functionality at the nanoscale, especially the fundamental relationship between the photocurrent generation and the surface plasmon generation (SPG) efficiency. Here the SPG efficiency is a term used to quantitatively describe how the surface waves scatter, launch, and propagate at the nanostructure interface by matching the continuous electromagnetic field quantities.³⁰⁻³¹

In this work, we used a nanoslit design for an electrochemical setup and, for the first time, observed the photocurrent generation of PSI proteins in a nanoscale plasmonic structure. The PSI was extracted from spinach (Figure C1, Appendix C) with featured absorbance peaks at both 435 and 670 nm (Figure C2)³² The PSI proteins were immobilized at a nanoplasmonic electrochemical device for photocurrent measurements with light excitation. Each device was milled to have one slit of the width at 50 nm, 100 nm, 200 nm, 300 nm, or 400 nm at the bridge center (Figures C3-C6). The present work considered using a semi-analytical SPG model and numerical simulations to demonstrate that the nanoslit width can induce changes in the photocurrent generation from the PSI proteins due to different SPG efficiencies. The results may offer new information to study the photovoltaic enhancement of PSI and give hints to develop an artificial light-harvesting device.

Materials and Methods

PSI Preparation

Spinach leaves were purchased from a supermarket and used for the PSI extraction and purification. The steps of the extraction of thylakoid membranes from the spinach leaves and the isolation and purification of PSI complexes from the thylakoids via the methods of Ciesielski.⁶

Fabrication of Nanoplasmonic Electrochemical Devices

We used AutoCAD to draw the sketch of a dark-field photomask and then used a high-resolution printer (25400 DPI) to print it on the transparency film. The design of the

photomask is shown in Figure C3. Glass slides (Globe diamond white) were used as substrates and were cleaned in a piranha bath (3:1 H₂SO₄/H₂O₂), rinsed with DI water, dried with a nitrogen stream, and cleaned in an oxygen plasma (200 W, 2 min). After that, we used the hot plate to dehydrate the substrates at 180 °C. A negative photoresist (JSR NFR 016 D2) was spin applied to the glass slides to a thickness of 3.5 μm, exposed, and developed. In contrast to the supplied data sheet, a substrate-priming step was omitted and an O₂ plasma descum was added. Microscopy images and profilometry plots were obtained after each process step. Metal deposition was performed by evaporation (Kurt Lesker PVD75 e-beam evaporator). After reaching a base pressure of 1.0 x 10⁻⁶ Torr, Ti was evaporated at a rate of 0.5 Å/s to a thickness of 4.6 nm, Au was evaporated at a rate of 4.4 Å/s to a thickness of 226.3 nm, then Ti was evaporated at a rate of 0.4 Å/s to a thickness of 4.4 nm. SiO₂ was used as a capping layer and 100.1 nm was deposited atop the final Ti layer at a rate of 1.5 Å/s. We used the acetone bath to sonicate for the lift-off process. A positive photoresist (Shipley S1827) was spin coated onto the patterned substrate and exposed through the second photomask. The top oxide layer was dry etched with reactive ion etching (LAM Rainbow 4400) using a mixture of CF₄/O₂. The positive photoresist was stripped and a nanoslit was milled in the center of each substrate with focused ion beam milling (Zeiss Auriga). Each device was milled to have one slit (with a slit width of 50 nm, 100 nm, 200 nm, 300 nm, or 400 nm) at the bridge center (Figures C4-C5).

Immobilization of PSI on Gold Nanoslit Surfaces

The method for protein immobilization has been reported in detail previously.³³ In brief, O₂ plasma (South Bay Technologies PC2000 Plasma Cleaner) was used to clean the gold slide electrode for three minutes. A mixed self-assembled monolayer (SAM) of 11-mercaptoundecanoic acid (Sigma Aldrich) and 8-mercapto-octanol (Sigma Aldrich) was formed by incubating in an absolute ethanol solution (ACROS Organics) containing a 1:2 mole ratio of the two alkanethiols for 2 days. The SAM was activated by a 10 mM PBS solution with 0.5 mM EDC/NHS (Sigma Aldrich) for 2 hours. After rinsing with a 10 mM PBS solution, the PSI was immobilized to the gold surfaces via incubating in a 10 mM PBS solution with ~1 mM PSI for 2 hours.

Electrochemical Measurement

Chronoamperometry (CA) photocurrent measurements were conducted using an electrochemical workstation (Bio-logic VMP3) with both sides of the gold slide as a testing system under a 0.2 V applied voltage in a homemade Faraday cage by the aluminum foil. Figure C6 shows the electrochemical device slide. A bridge center was fully covered by the electrolyte solution containing 20 mM methylene blue (MB) redox-active mediator with 100 mM KCl in 10 mM PBS solution. We then used the copper tape piece to electrically connect either side of the electrode. The photo-induced measurement was carried out using the LS-1 white light source with a tungsten halogen lamp (Ocean Optics Inc.) connected with an optical fiber and the area for the nanoslit region was fully illuminated by the light source. Note that the external conditions include the light

excitation (without/with light) for different testing systems (SAM/gold slide without PSI immobilization and SAM/gold slide with PSI immobilization).

Semi-analytical Analysis

With a semi-analytical model,³⁰⁻³¹ the SPG efficiency, e , at the Au-glass interface of the nanoslit can be calculated as follows:

$$e = \left| \alpha^+ (w/2) \right|^2 = \left| \alpha^- (w/2) \right|^2 = \frac{4w'n_1^3}{\pi n_2^2} \left| \frac{\epsilon^{1/2}}{\epsilon + n_1^2} \right| \left| \frac{I_1}{1 + (n_1/n_2)w'I_0} \right|^2, \quad (\text{Eq. 1})$$

which correlates to the SPG coefficient (α), nanoslit width (w), scaled width (w'), refractive index (n), dielectric constant (ϵ), and integration number (I) (see details in Appendix C).

Finite-Difference Time-Domain (FDTD) Simulations

The electric or magnetic field intensity profiles of the nanoslit were calculated by a Lumerical FDTD method.^{31,34} Considering the background of air, the refractive index was assumed to be 1.0 in the total mesh area. Perfectly matched layer (PML) was applied for the boundary conditions. The indices of Au and glass were obtained from the data of optical constants of solids. Electric-magnetic field distribution calculations were performed at different slit width. Using the Drude-Lorentz model, the transverse electric/magnetic (TE/TM) equations were obtained by a Fourier transform of the polarization.³⁵

Results and Discussion

We firstly study the photoelectric response of immobilized PSI on the gold slide electrodes through the mixed SAM (Figure 6.1). This strategy of covalent binding to the protein's amino groups for immobilization may decrease PSI large-conformational motion.^{3, 36} The action spectrum of the PSI immobilized inside the nanoslit surfaces (Figure C7) was obtained by measuring the photocurrent in a 20 mM MB redox-active mediator (with -0.2 V vs. Ag/AgCl formal potential) associated with 100 mM KCl in 10 mM PBS under light irradiation using the LS-1 white light source. Similar to the relaxation pathways occur in the interface of a semiconductor and an electrolyte, electron-hole pairs (e^-h^+) can undertake different pathways, which include electron transfer to redox species, electron transfer to the substrate, and electron-hole pair radiative recombination.³⁷⁻³⁸

In this case, under light illumination of the PSI, an oxidized $P700^+$ donor site and a reduced F_B acceptor can be generated by the photon-induced electron-hole pairs separation. Consequently, a direct electron transfer would occur according to the following details. After photoexciting $P700$ center, the F_B end will accept an electron from the photoexcited $P700$ center and then transfer it to the gold electrode through an internal electron-transfer chain. Gold electrode is an electron acceptor compatible with the F_B cluster in PSI, leading to an increased electrode current. Meanwhile, before another photon can re-excite $P700$ center in the PSI, the oxidized $P700^+$ center must be reduced by re-accepting a new electron. In our system, the MB in solution acts as

electron donors to the oxidized P700⁺ center (Figure 6.2a). Atomic coordinates from PDB entry 2O01 are used to make the structure of PSI.³⁹

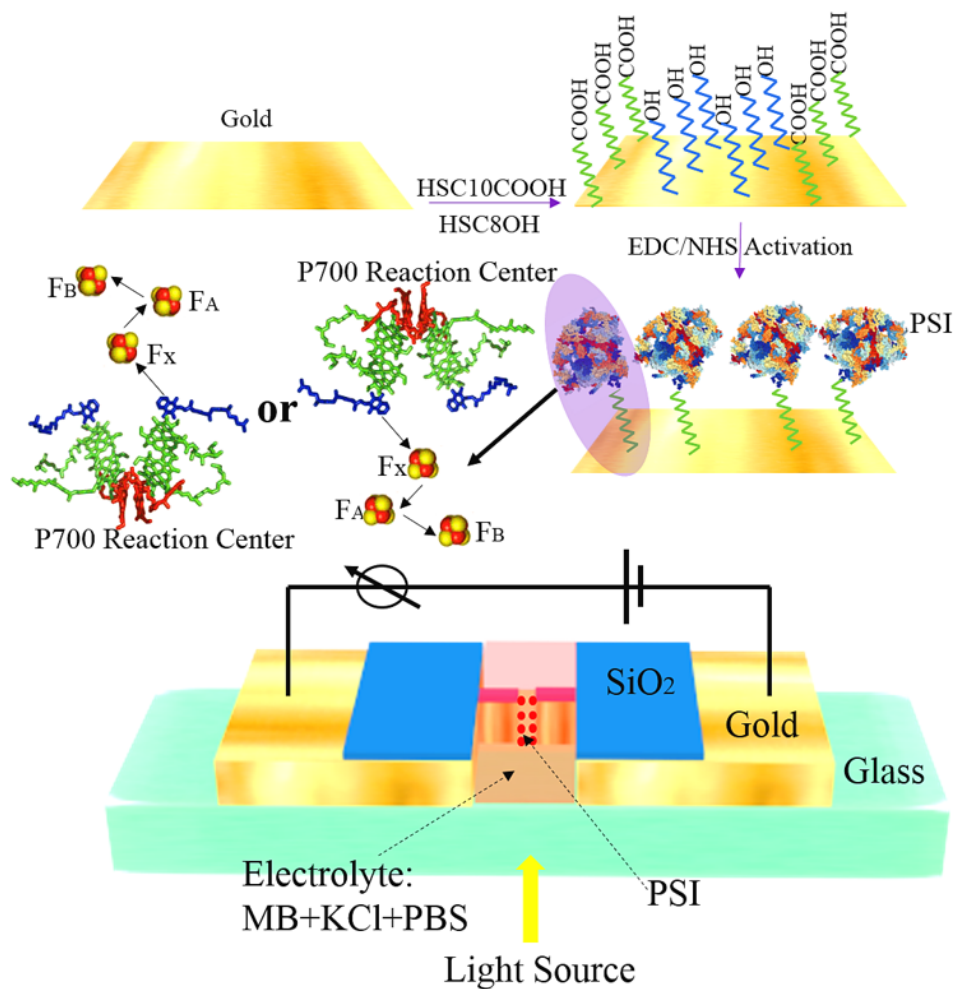


Figure 6.1. A Schematic View of a Method for the PSI Immobilization with a SAM and a Setup for the Light Associated Electrochemistry Analysis of PSI.

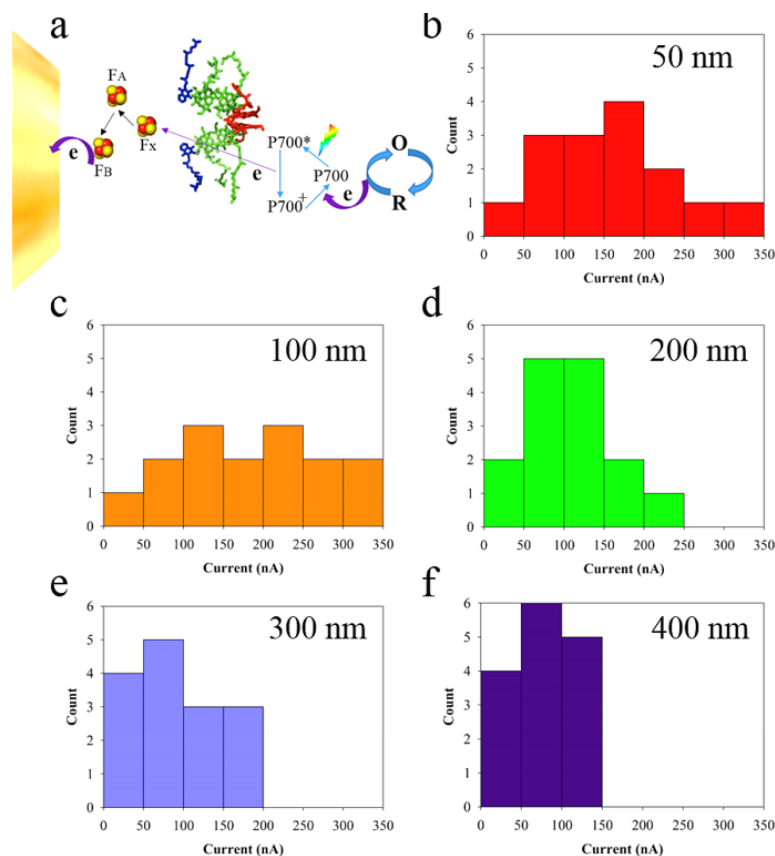


Figure 6.2. (a) Illustration of the Electron Transfer from PSI to Au Slide Electrode with the Reaction-center Electron Transfer Chain. (b-f) Photocurrent Generation Analysis and Histograms for the Electrochemical Devices with Different Nanoslit Widths.

Figure 6.2b-f show histogram distribution of photocurrent generation by the immobilized PSI at an applied voltage of 0.2 V in nanoslits. Figures C7-C8 show the representative CA measurements of nanoslit electrodes with or without immobilized PSI, respectively. In the CA measurements, the potential of the working electrode is stepped and recorded after 10 seconds of waiting time from the initial to the steady-state current. The photocurrent was recorded as a function of time from the photoexciting processes occurring at the side of nanoslit. The highest photocurrent (avg. ~181 nA by a 100 nm

nanoslit width device) and the lowest (avg.~76 nA by a 400 nm nanoslit width device) were obtained. Since the untreated gold nanoslits for all different widths have no obvious photocurrent generation under the light irradiation, we conclude that the photocurrent is originated from the PSI immobilized at the gold electrode surfaces due to the photoelectric effect. In accordance with a reported PSII-based photoelectrochemical cell,⁴⁰ the current-voltage curve (Figure C9) of the electrochemical cell with PSI immobilization (using nanoslit width of 100 nm) also supports the photoactive role of PSI in photocurrent generation. Considering that PSI proteins should have either the acceptor side (F_B) or the donor side (P700) in contact with the SAM-gold electrode to undergo a redox reaction,^{3, 7} the average value of the net photocurrent was obtained from 15 measurements (chosen from 18 measurements including 2 nanoslit devices with the same nanoslit width × self-assembly performed on the same device 3 times × measurements 3 times) for each nanoslit width device (Table C1). Note that 3 trials were failed (no photocurrent measured) possibly because of the release of chlorophyll or denature of PSI with the light irradiation. Using the excitation area of gold electrode about 18.2 μm² (fabrication information) with immobilized PSI, in our nanoscale device, the current density could be roughly obtained to be about 9.95 nA/μm² for the 100 nm width nanoslit device. Considering that, in the centimeter-scale biohybrid photoelectrochemical cells, the photocurrent generation of PSI films on p-doped silicon can be obtained to be about 875 μA/cm²,¹⁹ our results may suggest the good integration of photocurrent magnitude of 10 pA created by a single PSI using such a nanoscale energy conversion device.⁹

Next, we move to study the relationship of SPG efficiencies with the nanoslit width and incident light wavelengths. Regarding the bounded SPP modes with the geometric diffraction presenting on the interface of a gold surface and a glass one, the SPP scattering coefficients and efficiencies at the slit apertures are calculated. The scheme in Figure 6.3a depicts the key parameters for the SPG calculation with respect to the geometry of the nanoslit and property of light source (a normally incident plane wave), including the slit width of w , the SPG coefficients at the Au-glass interface in an inverse direction (α^+ and α^-), the refractive index of glass (n_{glass} of 1.41) and inside the slits (n_{air} of 1). The SPG efficiency on one side of the aperture was obtained using Eq. 1 presented earlier.

After a numerical calculation by a Python script (Table C2) and an analytical technique, for one side of the nanoslit structure, the SPG efficiency e can be obtained.³⁴ As shown in Figure 6.3b, with the increase of light wavelength (λ from 600 nm to 1200 nm) and scaled slit width (w' from 0.1 to 1.0), the SPG efficiencies were demonstrated dependence as a function of λ and w' . The SPG efficiency is higher in the visible frequency region than that in the near-infrared region because of the stronger visible frequency electromagnetic waves occurring at the Au-glass interface. Considering that the optimal slit width is related to the optimal scaled slit width, a value of $w'=0.26$ is obtained to estimate the optimal slit width. For example, the optimal widths are $w=0.18\lambda$ for the nanoslit with refractive index of 1.41. Moreover, according to different values for

w and λ , one can get different e values (Figure 6.3c, Table C3) and average SPG efficiencies (Table C1).

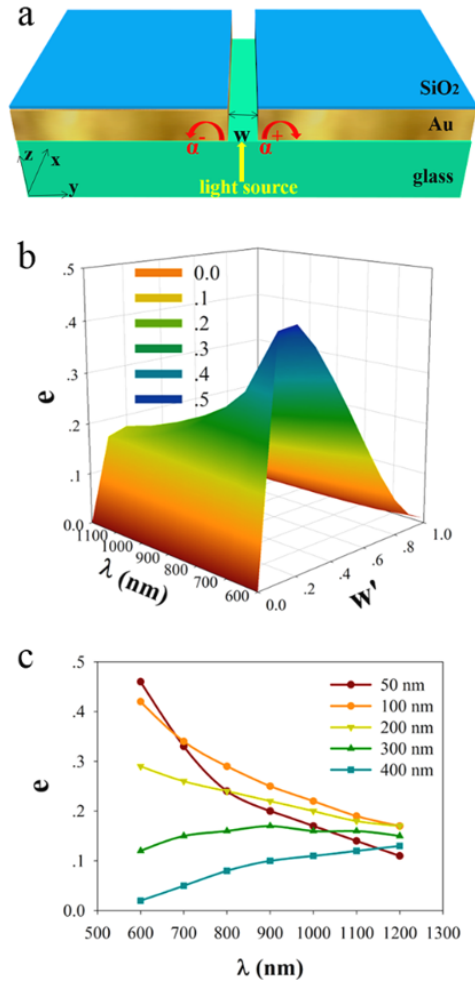


Figure 6.3. (a) Illustration of the Key Parameters for the SPG Calculation with Respect to the Structure of the Nanoslit and Light Source. (b) The Plot of SPG Efficiencies e at the Au-glass Interface with Respect to λ and w . (c) The Relationship of SPG Efficiencies e at the Au-glass Interface with λ at Different w .

The electromagnetic field distribution of the nanoslit structure (without PSI immobilization) was further modeled via a FDTD method (Figure C10). A Fourier

transform polarization was initiated and implementing it into the FDTD formalism resulted in the TE/TM equations. The electromagnetic (EM) field distribution indicates the plasmonic intensity at the Au-glass interface with the strength of $EM_{100} > EM_{50} > EM_{200} > EM_{300} > EM_{400}$, which is consistent with the results of the nanoslit structure with PSI immobilization (Figure C11). It is interesting to compare the FDTD result with PSI immobilization to that without PSI with the same nanoslit width. Adding a bio-layer on the side of nanoslit decreases the plasmonic intensity due to the increase of refractive index. Note that the refractive index and thickness of the PSI film were estimated to be 1.5 and 10 nm,⁴¹⁻⁴² respectively. The FDTD simulation agrees well with the semi-analytical model results for SPG efficiencies from the five nanoslit devices. Hence, the stronger charge oscillation induced by the improved SPP excitation results in an enhanced EM field at the Au-glass interface.⁴³⁻⁴⁴

Additionally, we used the CytoViva Hyperspectral imaging system to measure the light intensity in the nanoslit (Figure 6.4). The ENVI software was used to get the light intensity data in the center of the nanoslit by taking the image pixel by pixel. Spectra can be obtained from point to point and it gives the option to take the average spectra. We took the average spectra of each nanoslit 3 times to check the consistency and accuracy. The light intensity data is well consistent with the SPG efficiency of the electrochemical devices. More importantly, one absorbance peak wavelength of PSI (670 nm) locates within the range of light intensity peak wavelength (600-700 nm). These results suggest

that the plasmon-induced light trapping provides insight into the SPG efficiencies corresponding to the EM field distributions.

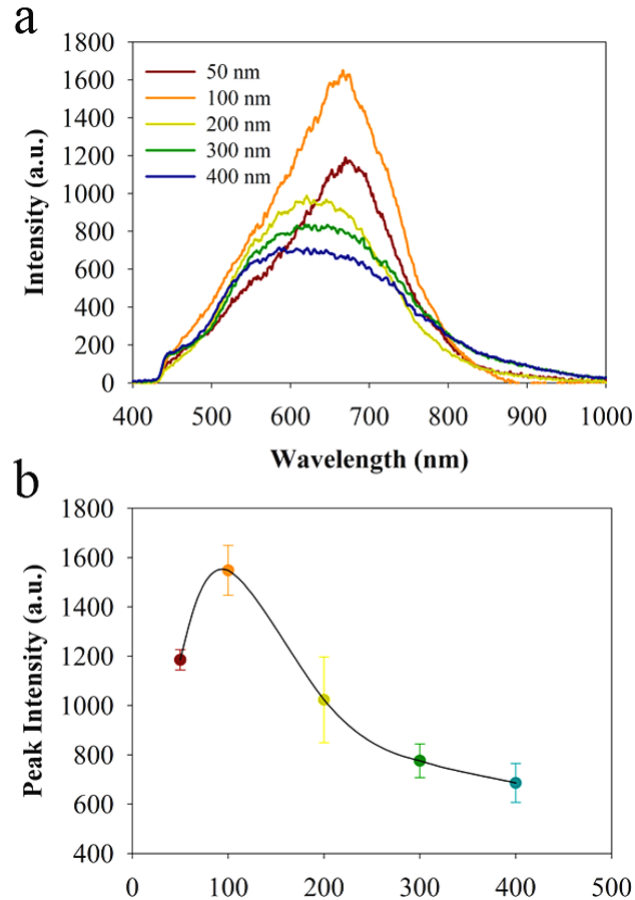


Figure 6.4. (a) Light Intensity Measurements for Different Nanoslit Structures in Reflection Mode, (b) Peak Intensity Versus Different Nanoslit Structures.

Figure 6.5 shows the photocurrent generation and SPG efficiency for the nanoslit electrochemical devices (D) as a function of nanoslit width. They both have the same order of $D_{100} > D_{50} > D_{200} > D_{300} > D_{400}$. Regarding the plasmonic effects on the metal-semiconductor photoelectrochemical cells,⁴⁵ light trapping/scattering, direct electron

transfer (hot electron injection), and PIRET have been recognized as three major mechanisms.⁴⁶ In this study, the photocurrent is originated from the electron transfer from immobilized PSI to the gold electrode, and the light intensity spectra in the nanoslits presents an overlap with the absorption peak of PSI. Hence, for this hybrid metal-biology system, it is expected that the plasmonic light trapping excitation and the PIRET between gold and PSI should play major roles in the enhanced photocurrent generation. Specifically, larger SPG efficiency (also called larger collective electron oscillations or larger electromagnetic near-field propagation) can concentrate more incident energy due to the larger combined dipole moment generation. This concentrated incident energy can be non-radiatively transferred to the PSI proteins through PIRET to generate more electron-hole pairs in PSI,⁴⁷⁻⁴⁸ resulting in more excited electrons inside the P700 center, thus more available P700⁺ donor sites and F_B acceptor sites for better efficient electron exchange in PSI. As a result, more electrons from the F_B end transfer to the gold electrode, leading to an increased photocurrent. Meanwhile, since plasmon resonance induced electron-hole separation potentially makes the kinetics of electron transfer faster, the gold electrode will receive more electrons under a unit time scale. Hence, the net photocurrent generation of the PSI is well consistent with the SPG efficiency of the electrochemical devices (Figure 6.5) with nanoslit width dependence and maximized at 100 nm slit in this work.

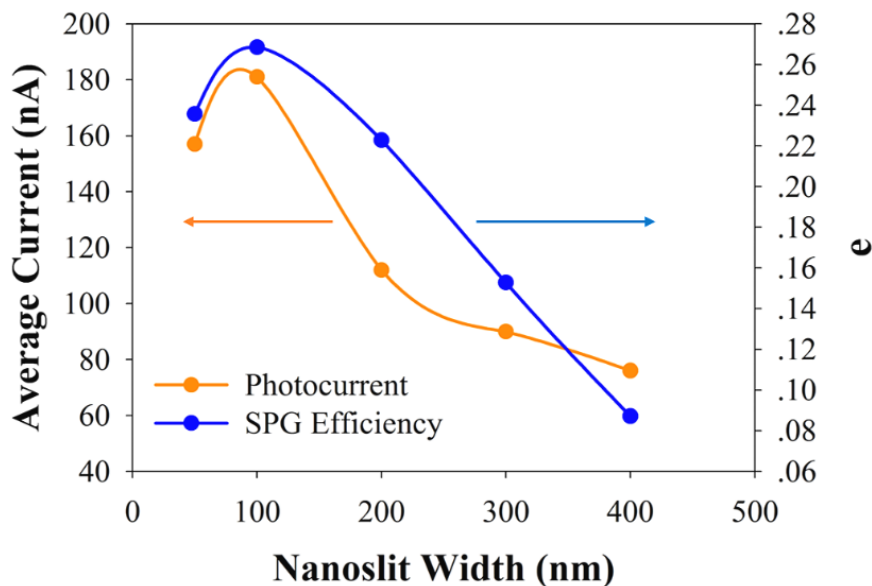


Figure 6.5. Plot of Average Photocurrent in Experimental Measurements or Calculated SPG Efficiency Versus Nanoslit Width.

Conclusions

This work demonstrates how surface plasmon resonance influence the photocurrent generation from PSI by immobilizing PSI on gold surfaces in a nanoslit. The energy conversion (photocurrent) is greatly enhanced, which is correlated to the SPG efficiency and EM field enhancement in the nanoslit. The results could be attributed to the phenomenon of plasmon-exciton coupling with the effects of plasmon-induced energy transfer and light trapping. This study offers promise to develop a novel photosystem I based biohybrid photoelectrochemical cell for high efficiency energy conversion.

References

1. Paul, S.; Neese, F.; Pantazis, D. A. Structural Models of The Biological Oxygen-Evolving Complex: Achievements, Insights, and Challenges for Biomimicry. *Green Chem.* **2017**, *19*, 2309-2325.
2. Gizzie, E. A.; LeBlanc, G.; Jennings, G. K.; Cliffel, D. E. Electrochemical Preparation of Photosystem I–Polyaniline Composite Films for Biohybrid Solar Energy Conversion. *ACS Appl. Mater. Interfaces* **2015**, *7*, 9328-9335.
3. LeBlanc, G.; Gizzie, E.; Yang, S.; Cliffel, D. E.; Jennings, G. K. Photosystem I Protein Films at Electrode Surfaces for Solar Energy Conversion. *Langmuir* **2014**, *30*, 10990-11001.
4. Nelson, N. Plant Photosystem I - The Most Efficient Nano-Photochemical Machine. *J. Nanosci. Nanotechnol.* **2009**, *9*, 1709-1713.
5. Brettel, K.; Leibl, W. Electron Transfer in Photosystem I. *Biochim. Biophys. Acta - Bioenergetics* **2001**, *1507*, 100-114.
6. Ciesielski, P. N.; Hijazi, F. M.; Scott, A. M.; Faulkner, C. J.; Beard, L.; Emmett, K.; Rosenthal, S. J.; Cliffel, D.; Kane Jennings, G. Photosystem I – Based Biohybrid Photoelectrochemical Cells. *Bioresour. Technol.* **2010**, *101*, 3047-3053.
7. Ciobanu, M.; Kincaid, H. A.; Lo, V.; Dukes, A. D.; Kane Jennings, G.; Cliffel, D. E. Electrochemistry and Photoelectrochemistry of Photosystem I Adsorbed on Hydroxyl-Terminated Monolayers. *J. Electroanal. Chem.* **2007**, *599*, 72-78.
8. Greenbaum, E. Platinized Chloroplasts: A Novel Photocatalytic Material. *Science* **1985**, *230*, 1373-1375.
9. Gerster, D.; Reichert, J.; Bi, H.; Barth, J. V.; Kaniber, S. M.; Holleitner, A. W.; Visoly-Fisher, I.; Sergani, S.; Carmeli, I. Photocurrent of a Single Photosynthetic Protein. *Nat. Nanotechnol.* **2012**, *7*, 673-676.
10. Das, R.; Kiley, P. J.; Segal, M.; Norville, J.; Yu, A. A.; Wang, L.; Trammell, S. A.; Reddick, L. E.; Kumar, R.; Stellacci, F.; Lebedev, N.; Schnur, J.; Bruce, B. D.; Zhang, S.; Baldo, M. Integration of Photosynthetic Protein Molecular Complexes in Solid-State Electronic Devices. *Nano Lett.* **2004**, *4*, 1079-1083.

11. Terasaki, N.; Yamamoto, N.; Hiraga, T.; Yamanoi, Y.; Yonezawa, T.; Nishihara, H.; Ohmori, T.; Sakai, M.; Fujii, M.; Tohri, A.; Iwai, M.; Inoue, Y.; Yoneyama, S.; Minakata, M.; Enami, I. Plugging a Molecular Wire into Photosystem I: Reconstitution of the Photoelectric Conversion System on a Gold Electrode. *Angew. Chem. Int. Ed.* **2009**, *48*, 1585-1587.
12. Yamanoi, Y.; Terasaki, N.; Miyachi, M.; Inoue, Y.; Nishihara, H. Enhanced Photocurrent Production by Photosystem I with Modified Viologen Derivatives. *Thin Solid Films* **2012**, *520*, 5123-5127.
13. Terasaki, N.; Yamamoto, N.; Hiraga, T. Photo-sensor with Photo-electric Conversion Molecules and a Modified Gold Nanostructured FET Gate Film. *Thin Solid Films* **2009**, *518*, 656-660.
14. Terasaki, N.; Yamamoto, N.; Hattori, M.; Tanigaki, N.; Hiraga, T.; Ito, K.; Konno, M.; Iwai, M.; Inoue, Y.; Uno, S.; Nakazato, K. Photosensor Based on an FET Utilizing a Biocomponent of Photosystem I for Use in Imaging Devices. *Langmuir* **2009**, *25*, 11969-74.
15. Faulkner, C. J.; Lees, S.; Ciesielski, P. N.; Cliffel, D. E.; Jennings, G. K. Rapid Assembly of Photosystem I Monolayers on Gold Electrodes. *Langmuir* **2008**, *24*, 8409-8412.
16. Ciesielski, P. N.; Scott, A. M.; Faulkner, C. J.; Berron, B. J.; Cliffel, D. E.; Jennings, G. K. Functionalized Nanoporous Gold Leaf Electrode Films for the Immobilization of Photosystem I. *ACS Nano* **2008**, *2*, 2465-2472.
17. Kothe, T.; Pöller, S.; Zhao, F.; Fortgang, P.; Rögner, M.; Schuhmann, W.; Plumeré, N. Engineered Electron Transfer Chain in Photosystem I Based Photocathodes Outperforms Electron Transfer Rates in Natural Photosynthesis. *Chem. Eur. J.* **2014**, *20*, 11029-11034.
18. Ciesielski Peter, N.; Faulkner Christopher, J.; Irwin Matthew, T.; Gregory Justin, M.; Tolk Norman, H.; Cliffel David, E.; Jennings, G. K. Enhanced Photocurrent Production by Photosystem I Multilayer Assemblies. *Adv. Funct. Mater.* **2010**, *20*, 4048-4054.
19. LeBlanc, G.; Chen, G.; Gizzie Evan, A.; Jennings, G. K.; Cliffel David, E. Enhanced Photocurrents of Photosystem I Films on p-Doped Silicon. *Adv. Mater.* **2012**, *24*, 5959-5962.

20. Kim, I.; Bender, S. L.; Hranisavljevic, J.; Utschig, L. M.; Huang, L.; Wiederrecht, G. P.; Tiede, D. M. Metal Nanoparticle Plasmon-Enhanced Light-Harvesting in a Photosystem I Thin Film. *Nano Lett.* **2011**, *11*, 3091-3098.
21. Cushing, S. K.; Li, J.; Meng, F.; Senty, T. R.; Suri, S.; Zhi, M.; Li, M.; Bristow, A. D.; Wu, N. Photocatalytic Activity Enhanced by Plasmonic Resonant Energy Transfer from Metal to Semiconductor. *J. Am. Chem. Soc.* **2012**, *134*, 15033-15041.
22. Li, J.; Cushing, S. K.; Meng, F.; Senty, T. R.; Bristow, A. D.; Wu, N. Plasmon-Induced Resonance Energy Transfer for Solar Energy Conversion. *Nat. Photonics* **2015**, *9*, 601.
23. Kinkhabwala, A.; Yu, Z.; Fan, S.; Avlasevich, Y.; Müllen, K.; Moerner, W. E. Large Single-Molecule Fluorescence Enhancements Produced by A Bowtie Nanoantenna. *Nat. Photonics* **2009**, *3*, 654-657.
24. Bardhan, R.; Grady, N. K.; Cole, J. R.; Joshi, A.; Halas, N. J. Fluorescence Enhancement by Au Nanostructures: Nanoshells and Nanorods. *ACS Nano* **2009**, *3*, 744-752.
25. Carmeli, I.; Lieberman, I.; Kravetsky, L.; Fan, Z.; Govorov, A. O.; Markovich, G.; Richter, S. Broad Band Enhancement of Light Absorption in Photosystem I by Metal Nanoparticle Antennas. *Nano Lett.* **2010**, *10*, 2069-2074.
26. Govorov, A. O.; Carmeli, I. Hybrid Structures Composed of Photosynthetic System and Metal Nanoparticles: Plasmon Enhancement Effect. *Nano Lett.* **2007**, *7*, 620-625.
27. Fofang, N. T.; Park, T.-H.; Neumann, O.; Mirin, N. A.; Nordlander, P.; Halas, N. J. Plexcitonic Nanoparticles: Plasmon-Exciton Coupling in Nanoshell-J-Aggregate Complexes. *Nano Lett.* **2008**, *8*, 3481-3487.
28. Terasaki, N.; Yamamoto, N.; Hiraga, T.; Sato, I.; Inoue, Y.; Yamada, S. Fabrication of Novel Photosystem I-Gold Nanoparticle Hybrids and Their Photocurrent Enhancement. *Thin Solid Films* **2006**, *499*, 153-156.
29. Nishijima, Y.; Ueno, K.; Yokota, Y.; Murakoshi, K.; Misawa, H. Plasmon-Assisted Photocurrent Generation from Visible to Near-Infrared Wavelength Using a Au-Nanorods/TiO₂ Electrode. *J. Phys. Chem. Lett.* **2010**, *1*, 2031-2036.
30. Lalanne, P.; Hugonin, J. P.; Rodier, J. C. Theory of Surface Plasmon Generation at Nanoslit Apertures. *Phys. Rev. Lett.* **2005**, *95*, 263902.

31. Zeng, Z.; Mendis, M. N.; Waldeck, D. H.; Wei, J. A Semi-Analytical Decomposition Analysis of Surface Plasmon Generation and The Optimal Nanoledge Plasmonic Device. *RSC Adv.* **2016**, *6*, 17196-17203.
32. Tian, L.; Xu, P.; Chukhutsina, V. U.; Holzwarth, A. R.; Croce, R. Zeaxanthin-dependent Nonphotochemical Quenching Does Not Occur in Photosystem I in the Higher Plant *Arabidopsis Thaliana*. *Proc. Natl. Acad. Sci. U.S.A* **2017**, *114*, 4828.
33. Zeng, Z.; Wei, J.; Liu, Y.; Zhang, W.; Mabe, T. Magnetoreception of Photoactivated Cryptochrome 1 in Electrochemistry and Electron Transfer. *ACS Omega* **2018**, *3*, 4752-4759.
34. Zeng, Z.; Shi, X.; Mabe, T.; Christie, S.; Gilmore, G.; Smith, A. W.; Wei, J. Protein Trapping in Plasmonic Nanoslit and Nanoledge Cavities: The Behavior and Sensing. *Anal. Chem.* **2017**, *89*, 5221-5229.
35. Zeng, Z.; Liu, Y.; Wei, J. Recent Advances in Surface-enhanced Raman Spectroscopy (SERS): Finite-difference Time-domain (FDTD) Method for SERS and Sensing Applications. *Trends Anal. Chem.* **2016**, *75*, 162-173.
36. Wei, J.; Liu, H.; Dick, A. R.; Yamamoto, H.; He, Y.; Waldeck, D. H. Direct Wiring of Cytochrome c's Heme Unit to an Electrode: Electrochemical Studies. *J. Am. Chem. Soc.* **2002**, *124*, 9591-9599.
37. Mu, Y. Chemical Functionalization of GaN Monolayer by Adatom Adsorption. *J. Phys. Chem. C* **2015**, *119*, 20911-20916.
38. Zeng, Z.; Zhang, W.; Arvapalli, D. M.; Bloom, B.; Sheardy, A.; Mabe, T.; Liu, Y.; Ji, Z.; Chevva, H.; Waldeck, D. H.; Wei, J. A Fluorescence-Electrochemical Study of Carbon Nanodots (CNDs) in Bio- and Photoelectronic Applications and Energy Gap Investigation. *Phys. Chem. Chem. Phys.* **2017**, *19*, 20101-20109.
39. Amunts, A.; Drory, O.; Nelson, N. The Structure of a Plant Photosystem I Supercomplex at 3.4 Å Resolution. *Nature* **2007**, *447*, 58-63.
40. Yehezkeli, O.; Tel-Vered, R.; Wasserman, J.; Trifonov, A.; Michaeli, D.; Nechushtai, R.; Willner, I. Integrated Photosystem II-Based Photo-Bioelectrochemical Cells. *Nat. Commun.* **2012**, *3*, 742.
41. Dunahay, T. G.; Staehelin, L. A. Isolation of Photosystem I Complexes from Octyl Glucoside/Sodium Dodecyl Sulfate Solubilized Spinach Thylakoids. *Plant Physiol.* **1985**, *78*, 606-613.

42. Kaye, S.; Zeng, Z.; Sanders, M.; Chittur, K.; Koelle, P. M.; Lindquist, R.; Manne, U.; Lin, Y.; Wei, J. Label-Free Detection of DNA Hybridization with a Compact LSPR-Based Fiber-Optic Sensor. *Analyst* **2017**, *142*, 1974-1981.
43. Maier, S. A. *Plasmonics: Fundamentals and Applications*, Springer US: 2007.
44. Emmanuel, F.; Samuel, G. Surface Enhanced Fluorescence. *J. Phys. D* **2008**, *41*, 013001.
45. Li, J.; Cushing, S. K.; Zheng, P.; Meng, F.; Chu, D.; Wu, N. Plasmon-Induced Photonic and Energy-Transfer Enhancement of Solar Water Splitting by A Hematite Nanorod Array. *Nat. Commun.* **2013**, *4*, 2651.
46. Cushing, S. K.; Wu, N. Progress and Perspectives of Plasmon-Enhanced Solar Energy Conversion. *J. Phys. Chem. Lett.* **2016**, *7*, 666-675.
47. Koh, A. L.; Fernández-Domínguez, A. I.; McComb, D. W.; Maier, S. A.; Yang, J. K. W. High-Resolution Mapping of Electron-Beam-Excited Plasmon Modes in Lithographically Defined Gold Nanostructures. *Nano Lett.* **2011**, *11*, 1323-1330.
48. Wu, N. Plasmonic Metal-Semiconductor Photocatalysts and Photoelectrochemical Cells: A Review. *Nanoscale* **2018**, *10*, 2679-2696.

CHAPTER VII

CONCLUSION AND FUTURE CONSIDERATIONS

The primary objective of the research within this dissertation was to develop new scientific knowledge and use that knowledge to create a point-of-care diagnostic device. The goal was to design, optimize, fabricate, and perform analyses with plasmonic biosensors. The theme of the work was centered on micro- and nanofabrication, surface functionalization, and plasmonic biosensing. The goal was to design and fabricate novel structures that would enhance the sensitivity and/or allow for the potential to detect analytes in complex samples, such as blood serum. In regards to the surface functionalization, the goal was to find chemical linkers and binding ligands (DNA aptamer vs. antibody), which gave an optimal performance for a plasmonic biosensor. After fabricating the structures and decorating the sensor surface with ligands, plasmonic sensing could ensue. A large portion of the dissertation was dedicated towards enhancing the sensitivity of the sensor. This was accomplished by adding an additional layer (bimetallic approach in Chapter II or a capping dielectric layer in Chapter III and V) and by novel nanostructures (nanoledge in Chapter III and V). Chapters IV and V were dedicated to the fabrication and use of a flow-over fluidic dam.

A bimetallic nanoslit substrate was presented in Chapter II for an increase in sensitivity over gold equivalent devices. A device with a bilayer of Ag/Au layer was

chosen due to the great optical and electrical properties of silver with an outer layer of inert gold that would not oxidize upon contact with a sample solution. A 10% increase in bulk sensitivity was realized while the surface sensitivity was increased by 62%. This high increase in the surface sensitivity can be attributed to the short decay length of the plasmon wave with LSPR. This confined decay length affords high sensitivity near the metal surface. Cleaning the devices with oxygen generating species such as H_2SO_4 and H_2O_2 became problematic, as there was a reaction with silver. This made reusing the devices somewhat problematic.

A novel nanoledge structure with a SiO_2 capping layer was presented in Chapter III. The nanoledge structure, with a 50 nm inner slit and a 280 nm wide opening, was chosen to yield high sensitivity and large peak shifts along with an aperture that allowed protein delivery into the sensing area. Slits with widths less than 100 nm are needed for intense plasmon coupling, while a larger opening (280 nm) is needed to allow for proteins to easily enter into the sensing area for nanometer sized protein trapping and biosensing. The SiO_2 capping layer was used to promote binding events to occur exclusively in the nano-cavity. TIRF imaging showed that proteins could diffuse their way into nanoledge structures, with a 280 nm open gap. TIRF imaging was performed on a straight nanoslits of similar size (100 nm and 300 nm) to investigate the protein migration behavior. Binding events between a monoclonal antibody and f-PSA were monitored with a wavelength peak shift.

Chapter IV served as a technical microfabrication chapter. A flow-over fluidic dam was designed and fabricated to decrease diffusion times of analytes to the sensing area, act as a barrier to exclude micron sized particles from the sensing area, and not clog like flow-through systems. Flow-over fluidic dams were fabricated with three different sidewall profiles: undercut, overcut, and T topped. The overcut sidewall profile was mandatory in creating a plasmonic biosensor because the sidewalls could be coated during metal evaporation yielding opaque sidewalls. The issue with transparent sidewalls was that light escaped from the sidewalls during a tSPR measurement. Fluidic dams with overcut sidewalls were fabricated using SU-8 photoresist with a multi-layered resist approach. SU-8 3005 was chosen because a DRIE tool was not available to etch deep trenches into a glass substrate and SU-8 had properties of interest. Those properties were that SU-8 3005 was optically transparent, was easily etched with a standard RIE tool, was a high refractive index material, showed good adhesion to SiO₂ and gold films, and that thick layers could be applied and patterned. Using the MLR approach allowed for the sidewalls to have slopes between 50° and 70°, which falls in the range for the sidewalls to be coated when using a line-of-sight technique like PVD evaporation. Positive tone photoresists do have overcut profiles, but the slopes are typically closer to 85°. Also, no positive tone photoresist met all of the needs listed above for SU-8 3005.

Troponin T biosensing was the topic of Chapter V. The fabricated fluidic dam structures were compared for their ability to allow micron sized fluorescent particles to pass over the dam. The undercut profile retained the microspheres while the overcut

profile allowed the microspheres to pass over the sensing area. This experiment gave a second reason why the overcut sidewall was needed. Self-assembly was used to attach DNA aptamers to the sensor surface. Binding events between the DNA aptamer and troponin T protein were monitored by a resonant peak shift. A logarithmic correlation was found between the protein concentration and the peak shift. IL-6 was used in the sample solution, as opposed to troponin T, for a control experiment. With a very large concentration of IL-6 protein in the sample, no notable peak shift was observed.

Chapter VI was in regards to the fabrication and use of a photocurrent-generating device. A photoactive protein (PSI) was immobilized into a nanoslit. Investigated were the relationship between surface plasmon generation efficiency of nanoslit structures and the experimentally obtained photocurrent by immobilizing PSI on the gold nanoslit electrode surfaces regarding different nanoslit widths. The enhancement of photocurrent generation was on the foundation of plasmonic light trapping and plasmon-induced resonance energy transfer.

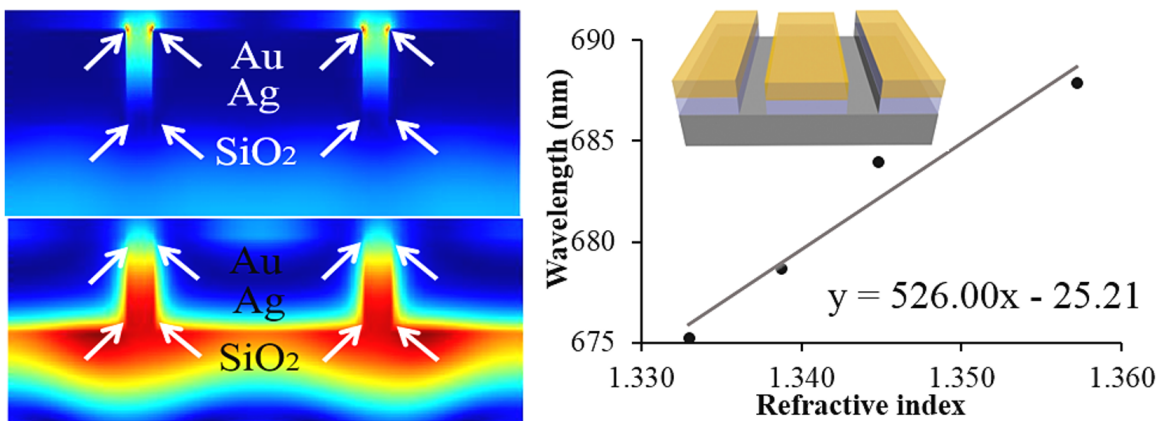
Future work to follow the research outlined in this dissertation will be towards detecting multiple analytes at one time, called multiplexing. Multiple nanostructured arrays and multiple flow channels could be created to allow for on-chip analysis of several protein biomarkers during a single experiment. This would also allow for on-chip control experiments. The end goal is to create a commercial sensor that is sensitive, portable, and able to handle complex samples without any pre-treatment. All of the research presented in the preceding chapters were in buffer or diluted serum. The logical

next step would be to work with diluted whole blood and then whole blood. The fluidic dam presented in Chapter IV was solely for use in complex media, like whole blood samples. After speaking with health care workers and emergency responders, it became apparent that finger-prick blood samples have several benefits compared to a venous blood draw. For one, they are much easier to perform and cause less anxiety and pain for the patient. Additionally, only paramedics can perform venous blood draws, while all emergency care workers (EMS basic, EMS advanced, and paramedics) can perform finger-prick blood draws. Therefore, if the final device could work with finger-prick blood samples then that would be a benefit in the pre-hospital setting. The last future consideration would be to attach the detection chip to a smart phone. Transmission SPR with a nanostructured substrates allows for the complex optics, prism, and laser of Kretschmann SPR to be replaced with a simple white light and camera. Thus, using a smart phone as the light source, camera, and interfacing software would allow for the development of a truly portable sensor without the cost of the instrument. Only the chip and a plastic device to mount the chip near the phone would be needed.

APPENDIX A

SUPPORTING INFORMATION FOR CHAPTER II

Graphical Abstract



An investigation of bimetallic (Ag/Au) nanoslit films with little-diffusing, long-term stable and temperature insensitive properties focusing on optical properties and refractive index sensitivity as a comparison to pure gold nanoslit films was conducted by using a semi-analytical analysis, FDTD simulation and SPR optical transmission.

Experimental Section

Fabrication of Metallic Film Nanoslit: The fabrication process is as follows: glass cleaning, thin film deposition, nanofabrication, and flow cell fabrication. Standard glass slides (75 x 25 x 1 mm, VWR) were used as substrates either as is or cut to size. The substrates were cleaned in a piranha bath (3:1 H₂SO₄:H₂O₂) followed by a DI water rinse (18.2 MΩ) then dried with nitrogen. Cleaned substrates were baked at 150 °C in an oven (282A, Fisher) while under vacuum. The clean, dried slides were placed into an electron beam evaporator (PVD75, Kurt Lesker) and pumped to a base pressure of 1.1 x 10⁻⁶ Torr. A 7kV e-beam sequentially coated the slides with 2.5 nm of Ti (0.4 Å/sec), 50.0 nm of

Ag (3.1 Å/sec), and 50.1 nm of Au (1.9 Å/sec) for the bimetallic devices and 2.7 nm of Ti (0.3 Å/sec) and 100.0 nm of Au (3.5 Å/sec) for the gold devices. All metals were purchased from Kurt Lesker. Titanium was used as an adhesion layer to promote the bonding of each noble metal to glass substrates. Titanium was chosen over the more commonly used chromium due to its smooth, level profile as well as the lower optical absorbance of titanium.¹ The literature suggests that chromium is also more reactive to contaminants on glass surfaces, giving defects more frequently with chromium layers.¹ The film thickness of each metal was monitored via a quartz crystal microbalance (QCM) and later checked with a profilometer (Tencor P-10, KLA). Focused ion beam milling (Auriga Dual Beam FIB/SEM, Carl Zeiss) with upgraded software (NPVE, Fibics) was used to fabricate the nanoslit arrays. Custom made aluminum substrate holders were manufactured at a local machine shop and afforded a conductive path to ground inside the FIB/SEM without the need for conductive adhesives, which often diminished the transparency of the glass even after removal. The nanoslit arrays consisted of 50 slits milled into the metal. The slit dimensions were 50 nm x 20 μm or 100 nm x 20 μm. The nanoslit arrays covered a range of widths (22.1 μm to 36.8 μm), as various periods were investigated. For each periodicity, 50 slits were milled with a Ga⁺ beam using a dose of 0.070 - 0.250 nC/μm² for the bimetallic films and 0.140 – 0.700 nC/μm² for the gold films. FIB probes of either 30kV:30pA or 30kV:50pA through an 80 μm aperture afforded 50 nm slits (± 6 nm depending on the probe alignment and focusing that day). The periodicities ranged from 400 nm to 700 nm which dictated the array widths. For

each nanoslit array a corresponding reference box was milled a minimum distance of 1 mm away from the nearest nanoslit array using a 30kV:4nA probe at 0.150 – 0.400 nC/ μm^2 through a 700 μm FIB aperture. This gave a transparent window the same size (20 μm \times 27 μm) as each nanoslit array and was used for reference measurements.

Sample Characterization: Scanning electron microscopy (Auriga Dual Beam FIB/SEM, Carl Zeiss) was used to visualize the nanostructuring and to confirm the periodicity and dimensions of each nanoslit array and reference box. SEM images were captured using a secondary electron detector, a 5 kV acceleration voltage, and a 5.0 mm working distance. The dimensions of each array and reference box were also confirmed with profilometry (KLA Tencor, P-10) and atomic force microscopy (Agilent 5600 LS AFM). Transmission surface plasmon resonance (tSPR) was used to monitor binding events and local RI changes by a redshift in the primary resonant peak. A tungsten halogen light source (Ocean Optics, LS-1) with a spectral range of 360 - 2000 nm was fed through fiber optics into a holder that was designed in CAD then printed using a 3D printer. Fiber optic cables allowed for the placement and focusing of white light onto the underside of the substrate/flow cell. The light was collected by a 50X objective (Olympus LMPlanFLN) on an Olympus BX-41 microscope. The CCD of a Horiba Xplora was used for data collection. The temperature was monitored using an electric thermocouple thermometer (Amprobe TMD-52). Measurements were taken in real-time over the nanoslit array, a reference box of the same dimensions as the nanoslit array, and a dark background measurement, which corrected for the small amount of light that transmitted through the

thin metallic film. The metallic film, 100 nm in thickness, essentially blocked all of the light. Therefore, the light collected by the CCM was due to the EOT effect.² The transmission was calculated as follows:

$$Transmittance = 100 \times \frac{slit-dark}{ref.-dark} \quad (\text{Eq. A1})$$

SIMS analysis were performed at NC State University with a TOF SIMS V (ION TOF) instrument using a Bi⁺ liquid metal gun and a Cs⁺ sputtering gun.

Chip and Flow-Chamber Setup: The metallic substrate with nanoslits functioned as the bottom to an enclosed flow cell with the top portion composed of either polyethylene (PE) or glass. This top substrate contained the flow channel, which had the dimensions 50.0 x 5.0 x 0.4 mm and a total volume of 100 μ L. PE devices were purchased from IBIDI and glass devices were fabricated using standard photolithographic techniques. Prior to sealing the two pieces together, both were cleaned with a series of solvents (acetone, isopropanol, DI water) and subjected to an oxygen plasma cleaning (Plasma Etch Inc. PE-100 Plasma Etch). An adhesive (3M, VHB) or UV epoxy (Microchem, SU-8 2005) was used to affix the flow cell to the metallic substrate. A syringe pump (Harvard, PHD 2000) was used to manipulate fluids through the enclosed chip and was connected to a degasser (Biotech, 2003 Degasser) to remove air bubbles from the system.

Self-assembled Monolayer Preparation: The self-assembly of alkanethiols on a cleaned substrate housed inside of a flow cell, were monitored using transmission surface plasmon resonance (tSPR). The substrates were cleaned by oxygen plasma for 5 min at

100 W in an oxygen plasma cleaner (South Bay Technologies PC-2000 Plasma Cleaner) at an O₂ pressure of 177.2 mTorr and a DC bias of -773 volts. This was followed by a DI water rinse, 0.1% Tween 20 rinse, and a second DI water rinse. The adsorption of alkanethiols onto the cleaned surface was monitored by a resonant peak shift. 16-mercaptohexadecanoic acid (16-MHDA) was purchased from Sigma Aldrich and self-assembled onto the metallic surfaces. A 5 mM ethanol solution of 16-MHDA was monitored in real-time using tSPR. The tSPR measurements were taken in air without SAM, in pure ethanol without SAM, and then 5 mM SAM solutions in ethanol were taken at 1 minute, 30 minutes, 1 hour, 2.5 hours, and then every hour. The flow cell was then flushed with ethanol, dried with N₂, and tSPR measurements taken. To regenerate the clean metallic surface the adsorbed SAM was removed by subjecting the substrates to oxygen plasma for 5 minutes at 100 W. The substrates were then exposed to sonication in a series of solvents (acetone, ethanol, water)³ and then cleaned by 20 minutes of UV/Ozone exposure⁴ using a Bioforce UV/Ozone ProCleaner. It has previously been demonstrated that plasma cleaning does not adversely affect the metallic surfaces and does not add roughness to the surface.⁵ This is in contrast to the roughness and pinholes⁶ that can occur by some cleaning methods, such as the use of piranha, which is a mixture of sulfuric acid and hydrogen peroxide.

Semi-analytical Analysis: In order to study nanoslit geometries that are of interest in practice and consider the geometric diffraction with the bounded surface plasmon (SP) modes launching on the flat interfaces surrounding the slits, the SP scattering coefficients

and efficiencies at the slit apertures need to be considered. With the semi-analytical model,² the SP excitation efficiency, e , which is defined as the rate of SPP launching and scattering by matching the continuous electromagnetic fields quantities at the interface,^{2,7} for the Ag (or Au)/SiO₂ interface at the bottom of the nanoslit aperture for one side of the aperture can be calculated using the following equations:

$$e_{(AgorAu)} = |\alpha_{(AgorAu)}^+(w/2)|^2 = |\alpha_{(AgorAu)}^-(w/2)|^2 = \frac{4w'n_{SiO_2}^3}{\pi n_{air}^2} \left| \frac{\varepsilon_{Ag/Au}^{1/2}}{\varepsilon_{Ag/Au} + n_{SiO_2}^2} \right| \left| \frac{I_1}{1 + (n_{SiO_2}/n_{air})w'I_0} \right|^2 \quad (\text{Eq. A2})$$

in which

$$I_0 = \int_{-\infty}^{\infty} du [\sin(\pi w'u)/(\pi w'u)]^2 / v \quad (\text{Eq. A3})$$

$$I_1 = \int_{-\infty}^{\infty} du \frac{\exp(-i\pi w'u)\sin(\pi w'u)/(\pi w'u)}{v\{v + [n_{SiO_2}^2/(\varepsilon_{AgorAu} + n_{SiO_2}^2)]^{1/2}\}} \quad (\text{Eq. A4})$$

$$w' = n_{SiO_2}w/\lambda \quad (\text{Eq. A5})$$

Similarly, for the Au/medium interface at the top of the nanoslit aperture (blue), e is given by

$$e_{(top)} = |\alpha_{(top)}^+(w'/2)|^2 = |\alpha_{(top)}^-(w'/2)|^2 = \frac{4w'n_{air}^2}{\pi n_{air}} \left| \frac{\varepsilon_{Au}^{1/2}}{\varepsilon_{Au} + n_{air}^2} \right| \left| \frac{I'_1}{1 + (n_{air}/n_{air})w'I'_0} \right|^2 \quad (\text{Eq. A6})$$

with

$$I'_0 = \int_{-\infty}^{\infty} du [\sin(\pi w'u)/(\pi w'u)]^2 / v \quad (\text{Eq. A7})$$

$$I'_1 = \int_{-\infty}^{\infty} du \frac{\exp(-i\pi w'u)\sin(\pi w'u)/(\pi w'u)}{v\{v + [n_{air}^2/(\varepsilon_{Au} + n_{air}^2)]^{1/2}\}} \quad (\text{Eq. A8})$$

$$herew' = n_{air}w'/\lambda, \quad (\text{Eq. A9})$$

where e is the SP generation efficiency, α is the SP generation coefficient, w is the width of the nanoslit structure, ε is the dielectric constant, n is the refractive index, I is the integration calculation, w' represents the scaled width and u and v are applied for numerical integration with $u^2+v^2=1$.

Finite-Difference Time-Domain (FDTD) Simulations: Numerical simulations were conducted using the FDTD method. A three-dimensional (3D) FDTD method was used to calculate the light transmission and electric-magnetic field intensity profiles of the nanoslit arrays along the metallic films with the following simulation details. The total mesh area had a background RI of 1.0 (air). Periodic boundary conditions (BCs) and perfectly matched layer (PML) BCs were applied along x-, y-, and z-boundaries of the unit cell, respectively. The indices of Au, Ag and SiO₂ followed the data of optical constants of solids. Light transmission calculations were performed on arrays with a 50 nm slit width and a periodicity of 450 nm, 500 nm, or 550 nm. Electric-magnetic field distribution calculations were performed on 50 nm or 100 nm slits with a 450 nm periodicity. Using the Drude-Lorentz model, a Fourier transform of the polarization was used in the model and implementing it into the FDTD formalism resulted in the transverse electric (TE) and transverse magnetic (TM) equations. The components of E_x , E_y , and H_z can be used to solve TE equations and those of H_x , H_y , and E_z can be used to solve TM equations, respectively.

Supporting Figures and Data Tables

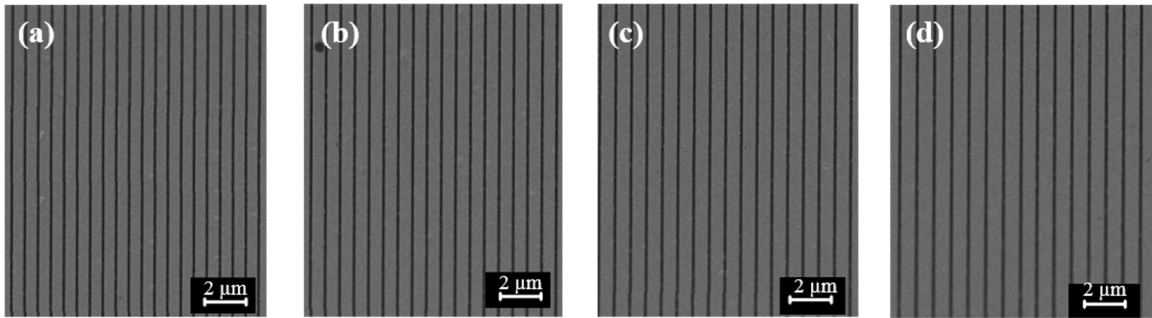


Figure A1. SEM Images of a Representative Au Nanoslit Array with 50 nm Width and a Periodicity of (a) 550 nm (b) 600 nm (c) 650 nm (d) 700 nm, Respectively.

Semi-analytical analysis results:

Table A1

I_0 and I_1 for Silver at Different Wavelengths When the Refractive Index n_{SiO_2} is 1.41 (I_0 Equals to Each Other for Different λ)

		600nm $\epsilon =$ -15.97+ 2.11i	700nm $\epsilon =$ -23.04+ 2.59i	800nm $\epsilon =$ -31.19+ 3.03i	900nm $\epsilon =$ -40.53+ 3.47i	1000nm $\epsilon =$ -51.06+ 3.92i	1100nm $\epsilon =$ -62.80+ 4.37i	1200nm $\epsilon =$ -75.76+ 4.83i
W'	I_0	I_1	I_1	I_1	I_1	I_1	I_1	I_1
0.1	3.09- 4.09i	0.18-2.85j	0.31-2.89j	0.40- 2.91j	0.47-2.92j	0.52-2.93j	0.57- 2.94j	0.60-2.94j
0.2	2.94- 2.61i	0.89-2.46j	1.04-2.47j	1.14- 2.47j	1.21-2.47j	1.27-2.47j	1.31- 2.46j	1.35-2.46j
0.3	2.72- 1.69i	1.38-1.89j	1.52-1.87j	1.62- 1.84j	1.69-1.82j	1.75-1.80j	1.79- 1.79j	1.83-1.77j
0.4	2.43- 1.05i	1.60-1.25j	1.72-1.19j	1.81- 1.14j	1.87-1.10j	1.91-1.07j	1.95- 1.04j	1.98-1.02j
0.5	2.13- 0.64i	1.56-0.65j	1.65-0.56j	1.71- 0.50j	1.76-0.44j	1.79-0.40j	1.82- 0.37j	1.84-0.34j

Table A1

Cont.

		600nm $\epsilon =$ -15.97+ 2.11i	700nm $\epsilon =$ -23.04+ 2.59i	800nm $\epsilon =$ -31.19+ 3.03i	900nm $\epsilon =$ -40.53+ 3.47i	1000nm $\epsilon =$ -51.06+ 3.92i	1100nm $\epsilon =$ -62.80+ 4.37i	1200nm $\epsilon =$ -75.76+ 4.83i
0.6	1.82- 0.34i	1.32-0.18j	1.38-0.08j	1.41- 0.01j	1.44+ 0.04j	1.45+ 0.09j	1.46+ 0.13j	1.47+ 0.16j
0.7	1.54- 0.18i	0.98+ 0.10j	1.00+ 0.19j	1.01+ 0.26j	1.01+ 0.31j	1.01+ 0.35j	1.01+ 0.38j	1.01+ 0.41j
0.8	1.30- 0.10i	0.62+ 0.19j	0.62+ 0.26j	0.61+ 0.31j	0.60+ 0.35j	0.59+ 0.38j	0.58+ 0.40j	0.57+ 0.42j
0.9	1.11- 0.06i	0.34+ 0.13j	0.32+ 0.17j	0.30+ 0.20 j	0.28+ 0.22j	0.27+ 0.24j	0.26+ 0.25j	0.25+ 0.26j
1.0	0.97- 0.07i	0.17-0.02j	0.15-0.01j	0.14+ 0.00j	0.12+ 0.01j	0.11+ 0.01j	0.10+ 0.02j	0.09+ 0.02j

Table A2

I_0 and I_1 for Gold at Different Wavelengths When the Refractive Index n_{SiO_2} is 1.41 (I_0 Equals to Each Other for Different λ)

		600nm $\epsilon=$ -10.21+ 1.43i	700nm $\epsilon=$ -17.94+ 1.61i	800nm $\epsilon=$ -26.27+ 1.85i	900nm $\epsilon=$ -35.80+ 2.43i	1000nm $\epsilon=$ -46.05+ 3.11i	1100nm $\epsilon=$ -57.32+ 3.87i	1200nm $\epsilon=$ -68.98+ 4.68i
W'	I_0	I_1	I_1	I_1	I_1	I_1	I_1	I_1
0.1	3.09-4.09i	-0.02-2.76j	0.23-2.85j	0.35-2.89j	0.44-2.91j	0.50-2.92j	0.55-2.93j	0.58-2.94j
0.2	2.94-2.61i	0.67-2.41j	0.94-2.45j	1.08-2.46j	1.18-2.47j	1.24-2.47j	1.29-2.46j	1.33-2.46j
0.3	2.72-1.69i	1.16-1.90j	1.42-1.87j	1.56-1.85j	1.66-1.83j	1.72-1.81j	1.77-1.79j	1.81-1.78j
0.4	2.43-1.05i	1.39-1.31j	1.63-1.22j	1.75-1.16j	1.84-1.12j	1.89-1.08j	1.93-1.05j	1.97-1.03j
0.5	2.13-0.64i	1.40-0.75j	1.58-0.61j	1.67-0.53j	1.73-0.47j	1.77-0.42j	1.80-0.38j	1.83-0.35j
0.6	1.82-0.34i	1.21-0.31j	1.33-0.14j	1.39-0.05j	1.42+0.02j	1.44+0.07j	1.46+0.11j	1.47+0.14j
0.7	1.54-0.18i	0.92-0.02j	0.98+0.13j	1.00+0.22j	1.00+0.29j	1.01+0.33j	1.01+0.37j	1.01+0.39j
0.8	1.30-0.10i	0.61+0.09j	0.62+0.22j	0.61+0.28j	0.60+0.33j	0.59+0.37j	0.58+0.39j	0.57+0.41j
0.9	1.11-0.06i	0.35+0.06j	0.33+0.14j	0.31+0.18j	0.29+0.21j	0.28+0.23j	0.26+0.24j	0.25+0.25j
1.0	0.97-0.07i	0.19-0.06j	0.16-0.02j	0.15-0.00j	0.13+0.01j	0.12+0.01j	0.11+0.01j	0.10+0.02j

Table A3

Γ_0 and Γ_1 for gold at different wavelengths when the refractive index n_{air} is 1.0 (Γ_0 equals to each other for different λ)

		600nm $\epsilon=$ -10.21+ 1.43i	700nm $\epsilon=$ -17.94+ 1.61i	800nm $\epsilon=$ -26.27+ 1.85i	900nm $\epsilon=$ -35.80+ 2.43i	1000nm $\epsilon=$ -46.05+ 3.11i	1100nm $\epsilon=$ -57.32+ 3.87i	1200nm $\epsilon=$ -68.98+ 4.68i
w'	Γ_0	Γ_1	Γ_1	Γ_1	Γ_1	Γ_1	Γ_1	Γ_1
0.1	3.09-4.09i	0.27-2.89i	0.44-2.92i	0.53-2.93i	0.59-2.94i	0.63-2.94i	0.67-2.95i	0.69-2.95i
0.2	2.94-2.61i	0.99-2.48i	1.18-2.47i	1.27-2.47i	1.34-2.46i	1.39-2.46i	1.42-2.45i	1.45-2.45i
0.3	2.72-1.69i	1.48-1.89i	1.66-1.83i	1.75-1.80i	1.82-1.78i	1.86-1.76i	1.90-1.75i	1.92-1.74i
0.4	2.43-1.05i	1.69-1.22i	1.84-1.12i	1.92-1.06i	1.97-1.03i	2.01-1.00i	2.04-0.97i	2.06-0.96i
0.5	2.13-0.64i	1.63-0.60i	1.74-0.47i	1.79-0.40i	1.83-0.35i	1.85-0.31i	1.87-0.28i	1.89-0.26i
0.6	1.82-0.34i	1.37-0.12i	1.43+0.02i	1.45+0.09i	1.47+0.15i	1.48+0.18i	1.49+0.21i	1.49+0.24i
0.7	1.54-0.18i	1.00+0.16i	1.01+0.28i	1.01+0.35i	1.01+0.40i	1.00+0.43i	1.00+0.46i	1.00+0.48i
0.8	1.30-0.10i	0.62+0.24i	0.60+0.33i	0.58+0.38i	0.57+0.41i	0.56+0.44i	0.55+0.45i	0.54+0.47i
0.9	1.11-0.06i	0.33+0.16i	0.29+0.21i	0.27+0.24i	0.25+0.26i	0.24+0.27i	0.23+0.28i	0.22+0.28i
1.0	0.97-0.07i	0.16-0.01i	0.13+0.01i	0.11+0.01i	0.10+0.02i	0.09+0.02i	0.08+0.02i	0.07+0.02i

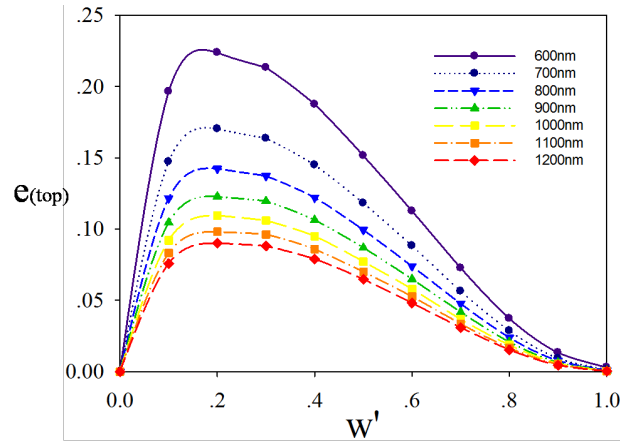


Figure A2. $e_{(top)}$ for Both the Bimetallic Nanoslit Structure and Au Nanoslit Structure.

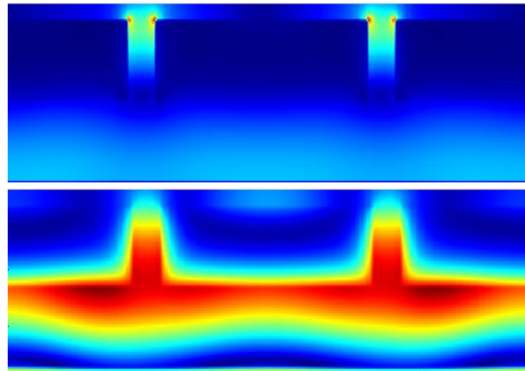


Figure A3. FDTD Simulation of Transverse Electro-magnetic Field Intensity for the 50-450 nm Gold Nanoslit Structure with Transverse Electric Field Intensity (Top) and Transverse Magnetic Field Intensity (Bottom).

References

1. B. A. Sexton, B. N. Feltis, T. J. Davis, *Sensors and Actuators A: Physical* **2008**, *141*, 471-475.
2. Z. Zeng, M. N. Mendis, D. H. Waldeck, J. Wei, *RSC Adv.* **2016**, *6*, 17196-17203.
3. J. Benesch, J. F. Mano, R. L. Reis, *Acta. Biomater.* **2010**, *6*, 3499-3505.

4. a) H. Ron, S. Matlis, I. Rubinstein, *Langmuir* **1998**, *14*, 1116-1121; b) C. G. Worley, R. W. Linton, *Journal of Vacuum Science & Technology A: Vacuum, Surfaces, and Films* **1995**, *13*, 2281-2284.
5. D. Berman, J. Krim, *Thin Solid Films* **2012**, *520*, 6201-6206.
6. J. Kang, P. A. Rowntree, *Langmuir* **2007**, *23*, 509-516.
7. P. Lalanne, J. P. Hugonin, J. C. Rodier, *Phys. Rev. Lett.* **2005**, *95*, 263902.

APPENDIX B

SUPPORTING INFORMATION FOR CHAPTER III

Methods

Semi-analytical analysis and FDTD simulations

With the semi-analytical model, the SP excitation efficiency e for one side of the aperture is readily calculated with the following equations:

$$e_1 = |\alpha_1^+(w_1/2)|^2 = |\alpha_1^-(w_1/2)|^2 = \frac{4w_1 n_1^3}{\pi n_2^2} \left| \frac{\varepsilon^{1/2}}{\varepsilon + n_1^2} \right| \left| \frac{I_1}{1 + (n_1/n_2)w_1 I_0} \right|^2$$

in which

$$I_0 = \int_{-\infty}^{\infty} du [\sin(\pi w_1' u) / (\pi w_1' u)]^2 / v$$

$$I_1 = \int_{-\infty}^{\infty} du \frac{\exp(-i\pi w_1' u) \sin(\pi w_1' u) / (\pi w_1' u)}{v \{v + [n_1^2 / (\varepsilon + n_1^2)]^{1/2}\}}, \text{ and}$$

$$w_1' = n_1 w_1 / \lambda$$

$$e_2 = |\alpha_2^+(w_1/2)|^2 = |\alpha_2^-(w_1/2)|^2 = \frac{4w_2 n_3^2}{\pi n_2} \left| \frac{\varepsilon^{1/2}}{\varepsilon + n_3^2} \right| \left| \frac{I_1'}{1 + (n_3/n_2)w_2 I_0'} \right|^2$$

with

$$I_0' = \int_{-\infty}^{\infty} du [\sin(\pi w_2' u) / (\pi w_2' u)]^2 / v$$

$$I_1' = \int_{-\infty}^{\infty} du \frac{\exp(-i\pi w_2' u) \sin(\pi w_2' u) / (\pi w_2' u)}{v \{v + [n_3^2 / (\varepsilon + n_3^2)]^{1/2}\}}, \text{ and}$$

$$w_2' = n_2 w_1 / \lambda$$

Similarly, for the Au/medium interface at the top of the nanoledge aperture (blue), e is given by

$$e_3 = |\alpha_3^+(w_2/2)|^2 = |\alpha_3^-(w_2/2)|^2 = \frac{4w_3 n_4^2}{\pi n_3} \left| \frac{\varepsilon^{1/2}}{\varepsilon + n_4^2} \right| \left| \frac{I_1''}{1 + (n_4/n_3)w_3 I_0''} \right|^2$$

with

$$I_0'' = \int_{-\infty}^{\infty} du [\sin(\pi w_3' u) / (\pi w_3' u)]^2 / v,$$

$$I_1'' = \int_{-\infty}^{\infty} du \frac{\exp(-i\pi w_3' u) \sin(\pi w_3' u) / (\pi w_3' u)}{v \{v + [n_4^2 / (\varepsilon + n_4^2)]^{1/2}\}}, \text{ and}$$

$$w_3' = n_3 w_2 / \lambda,$$

where e is the SP generation efficiency, α is the SP generation coefficient, w is the width of the nanoledge structure, ε is the dielectric constant, n is the refractive index, I is the integration calculation, w' represents the scaled width and u and v are applied for numerical integration with $u^2 + v^2 = 1$.

Moreover, FDTD simulations reiterate the previous study by adding additional 10 nm SiO₂ film at the top of Au layer. Refractive index of the SiO₂ film used in calculations was equal to 1.41.¹

Table B1

The SP Generation Efficiency e_1, e_2, e_3 for the Nanoledge Geometry w_2/w_1 of 280 -50nm with Different n

n_1, n_2, n_3, n_4	e_1	e_2	e_3	Δe
$n_1=1.45, n_2=n_3=1, n_4=1.41$	0.48	0.18	0.25	
$n_1=1.45, n_2=n_3=1.2, n_4=1.41$	0.38	0.25	0.20	-0.08
n_1, n_2, n_3, n_4	e_1	e_2	e_3	Δe
$n_1=1.45, n_2=n_3=n_4=1$	0.48	0.18	0.16	
$n_1=1.45, n_2=n_3=1, n_4=1.2$	0.48	0.18	0.20	0.04
$n_1=1.45, n_2=n_3=n_4=1.2$	0.38	0.25	0.15	-0.04
$n_1=1.45, n_2=n_3=1.2, n_4=1$	0.38	0.25	0.13	-0.06

Table B2

The SP generation efficiency e_1 , e_2 , e_3 for the nanoledge geometry w_2/w_1 of 280 -50 nm with different bulk refractive index ($n_1=1.45$, $n_4=1.41$, and $n_2=n_3=1.0-1.5$).

$n_2 = n_3$	e_1	e_2	e_3	Δe
1.0	0.48	0.18	0.25	0
1.1	0.42	0.21	0.23	-0.05
1.2	0.38	0.25	0.20	-0.08
1.3	0.34	0.28	0.18	-0.11
1.4	0.31	0.32	0.15	-0.14
1.5	0.28	0.35	0.12	-0.16

Table B3

The SP Generation Efficiency e_1 , e_2 , e_3 for the Nanoledge Geometry w_2/w_1 of 280nm-50nm with Different Bulk Refractive Index ($n_1=1.45$, $n_4=1$, and $n_2=n_3=1.0-1.5$)

$n_2 = n_3$	e_1	e_2	e_3	Δe
1.0	0.48	0.18	0.16	0
1.1	0.42	0.21	0.16	-0.03
1.2	0.38	0.25	0.15	-0.04
1.3	0.34	0.28	0.15	-0.05
1.4	0.31	0.32	0.14	-0.05
1.5	0.28	0.35	0.13	-0.06

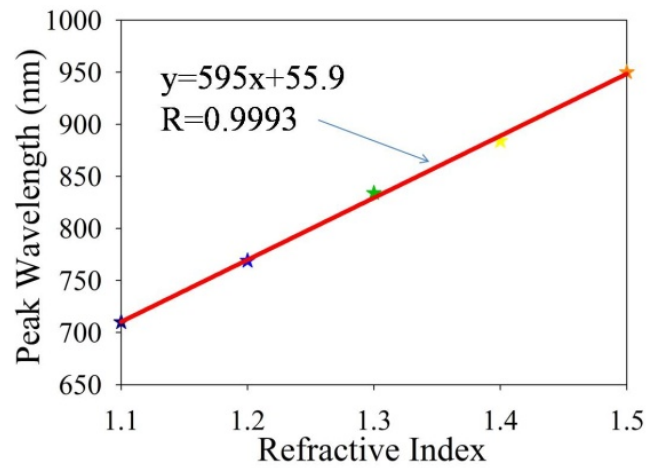


Figure B1. FDTD Calculation of the Peak Wavelength of 280-50 nm Nanoslit System vs. Refractive Indices of Bulk Solutions.

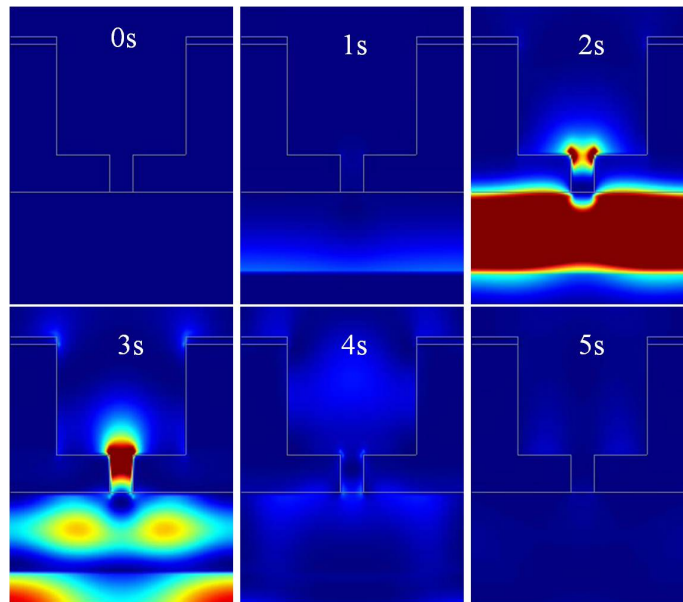


Figure B2. Movie Screenshots of the TE Field Propagation through the Simulation Volume of 280-50 nm Nanoedge System with SiO₂. The Time of Each Screenshot Shows the Elapsed Time of the Movie.

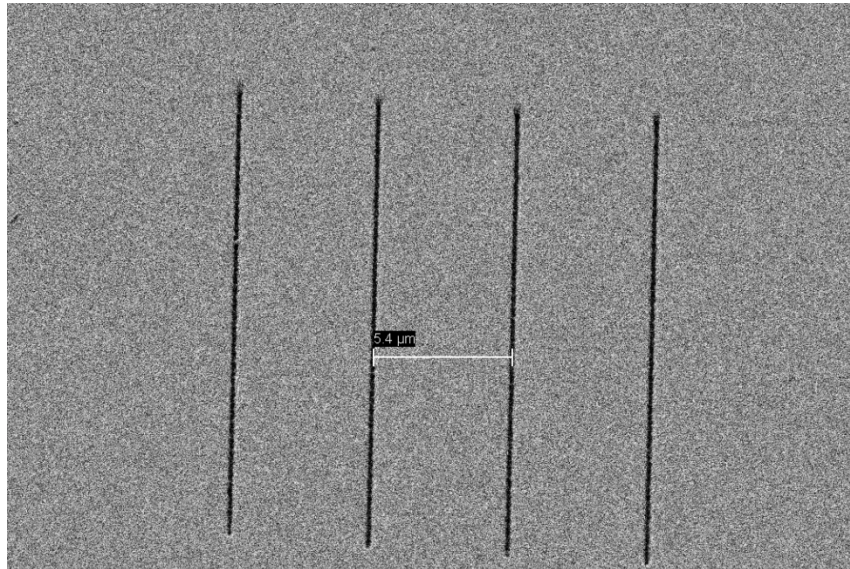


Figure B3. SEM Image of Nanoslits (100 nm Width) with Period of 5.4 μm.

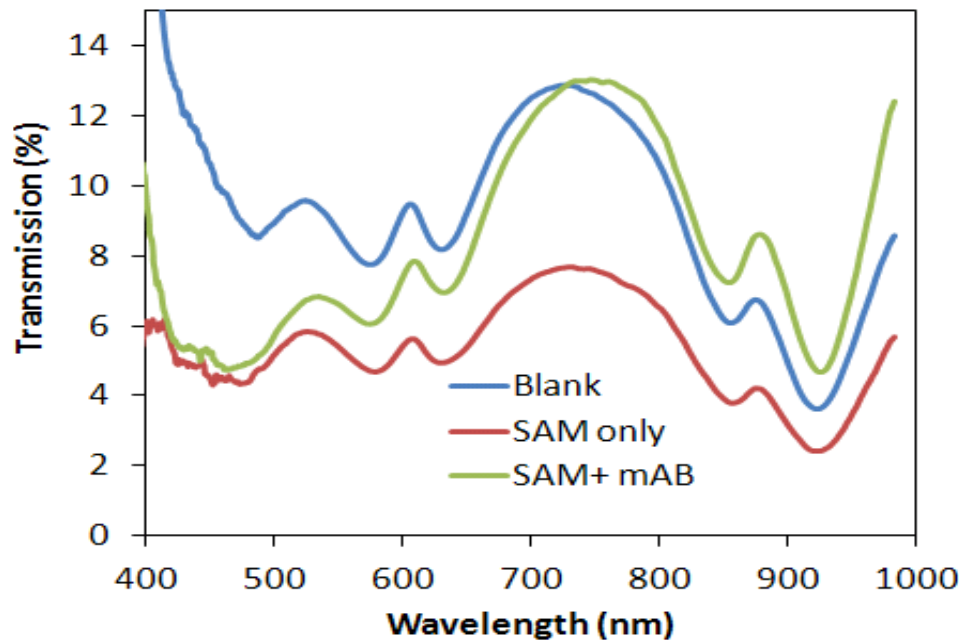


Figure B4. Optical Transmission through a Nanoledge Device.

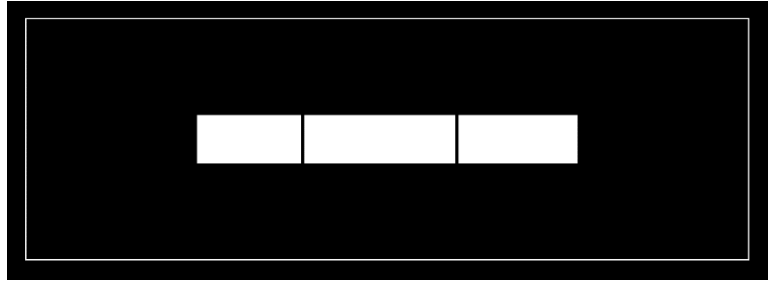


Figure B5. Design of Dark Field Photomask for Optical Lithography. Not Shown to Scale.

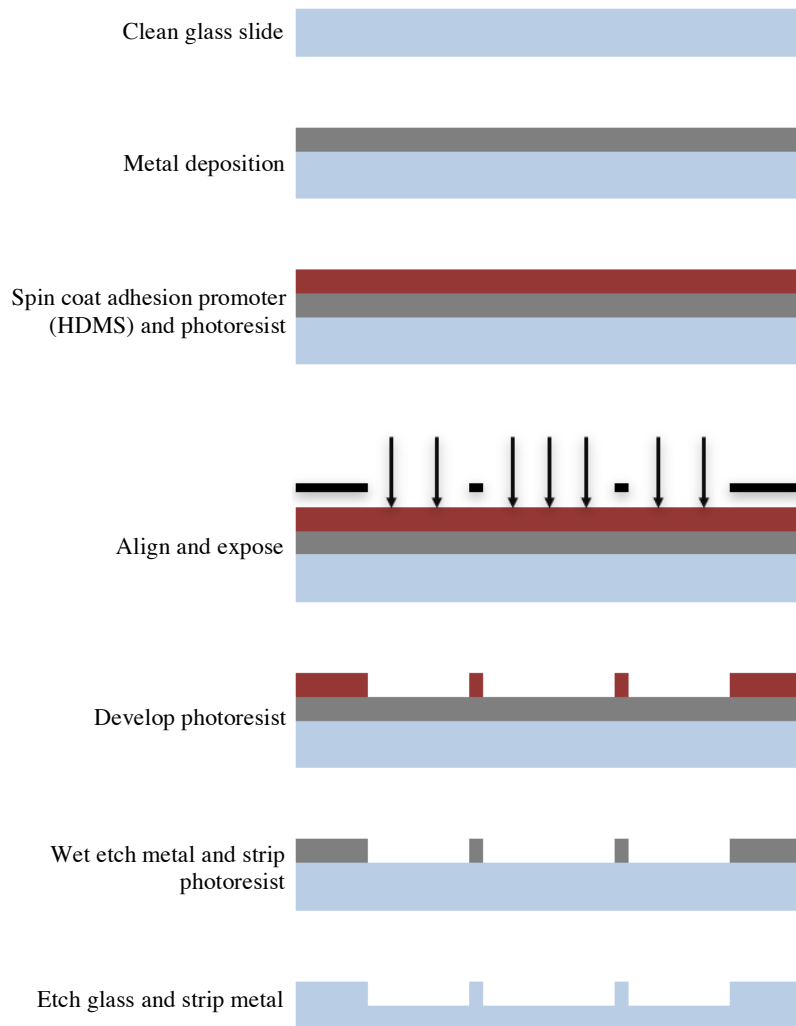


Figure B6. Lithography Process for Fabrication of the Flow Channel with Dam Structures.

References

1. Zeng, Z., Mendis, M. N., Waldeck, D. H., & Wei, J. (2016). A semi-analytical decomposition analysis of surface plasmon generation and the optimal nanoledge plasmonic device. *RSC Advances*, 6(21), 17196-17203.

APPENDIX C

SUPPORTING INFORMATION FOR CHAPTER VI

1. Methods

Semi-analytical Analysis: With a semi-analytical model,¹ the SPG efficiency, e , for the Au/glass interface at the bottom of the nanoslit aperture for one side of the aperture can be calculated using Eq. 1 from Chapter VI, in which

$$I_0 = \int_{-\infty}^{\infty} du \left[\sin(\pi w' u) / (\pi w' u) \right]^2 / v \quad (\text{Eq. C1})$$

$$I_1 = \int_{-\infty}^{\infty} du \frac{\exp(-i\pi w' u) \sin(\pi w' u) / (\pi w' u)}{v \left\{ v + \left[n_1^2 / (\varepsilon + n_1^2) \right]^{1/2} \right\}} \quad (\text{Eq. C2})$$

$$w' = n_1 w / \lambda, \quad (\text{Eq. C3})$$

where e is the SPG efficiency, α is the SPG coefficient, w is the width of the nanoslit structure, ε is the dielectric constant, n is the refractive index, I is the integration calculation, w' represents the scaled width, λ is the incident light wavelength, and u and v are applied for numerical integration with $u^2 + v^2 = 1$.

2. Results

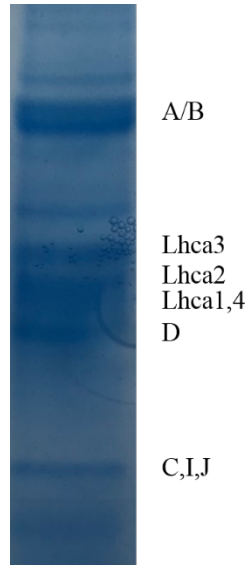


Figure C1. SDS-PAGE of PSI Complexes from Spinach. Extrude Extract and Label Methods were Prepared as Other Reports.^{2,3}

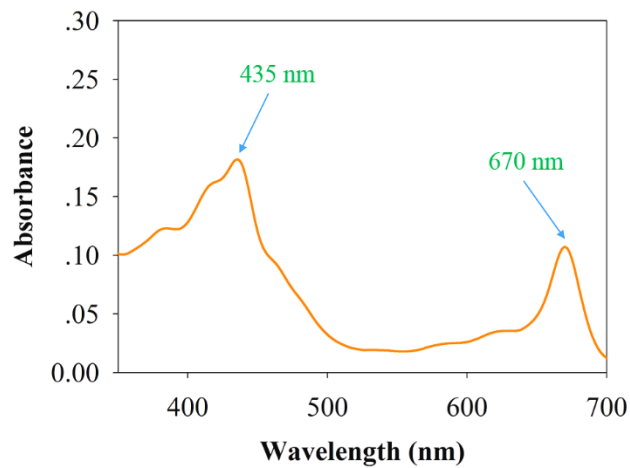


Figure C2. UV-Vis Absorption Spectrum of Purified PSI Complexes Performed in a Solution of 10 mM PBS.

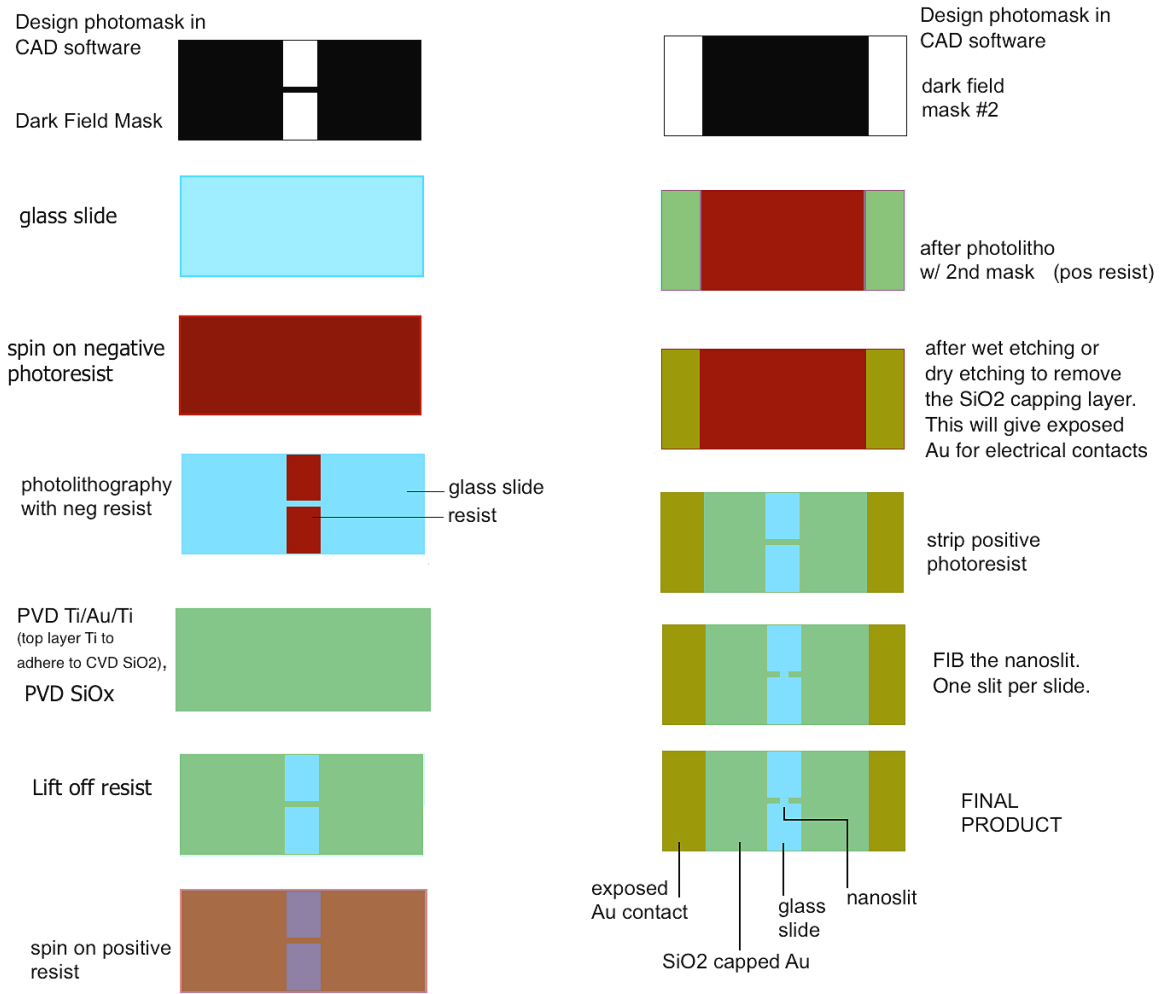


Figure C3. Illustration of the Protocol for Fabrication of the Electrochemical Device.

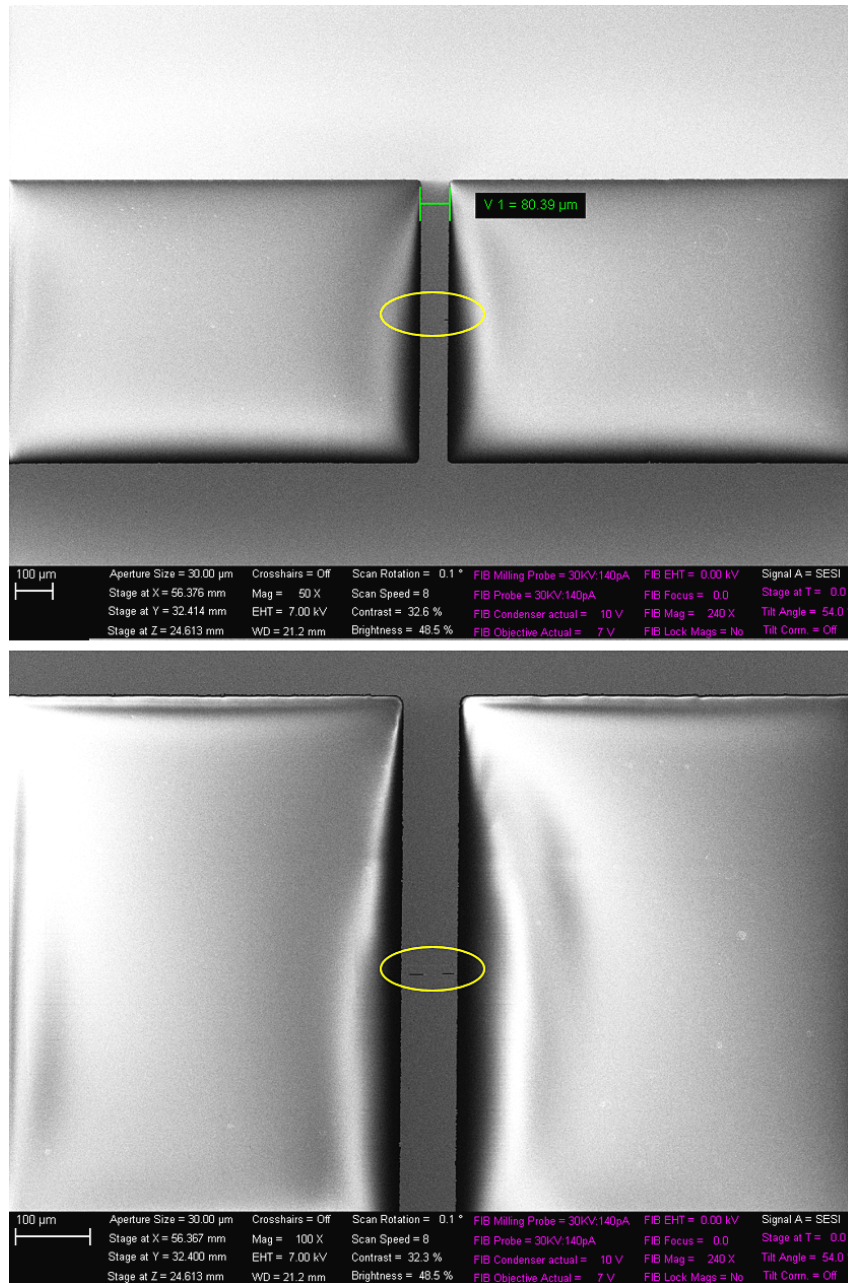


Figure C4. SEM Images of the Bridge Centers.

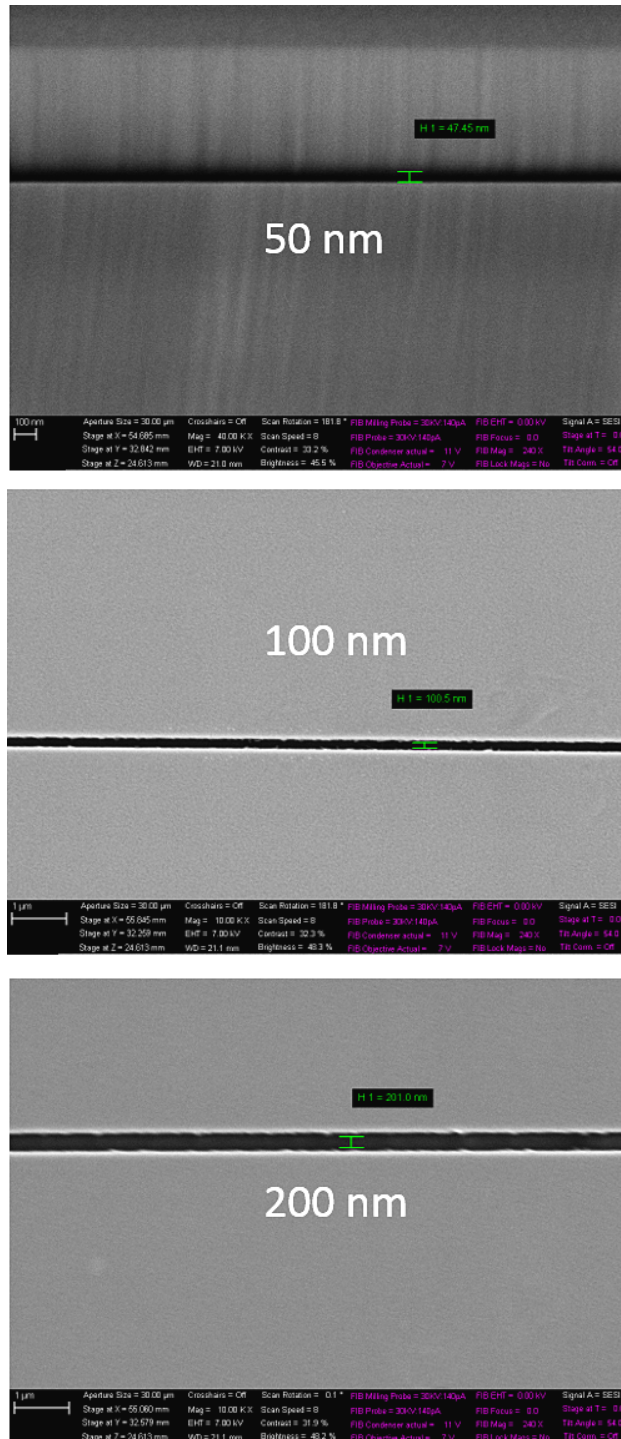


Figure C5. SEM Images of the Bridge Center Slit (Width of 50 nm, 100 nm, 200 nm, 300 nm, or 400 nm).

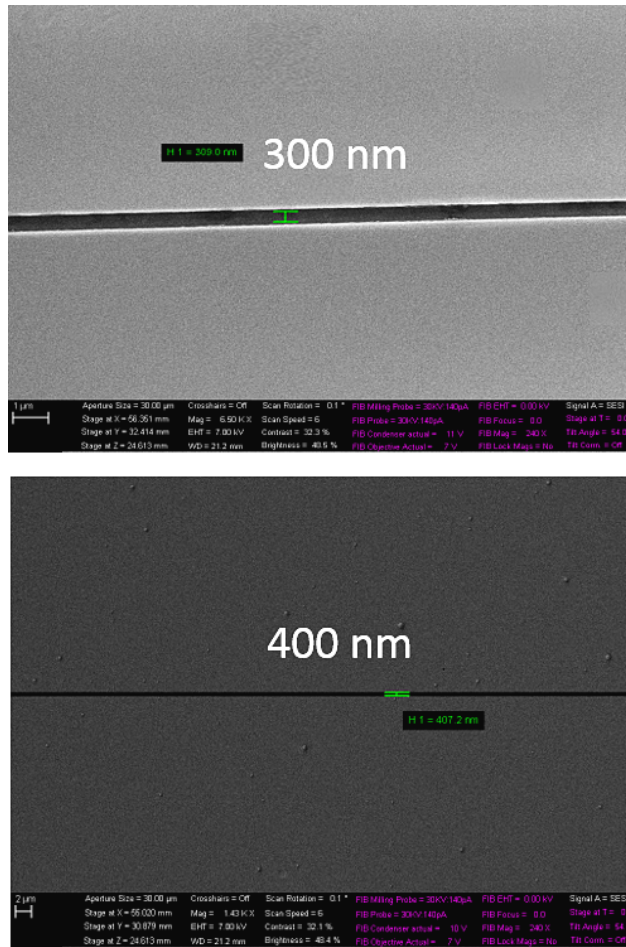


Figure C5. Cont.

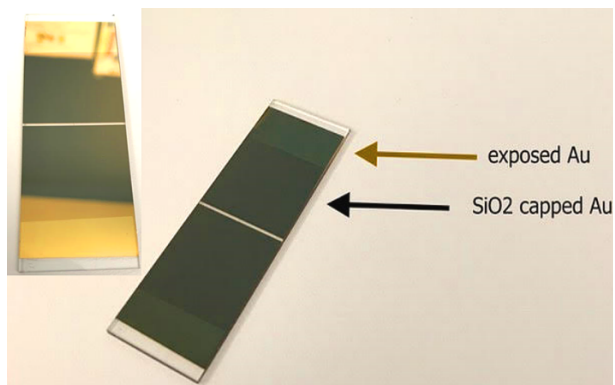


Figure C6. Electrochemical Device Images.

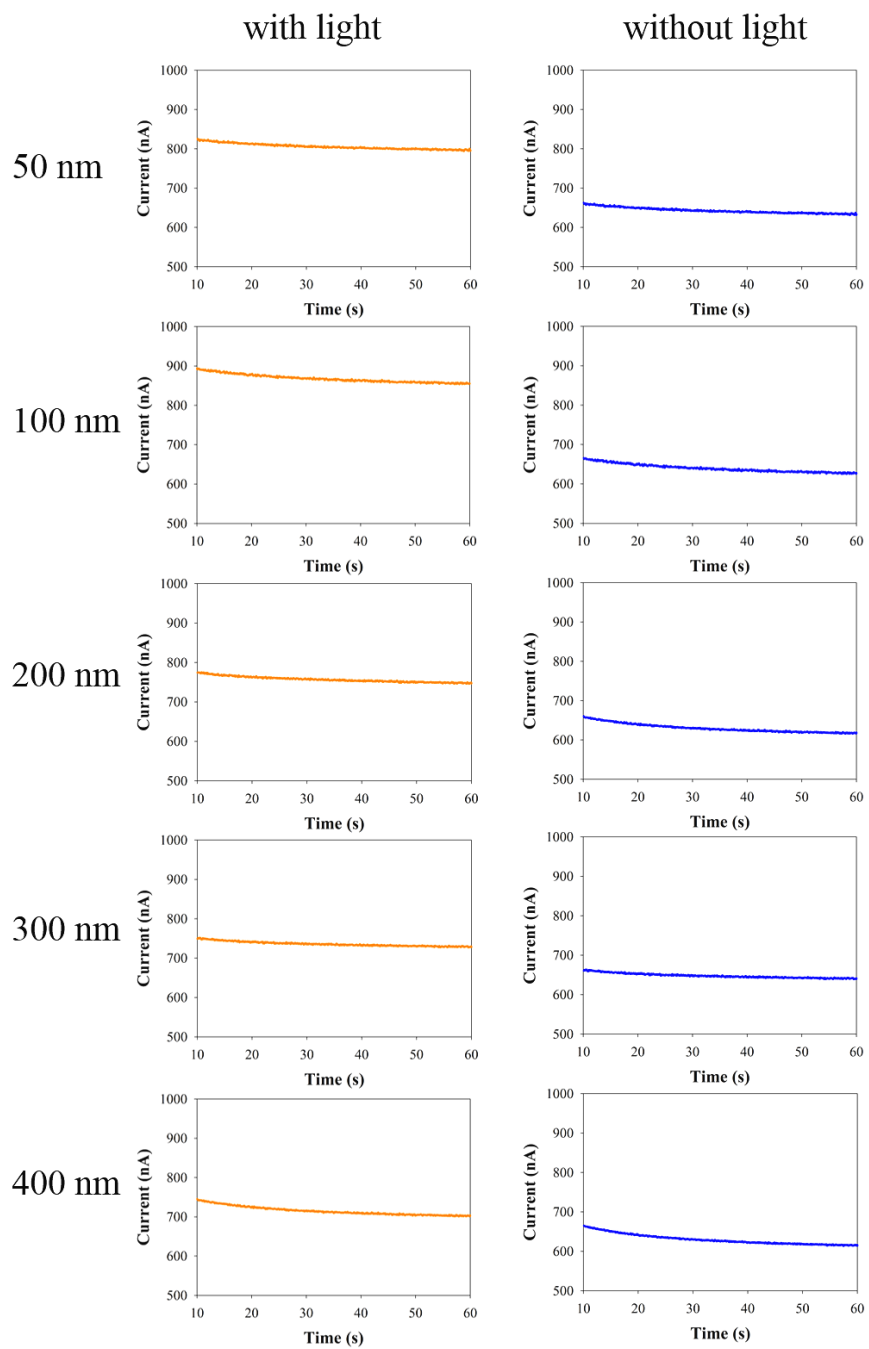


Figure C7. Representative Chronoamperometry (CA) Measurements of the Gold Slide Electrode with PSI Immobilization before and after Light Irradiation.

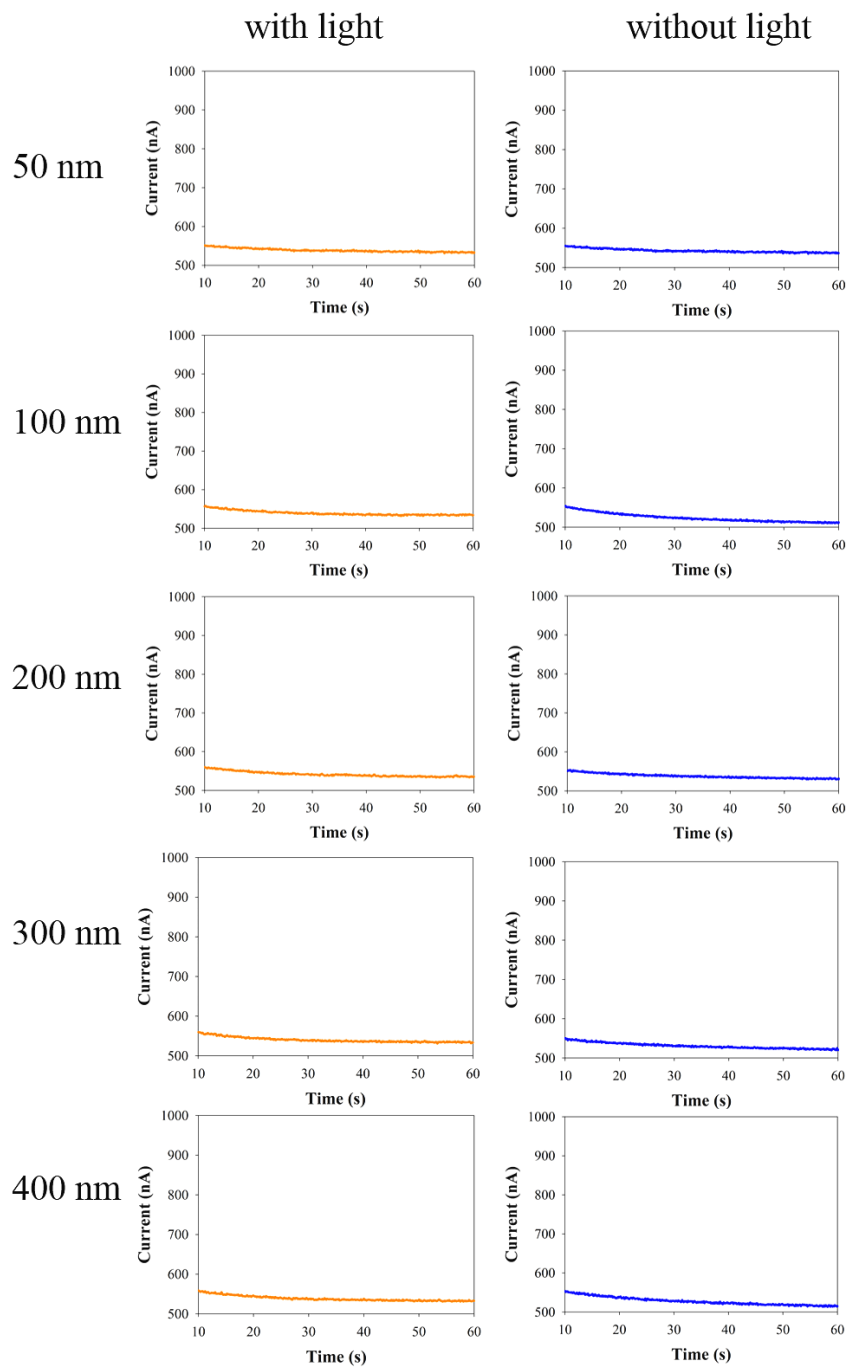


Figure C8. Representative Chronoamperometry (CA) Measurements of the Gold Slide Electrode without PSI Immobilization before and after Light Irradiation.

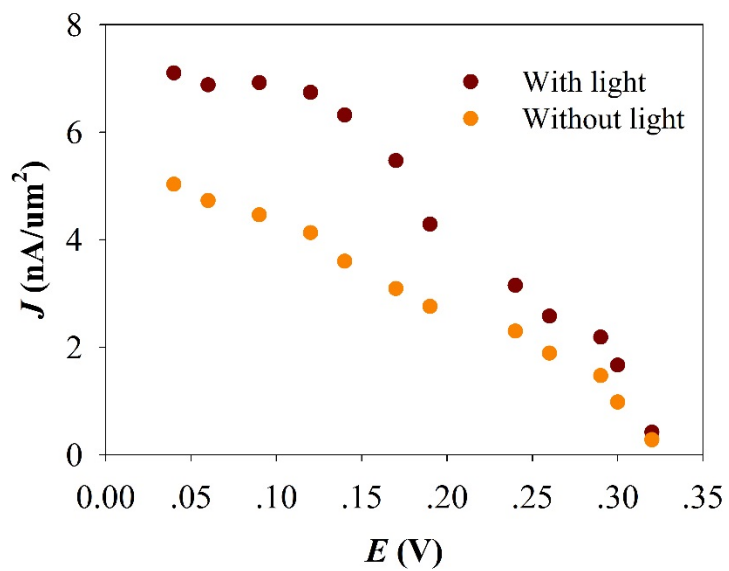


Figure C9. The Current-voltage Curve of the Gold Slide Electrode (100 nm Nanoslit) with PSI Immobilization in the Presence/Absence of Light Irradiation.

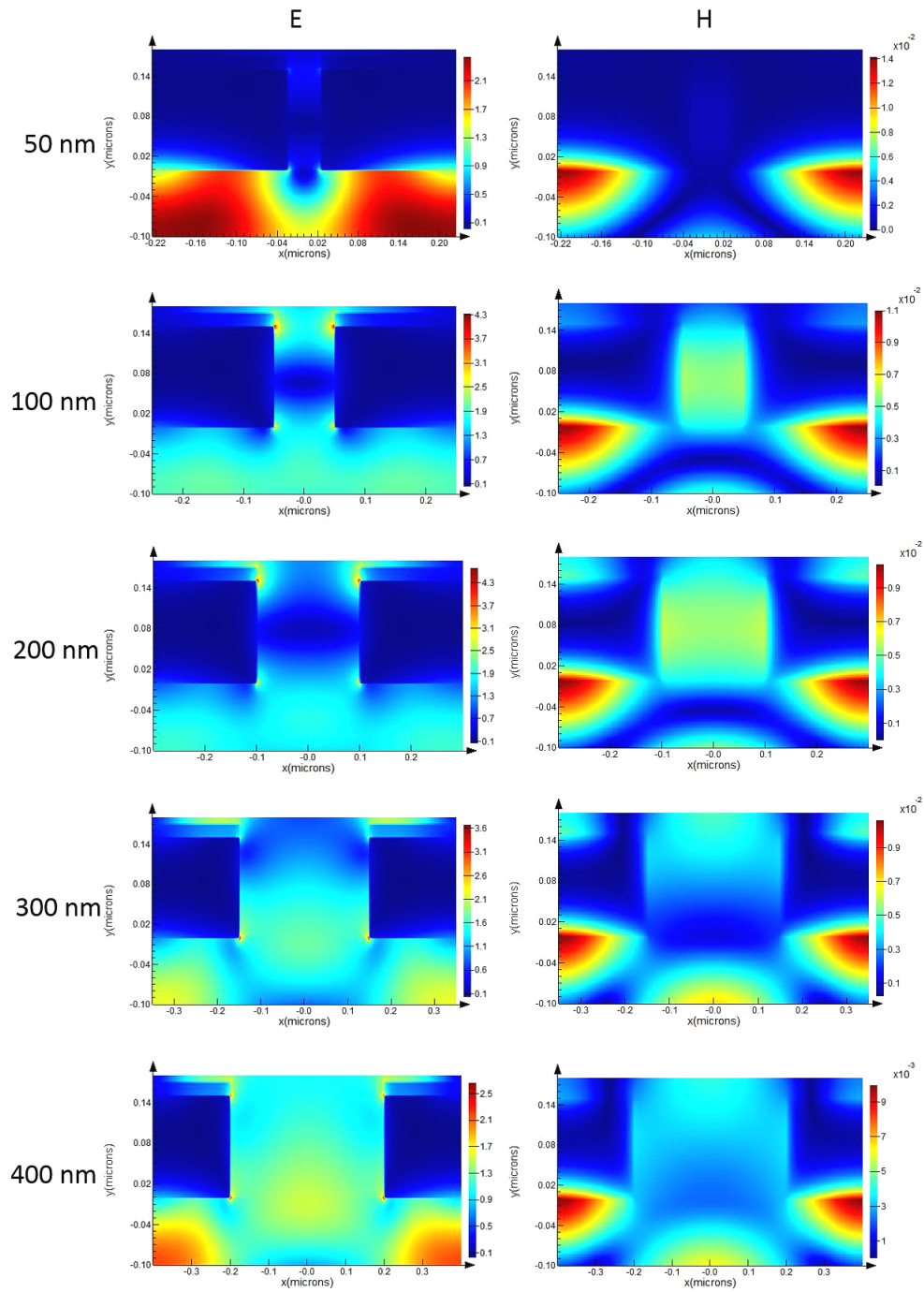


Figure C10. FDTD Simulation of Transverse Electro-magnetic Field Intensity for Different Nanoslit Structures without PSI Immobilization (E: Transverse Electric Field Intensities; H: Transverse Magnetic Field Intensity). The Units of Electric Field Intensity (E^2) and Magnetic Field Intensity (H^2) are $(V/m)^2$ and $(A/m)^2$, Respectively.

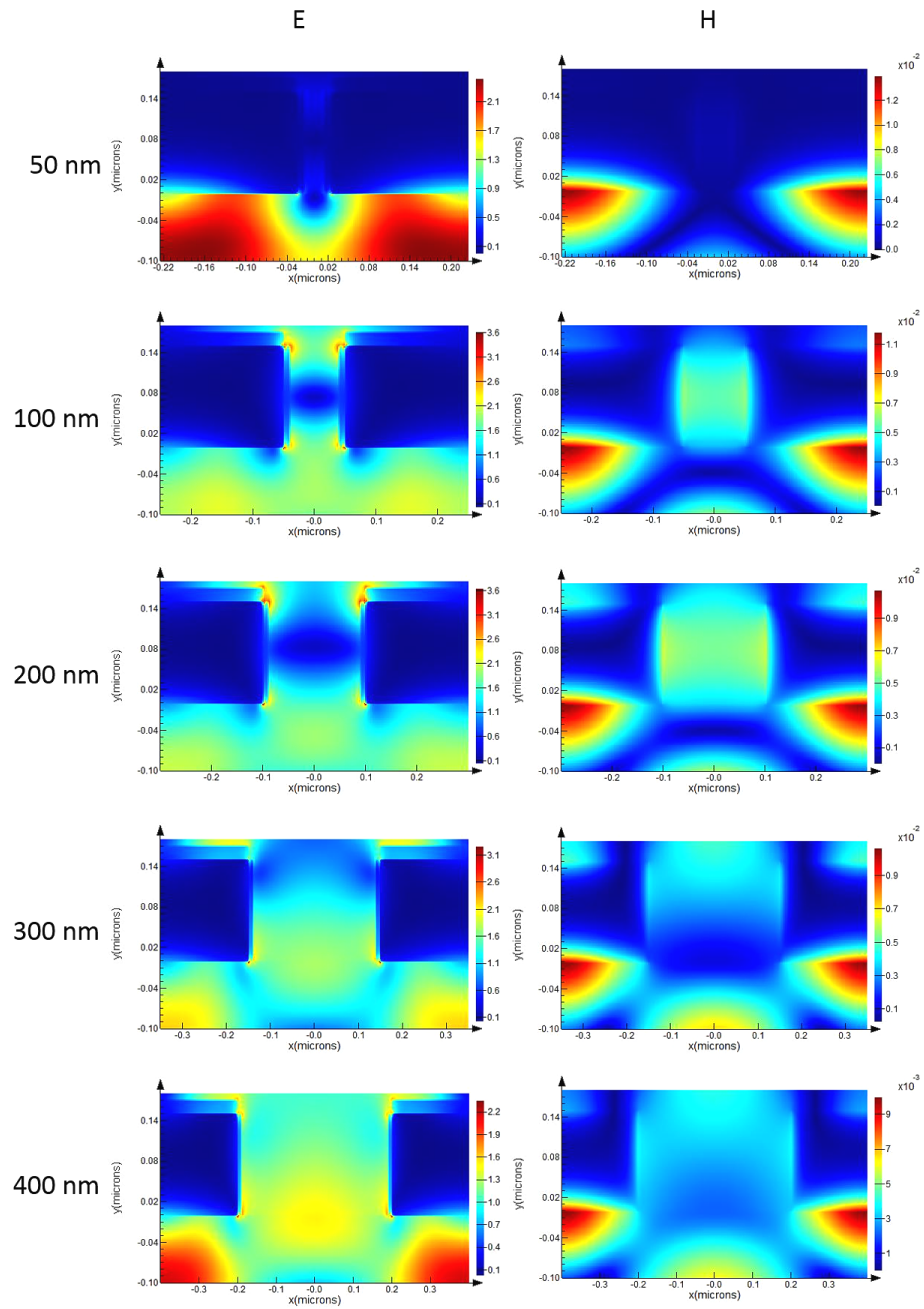


Figure C11. FDTD Simulation of Transverse Electro-magnetic Field Intensity for Different Nanoslit Structures with PSI Immobilization. The Thickness of PSI Film was Estimated to be 10 nm and Its Refractive Index was Estimated to be 1.5. (E: Transverse Electric Field Intensities; H: Transverse Magnetic Field Intensity). The Units of Electric Field Intensity (E^2) and Magnetic Field Intensity (H^2) are $(V/m)^2$ and $(A/m)^2$, Respectively.

Table C1

Photocurrent and Surface Plasmon Generation Efficiency Calculation for Different Nanoslits

Nanoslit Width (nm)	Photocurrent (nA)	SPG Efficiency
50	157±78	0.236±0.122
100	181±89	0.269±0.089
200	112±53	0.223±0.044
300	90±47	0.153±0.016
400	76±41	0.087±0.040

Table C2

I_0 and I_1 for Gold at Different Wavelengths When the Refractive Index n_1 is 1.41 (I_0 equals to Each Other for Different λ)

		600nm $\epsilon=$ -10.21+ 1.43i	700nm $\epsilon=$ -17.94+ 1.61i	800nm $\epsilon=$ -26.27+ 1.85i	900nm $\epsilon=$ -35.80+ 2.43i	1000nm $\epsilon=$ -46.05+ 3.11i	1100nm $\epsilon=$ -57.32+ 3.87i	1200nm $\epsilon=$ -68.98+ 4.68i
W'	I_0	I_1	I_1	I_1	I_1	I_1	I_1	I_1
0.1	3.09-4.09i	-0.02- 2.76j	0.23-2.85j	0.35-2.89j	0.44-2.91j	0.50-2.92j	0.55-2.93j	0.58-2.94j
0.2	2.94-2.61i	0.67-2.41j	0.94-2.45j	1.08-2.46j	1.18-2.47j	1.24-2.47j	1.29-2.46j	1.33-2.46j
0.3	2.72-1.69i	1.16-1.90j	1.42-1.87j	1.56-1.85j	1.66-1.83j	1.72-1.81j	1.77-1.79j	1.81-1.78j
0.4	2.43-1.05i	1.39-1.31j	1.63-1.22j	1.75-1.16j	1.84-1.12j	1.89-1.08j	1.93-1.05j	1.97-1.03j
0.5	2.13-0.64i	1.40-0.75j	1.58-0.61j	1.67-0.53j	1.73-0.47j	1.77-0.42j	1.80-0.38j	1.83-0.35j
0.6	1.82-0.34i	1.21-0.31j	1.33-0.14j	1.39-0.05j	1.42+ 0.02j	1.44+ 0.07j	1.46+ 0.11j	1.47+ 0.14j
0.7	1.54-0.18i	0.92-0.02j	0.98+ 0.13j	1.00+ 0.22j	1.00+ 0.29j	1.01+ 0.33j	1.01+ 0.37j	1.01+ 0.39j

Table C2

Cont.

		600nm	700nm	800nm	900nm	1000nm	1100nm	1200nm
		$\epsilon=$						
		-10.21+	-17.94+	-26.27+	-35.80+	-46.05+	-57.32+	-68.98+
		1.43i	1.61i	1.85i	2.43i	3.11i	3.87i	4.68i
W'	I ₀	I ₁						
0.8	1.30-0.10i	0.61+ 0.09j	0.62+ 0.22j	0.61+ 0.28j	0.60+ 0.33j	0.59+ 0.37j	0.58+ 0.39j	0.57+ 0.41j
0.9	1.11-0.06i	0.35+ 0.06j	0.33+ 0.14j	0.31+ 0.18j	0.29+ 0.21j	0.28+ 0.23j	0.26+ 0.24j	0.25+ 0.25j
1.0	0.97-0.07i	0.19-0.06j	0.16-0.02j	0.15-0.00j	0.13+ 0.01j	0.12+ 0.01j	0.11+ 0.01j	0.10+ 0.02j

Table C3

Surface Plasmon Generation Efficiency Calculation under Different Incident Wavelengths for Different Nanoslits

	50 nm	100 nm	200 nm	300 nm	400 nm
600 nm	0.46	0.42	0.29	0.12	0.02
700 nm	0.33	0.34	0.26	0.15	0.05
800 nm	0.24	0.29	0.24	0.16	0.08
900 nm	0.20	0.25	0.22	0.17	0.10
1000 nm	0.17	0.22	0.20	0.16	0.11
1100 nm	0.14	0.19	0.18	0.16	0.12
1200 nm	0.11	0.17	0.17	0.15	0.13

3. References

1. Zeng, Z.; Mendis, M. N.; Waldeck, D. H.; Wei, J. A Semi-analytical Decomposition Analysis of Surface Plasmon Generation and the Optimal Nanoledge Plasmonic Device. *RSC Adv.*, 2016, 6, 17196-17203.
2. Hiyama, T. Isolation of Photosystem I Particles from Spinach. In *Photosynthesis Research Protocols* (pp. 11-17). 2004, Humana Press.
3. Nelson, N.; Yocum, C. F. Structure and Function of Photosystems I and II. *Annu. Rev. Plant Biol.*, 2006, 57, 521-565.